



TECHNISCHE UNIVERSITÄT MÜNCHEN

Fakultät für Elektrotechnik und Informationstechnik

Lehrstuhl für Biologische Bildgebung

**Optoacoustic endoscopy: system development and application**

**Hailong He**

Vollständiger Abdruck der von der Fakultät für Elektrotechnik und Informationstechnik der Technischen Universität München zur Erlangung des akademischen Grades eines

**Doktor-Ingenieurs**

genehmigten Dissertation.

Vorsitzende(r): Prof. Dr. Majid Zamani

Prüfer der Dissertation:

1. Prof. Vasilis Ntziachristos, Ph.D.
2. Prof. Dr.-Ing. Christian Jirauschek
3. Prof. Dr. Dieter Saur

Die Dissertation wurde am 27.04.2017 bei der Technischen Universität München eingereicht und durch die Fakultät für Elektrotechnik und Informationstechnik am 24.10.2017 angenommen.



## Abstract

Endoscopic imaging techniques play a vital role for physicians to diagnose gastrointestinal diseases, such as white-light endoscopy (WLE), narrow-band imaging, optical coherence tomography and confocal laser endoscopy. Although these techniques can achieve cellular and subcellular resolution, their applications are limited to superficial structures due to strong photon scattering in soft tissue. While endoscopic ultrasound achieves much deeper penetration in tissue, it provides weak soft tissue contrast and low sensitivity, preventing its broad clinical use. In contrast, optoacoustic (also termed as photoacoustic) imaging is less sensitive to photon scattering and provides high resolution optical visualization in deep tissue compared to conventional optical imaging methods. Thus, optoacoustic technique in particular is well suited for endoscopy and disease detection can be enhanced via the application of multispectral optoacoustic tomography.

The work presented herein focused on developing optoacoustic endoscopy. Several implementations of optoacoustic endoscopy probes based on different scanning configurations, illumination settings and ultrasound transducers are implemented and analyzed regarding their influence on the endoscopic imaging performance. Afterwards, two dedicated endoscopy systems are developed for esophageal imaging, and imaging performance is characterized on phantoms and pig/human esophageal samples.

In addition to the technical development of the instrumentation, the necessary detection bandwidth for visualizing esophagus morphology is studied. For endoscopic or tomography image reconstruction, limited signals are usually recorded, resulting in artifacts and low image quality. Therefore, two image quality enhancement approaches are proposed to improve the reconstruction performance.

Finally, the clinical relevance of optoacoustic imaging on esophagus tissues is demonstrated by measuring excised esophageal samples from pigs and human with high resolution optoacoustic mesoscopy and the developed optoacoustic endoscopy systems. Afterwards, optoacoustic parameters such as the optimal laser wavelength and necessary detection bandwidth of the ultrasound transducer for esophagus imaging are investigated based on these measurements.

Overall, the imaging capabilities of optoacoustic and the developed endoscopy systems have been demonstrated to effectively resolve the structures of esophageal tissues, showing great clinical potential of esophagus imaging.

# Contents

Contents .....	v
Lists of abbreviations.....	ix
Chapter 1 Introduction.....	11
1.1 Clinical imaging modalities .....	11
1.1.1 X-ray CT .....	12
1.1.2 PET .....	13
1.1.3 MRI.....	13
1.1.4 Medical Ultrasound.....	14
1.2 Endoscopic imaging today .....	15
1.2.1 White light endoscopy .....	15
1.2.2 Optical endoscopy.....	16
1.2.3 Ultrasound endoscopy.....	17
1.3 Objectives addressed in this thesis .....	18
1.4 Outline of this dissertation .....	20
Chapter 2 Theoretical and technical background .....	22
2.1 General knowledge of optoacoustic imaging.....	22
2.1.1 Optoacoustic signal generation and properties .....	22
2.1.2 Penetration depth .....	27
2.1.3 Acoustic reflection and attenuation .....	28
2.2 Optoacoustic image formation .....	30
2.2.1 Backprojection algorithm.....	30
2.2.2 Model-based algorithm .....	31
2.3 Technical aspects of optoacoustic endoscopy implementation.....	32
2.3.1 Existing configurations .....	32
2.3.2 Ultrasound transducers.....	35
2.3.3 Image display approaches .....	38
2.4 Summary and discussion.....	39
Chapter 3 Implementations of optoacoustic endoscopy probes .....	40
3.1 Curved endoscopy probe .....	40
3.1.1 Endoscopy probe implementation.....	41
3.1.2 Characterization measurements .....	42

3.2	Hybrid OR and AR optoacoustic endoscopy probe .....	46
3.2.1	Hybrid endoscopy probe .....	47
3.2.2	Characterization measurements .....	49
3.3	Linear array-based endoscopy probe.....	52
3.3.1	Transducer array based endoscopy probe .....	53
3.3.2	Characterization measurements .....	55
3.4	Summary and Discussion .....	58
Chapter 4	Optoacoustic endoscopy system development.....	60
4.1	The scanning control system .....	60
4.2	IVUS-based endoscopy system.....	62
4.2.1	System implementation.....	62
4.2.2	System characterization .....	64
4.3	Focused detector based endoscopy system .....	65
4.3.1	System implementation.....	66
4.3.2	System characterization .....	67
4.4	Summary and discussion.....	69
Chapter 5	Importance of ultrawide bandwidth for endoscopy performance .....	71
5.1	Introduction .....	71
5.2	Simulations and experimental measurement.....	72
5.2.1	Simulations .....	72
5.2.2	Imaging setup.....	73
5.2.3	Phantom and tissue measurements.....	75
5.3	Results .....	76
5.3.1	Simulation results.....	76
5.3.2	Experimental results.....	77
5.4	Summary and Conclusion .....	81
Chapter 6	Image quality enhancement methods.....	84
6.1	Accelerated sparse recovery method.....	84
6.1.1	Methods and materials .....	85
6.1.2	Results.....	91
6.2	Geometric pixel super-resolution approach .....	99
6.2.1	Methods and materials .....	101
6.2.2	Results.....	107
Chapter 7	Optoacoustic imaging of esophageal tissue .....	117
7.1	Clinical interests of esophagus imaging.....	117
7.2	Esophagus sample measurements by Mesoscopy .....	119
7.2.1	Mesoscopy imaging system .....	119

7.2.2	Pig esophagus measurement .....	120
7.2.3	Human esophagus measurement.....	121
7.2.4	Multi-spectra optoacoustic imaging of esophagus sample .....	123
7.2.5	Frequency characteristics .....	126
7.3	Optoacoustic endoscopy imaging of esophageal sample .....	127
7.3.1	Esophagus measurement by IVUS-based endoscopy system .....	127
7.3.2	Challenges of in vivo measurements .....	128
7.3.3	Esophagus measurement by focused detector based endoscopy system .....	130
7.3.4	Further development .....	132
7.4	Summary and discussion .....	134
Chapter 8	Conclusion and outlook .....	135
8.1	Conclusion .....	135
8.2	Outlook .....	137
	Acknowledgements.....	140
	Publication lists.....	142
	Bibliography .....	144



## **Lists of abbreviations**

WLE	White-light endoscopy
IVUS	Intravascular ultrasound
CT	Computed tomography
PET	Positron Emission Tomography
MRI	Magnetic Resonance Imaging
CLE	Confocal laser microendoscopy
FDG	Fluorodeoxyglucose
fMRI	functional MRI
BOLD	Blood oxygenation level dependent
HD-WLE	High-definition WLE
OCT	Optical coherence tomography
EUS	Endoscopy ultrasound
MSOT	Multi-spectra optoacoustic tomography
SO <sub>2</sub>	Oxygen saturation of hemoglobin
AR-OE	Acoustic resolution optoacoustic endoscope
OR-OE	Optical-resolution optoacoustic endoscopy
ICG	Indocyanine green
NIR	Near infrared
GPU	Graphics processing units
AJCC	American Joint Committee on Cancer
EP	Epithelium
LP	Lamina propria
MM	Muscularis mucosa

SM	Submucosa
MP	Muscularis propria
EMR	Endoscopic mucosal resection
MIP	Maximum-intensity projections
CNR	Contrast to noise ratio
FWHM	Full width at half-maximum
OPO	Optical parametric oscillator
EC	Esophageal cancer
LSQR	Sparse Equations and Least Square
ASALSA	Split Augmented Lagrangian Shrinkage Algorithm
CF	Coherence factor
MAP	Maximum a posteriori
ADMM	Alternated direction method of multiplier
PSR	Pixel super resolution
PSF	Point spread function
LR	Low resolution
HR	High resolution
BTV	Bilateral total variation
FBP	Filtered back-projection
SoS	Speed of sound

# Chapter 1 Introduction

“The ability to establish an immediate endoscopic diagnosis that is virtually consistent with the histologic diagnosis has been the ultimate objective of endoscopists since the very earliest phases of the development of endoscopy” [1]. In order to achieve this goal, imaging techniques are generally applied to enable visualization of tissue structures under surface. Modern clinical imaging techniques allow visualization of the representations of the interior of a body revealing internal structures concealed by the skin and bones. They play a key role in clinical diagnostic procedures and medical intervention. Endoscopy provides an alternative solution for medical doctors to examine the interior of a hollow organ or cavity inside the body [2]. Many imaging modalities have been implemented into endoscopic modes, which can be inserted directly into luminal organs and acquire high quality images. For example, optical imaging approaches relying on the electromagnetic field at visible wavelengths have been widely used for endoscopy applications, such as white-light endoscopy and confocal laser microendoscopy (CLE) [3, 4]. However, these techniques are limited to superficial structures due to photon scattering in soft tissue. Ultrasound endoscopy can achieve deep penetration depth in soft tissue, while low soft tissue contrast limits its clinical use for gastrointestinal diseases. Optoacoustic imaging, as a novel modality, is less sensitive to photon scattering within biological tissues. It provides high resolution optical visualization in deep tissue compared to conventional optical imaging methods, which is well suited for endoscopy applications [5-9]. Therefore, the goal of this work is to develop optoacoustic endoscopy system.

## 1.1 Clinical imaging modalities

The most commonly used imaging modalities in clinics include: X-ray Computed Tomography (X-ray CT), Positron Emission Tomography (PET), Magnetic Resonance Imaging (MRI) and medical ultrasound. These techniques can achieve whole body imaging and provide anatomical and function information, which have been applied for the diagnosis

of gastrointestinal disease, such as identifying advanced esophageal or colon cancer [10-13]. However, limited resolution or contrast restricts their capability of resolving the earlier gastrointestinal diseases [14, 15]. Indeed, several reports showed the limited ability of evaluating earlier esophageal cancer because of incapability to discriminate the esophageal wall layer and detect the infiltration depth of the tumor [10, 14, 16].

### **1.1.1 X-ray CT**

X-ray CT scan is a computer-processed combination of many X-ray images taken from different scanning positions to produce cross-sectional images of an object, allowing noninvasively visualizing inside the object [17, 18]. Since its introduction in the 1970s, X-ray CT has been an important medical imaging tool to supplement X-rays and ultrasonography, which can acquire detailed images of internal organs, bones, soft tissue and blood vessels [17, 18]. Pixels of X-ray CT images represent relative radiodensity of tissue. Intrinsic differences in absorption between bone, fat, air and water result in high-contrast images of anatomical structures. Comparing to traditional two-dimensional medical radiography, X-ray CT has several advantages. First, X-ray CT completely eliminates artifacts produced outside the area of interest. Secondly, because of its high sensitivity, X-ray CT scan can differentiate tissues that differ in physical density by less than 1%. Finally, the cross-sectional images generated during a X-ray CT scan can be reformatted into multiple planes, and three-dimensional images can be generated and viewed on a computer monitor, printed out or transferred to electronic media. Recent advances in X-ray CT technology, including multi-detector rows X-ray CT and new real time volumetric imaging systems, have enhanced the applications of CT scan to evaluate the intestinal organ. For example, X-ray CT colonography and the generation of volumetric images of colon can be used for cancer detection [19]. Volume rendering of X-ray CT data coupled with interactive volumetric and stereoscopic display is very helpful to more clearly depict gastric disease. However, due to its ionizing nature, great attention is taken to minimize the use of X-ray CT scan for a given time interval. There is always a slight chance of cancer from excessive exposure to radiation. However, the benefit of an accurate diagnosis far outweighs the risk.

### 1.1.2 PET

Another modality based on ionizing radiation is known as positron emission tomography. This technique detects pairs of gamma rays emitted indirectly by a positron-emitting radionuclide (tracer), which is introduced into the body on a biologically active molecule [13]. Early PET scanners had only a single ring of detectors; hence the acquisition of data and subsequent reconstruction was restricted to a single transverse plane. More advanced scanners now include multiple rings, essentially forming a cylinder of detectors. By rotating the detection camera around the patient, cross-sectional images and 3D volumes can be reconstructed directly according to the detection geometry. PET offers quantitative analyses and can monitor relative changes of the tracer over time as a disease evolves or in response to a specific stimulus. For example, PET scanning with the tracer fluorine-18 (F-18) fluorodeoxyglucose (FDG), called FDG-PET, is widely used in clinical oncology [13]. Use of this tracer to explore the possibility of cancer metastasis is the most common type of PET scan in standard medical care. However, the widespread clinical use of PET has been restricted because of the high costs of cyclotrons needed to produce the short-lived radionuclides for PET scanning. Also, there are very limited choices of the tracer used for PET scan. Besides, safety and high costs are needed to be concerned for PET test. Typically, PET scans are combined with CT or MRI scans, giving both anatomic and metabolic information, which enhances the PET scan to provide higher sensitivity and specificity and expands its application fields [11, 13].

### 1.1.3 MRI

Magnetic resonance imaging is used in radiology to produce images of the anatomy and the physiological processes of the body based on stimulating water molecules [20]. In contrast to X-ray or PET, MRI does not rely on ionizing radiation but rather on strong magnetic fields, which has been proven to have no harm on patients. The main principle of MRI is to use strong magnetic fields to generate detectable radio frequency signal from hydrogen atoms, which exists naturally in tissue, particularly in water and fat. For this reason, MRI scans usually map the location of water and fat in the body. Pulses of radio waves excite the nuclear spin energy transition, and magnetic field gradients localize the signal in space. By changing

the parameters of the pulse excitation and recording, different contrasts can be generated between tissues based on the relaxation properties of the hydrogen atoms known as T1 and T2 weighting. MRI is considered as the best imaging modality for soft tissue pathology. It is also widely used in assessing prostate cancer, staging of esophagus tumor, hepatocellular cancer and liver metastases, renal cell carcinoma, pancreatic adenocarcinoma and other malignancies [13, 20]. Besides its excellent ability of providing anatomical information, functional MRI (fMRI), diffusion MRI or MR angiography, have extended applications to obtain functional and molecular information. For example, fMRI is widely used for brain imaging, which can help to understand how different parts of the brain respond to external stimuli or resting state activity [13, 20]. Change of the ration of oxyhemoglobin and deoxyhemoglobin can be measured by blood oxygenation level dependent (BOLD) fMRI [21]. However, limitations of this modality include applicability, procedural cost and availability. Generally, patients carrying ferromagnetic implants are not allowed for MRI scanning. Frequently, patients are not always prescribed a MRI test because of the high costs covering a long process that can take several hours and involve several medical personnel [20].

#### **1.1.4 Medical Ultrasound**

Medical ultrasound is a diagnostic imaging technique based on the application of ultrasonography [22]. Ultrasonic images also known as sonograms are produced based on sending pulses of ultrasound into tissue using a transducer probe and recording the reflected waves. The recorded waves can be reconstructed as images, which reflect the acoustic impedances of tissue. Typical medial ultrasound systems are operated in the frequency range of 1 to 18 megahertz, although high frequencies (50–100 MHz) have been used experimentally in a technique known as US bio-microscopy [23, 24]. The choice of frequency significantly determines the spatial resolution and imaging depth: lower frequencies create less resolution but image deeper up to tens of centimeters. Higher frequency ultrasound signals can lead to high resolution in the range of micrometers. However, higher frequency waves have a larger attenuation coefficient, limiting the depth of penetration. B-mode ultrasound images are usually acquired by using transducer array, which can display the acoustic impedance of a cross-section of tissue in real time. Other

information, like blood flow, motion of tissue over time, the location of blood, the presence of specific molecules, the stiffness of tissue, or the anatomy of a three-dimensional region can be acquired by advanced ultrasound techniques, such as Doppler ultrasound and 3D ultrasound [24-27]. Compared to aforementioned medical imaging modalities, ultrasound has several advantages. For example, it provides real-time 2D images. Besides, current ultrasound systems are portable and can be brought to the bedside. Low cost and no harm make it very commonly used in clinics. Drawbacks of medical ultrasound include low tissue contrast, difficulties in imaging structures behind bone and air, and its dependence on a skilled operator [25].

## 1.2 Endoscopic imaging today

### 1.2.1 White light endoscopy

The first endoscope was developed in 1806 by Philipp Bozzini in Mainz with his introduction of a "Lichtleiter" (light conductor) "for the examinations of the canals and cavities of the human body. Modern clinical endoscopy procedure was initially conducted by white-light endoscopy with magnification and/or augmented by chromo-endoscopy, which yielded reasonable accuracy rates for the prediction of histology [28]. Gradually high-definition WLE (HD-WLE) replaced the standard-definition WLE because of its high resolution and better capabilities for tissue characterization [28]. Despite its wide clinical acceptance, WLE is limited by accessing only superficial tissue features and generally low contrast between early disease and surrounding tissue, leading to reduced sensitivity and specificity in detecting flat adenomas and identifying disease infiltration [29]. Moreover, human vision is insensitive to detecting early disease as it lacks disease specificity. Typically, gastrointestinal diseases generally grow and develop below the tissue surface [2]. Since video endoscopy can only provide information of the superficial mucosal structures, features underneath the tissue surface cannot be seen with conventional endoscopy or even higher-resolution forms of endoscopy such as high-definition magnification endoscopy. In these instances, random biopsy is usually used to get more information [14, 30]. Normally a flexible video endoscopy probe is inserted into the luminal digestive organs. If an abnormal region is identified,

endoscopic biopsy forceps are used to extract a small amount of tissue from the irregular areas. Typically, biopsies are taken from several fields with the hope of sampling the correct spot, which, unfortunately, often has high missing rate [14, 30]. Pathologist then processes and reviews the biopsied samples under a microscope to define the diagnosis and intervention strategies [28].

### **1.2.2 Optical endoscopy**

As random biopsy is an invasive method and has high missing rate for gastrointestinal tests, optical imaging techniques have been considered to complement WLE, such as confocal laser endomicroscopy [31, 32], fluorescence endoscopy [2], and optical coherence tomography [33, 34].

Confocal laser endomicroscopy is a newly introduced endoscopic tool that makes it possible to carry out confocal microscopic examination of superficial layer during ongoing endoscopy [31]. The method of CLE has recently been developed, which allows high resolution in vivo histological assessment, so that changes in vessels, connective tissue, and cellular or subcellular structures can be evaluated during ongoing endoscopy examinations. It has been shown that living cells and cellular structures of the mucosal layer in human esophagus were observed [31, 35]. Different types of tissue and diseases can be diagnosed immediately, facilitating early diagnosis of gastrointestinal cancer [31, 35]. Analysis of in vivo microarchitecture relying on the CLE approach is helpful in targeting biopsies to relevant areas [31]. However, due to intrinsic limitations of photon propagation in tissues, CLE has limited imaging penetration depth and only interrogates small superficial lumen volumes ( $<0.1 \text{ mm}^3$ ) at a time, which prevents application to surveillance endoscopy [31, 35].

The use of fluorescence imaging has a promising outlook for endoscopic surveillance, especially when utilizing systemic or local administration of agents with disease specificity [36-38]. Video autofluorescence endoscopy is an imaging technique, which utilizes the autofluorescent properties of endogenous fluorophores in the gastrointestinal tract, such as collagen and elastin [2]. Light at specific wavelength is required to excite these fluorophores, emitting light of a longer wavelength. Based on the autofluorescence properties, this technique can identify areas of dysplasia as magenta on a background of green mucosal reflection [37].

This information is helpful for diagnose Barret esophagus [2]. Although autofluorescence endoscopy is a new technology for wide-field imaging, the high false-positive rates of current generation autofluorescence endoscopes have limited its clinical use [36-38]. In order to enhance the specificity of fluorescence endoscopy, exogenous fluorophores accumulate selectively in malignant lesions and induce fluorescence after illumination with light of adequate wavelength [36-38]. However, fluorescence imaging is two-dimensional in nature and the administration of sensors comes with a higher threshold of clinical regulatory processes compared to label-free lumen inspection.

Optical coherence tomography provides non-invasive and label-free imaging of living tissue and organism [34, 39]. OCT images generated based on the principles of optical interferometry, which gives several distinctive capabilities comparing to other imaging modalities for endoscopy applications [40]. For example, OCT imaging uses longer wavelengths in the near-infrared region, which allows OCT to image at high resolution and deeper into soft tissue than possible using shorter wavelength optical microscopy [40]. Besides, OCT has proved real time imaging capability of human gastrointestinal tract [41]. These factors have combined to result in the adoption of OCT for several diagnostic applications, such as ophthalmic OCT and intravascular OCT [40, 42]. However, like other optical imaging modalities, OCT imaging is still limited to superficial structures, impairing its clinical applications [34, 39].

### 1.2.3 Ultrasound endoscopy

Endoscopy ultrasound (EUS) is a widely used clinical imaging modality for esophagus cancer staging, which can provide high-speed, high-resolution, cross-sectional imaging over a large field of view [24, 26, 27, 43]. The poor tissue contrast, however, limits ultrasound endoscopy for early-stage tumor detection or *in situ* characterization of diseased tissues [44]. The boundaries in EUS images are set by the reflections of the interfaces between various layers, and there is little difference between the actual anatomical structure and the echoic gray scale of EUS. Furthermore, tumor boundaries and connections with surrounding blood or lymphatic vessels are clinically relevant and provide necessary information for assessing disease stage or progress and planning treatment strategies [45]. However, pure ultrasound-

based image contrast does not sufficiently provide this crucial information, since low tissue contrast of ultrasound restricts the ability of resolving the esophagus structures [43, 46]. Therefore, EUS requires further improvements or cooperating with other imaging modalities, to enhance the accuracy of early esophagus cancer staging.

### **1.3 Objectives addressed in this thesis**

Optoacoustic imaging combines the advantages of both modalities, i.e. the rich contrast of optical imaging and the high resolution of ultrasonic imaging [7, 9]. This technique is less sensitive to photo scattering within biological tissue, and provides high resolution optical visualization across a wider ranges of depths, from a few hundred micrometers to several centimeters, exceeding the penetration depths of conventional high-resolution optical imaging modalities [7, 9]. In recent multi-spectra optoacoustic tomography (MSOT) modality, optoacoustic has been widely applied to resolve the bio-distribution of targeted optical agents, fluorescent proteins, circulating gold-nanorods, vascular structures and tumor hypoxia [6-8, 47, 48]. Because of these advantageous features, optoacoustic endoscopy has recently emerged as a new research area for applications in preclinical and clinical development, like the intravascular, gastrointestinal and urogenital systems [49, 50]. With high optical contrast, tumor boundaries and surrounding lymphovascular systems can be resolved with endogenous or exogenous contrast agents [6, 8, 48]. Additionally, physiological or functional information, including total hemoglobin concentration, oxygen saturation of hemoglobin (SO<sub>2</sub>) can be gained for accurate staging of gastrointestinal cancer [51].

However, current optoacoustic endoscopy are mostly designed and validated on small animals, which have been shown to resolve the superficial vascular structure of the esophageal lumen of rats and rabbits [52-55]. However, imaging of human esophageal lumen has not yet been investigated. The layer thickness of the mucosa and submucosa in the human esophageal wall varies from a few hundred  $\mu\text{m}$  to millimeters, which is markedly greater than the thickness of rat and rabbit esophageal wall, possibly requiring different operational characteristics in terms of ultrasound transducers. Besides, the imaging capability and working distance of the existing endoscopic probes are designed to scan small luminal organs, such as colon and esophagus of rats or rabbits [52-55]. However, gastrointestinal

tracts of human usually have much larger diameters and more complicated structures, which require adapted implementations of endoscopy probes. Furthermore, miniaturized transducers with low sensitivity and complicated implementations are commonly used in current optoacoustic endoscopy probes, resulting in limited image quality and penetration depth. Therefore, advanced implementations of optoacoustic endoscopy should be developed for esophagus imaging of human or large animals.

This work focuses on the development of optoacoustic endoscopy system and rigorous evaluation of optoacoustic imaging on excised esophageal samples from human and pigs. It also presents improved frameworks for better image reconstruction and image quality enhancement. The framework of this thesis is divided in three main objectives:

(1) Development of optoacoustic endoscopy probe

First, several optoacoustic endoscopic probes are built based on different scanning geometries, illumination settings, and ultrasound transducers to explore possible implementations of optoacoustic endoscopy probes. The influence of these factors on the endoscopy imaging performance is analyzed, which is helpful to optimize the endoscopy system development. Then two optoacoustic endoscopy systems are developed for esophagus imaging. One is based on an intravascular ultrasound detector with the support of commercial working channel and the other is a miniaturized capsule version based on a spherical focused transducer. Furthermore, the necessary detection bandwidth of ultrasound transducers for resolving esophagus layer structures is studied, which suggests how to optimize the selection of ultrasound transducers for esophagus imaging.

(2) Improvement of image reconstruction

The reconstruction method for radial scanning mode is studied. Besides, two image quality enhancement approaches are introduced to enhance the reconstruction performance of optoacoustic tomography. One method is implemented to accelerate the model-based reconstruction process with novel coherence factor weighting scheme for suppressing noise and artifacts. Another one is a geometrical super resolution approach, which integrates

information from multiple optoacoustic images acquired at sub-diffraction steps into one high resolution image by means of an iterative registration algorithm.

### (3) Study of optoacoustic imaging on esophagus tissues

The capability of optoacoustic on resolving the structures of the esophagus wall is demonstrated by measuring esophagus samples from human and pigs with optoacoustic mesoscopy and the developed optoacoustic endoscopy systems. Optoacoustic parameters for esophagus imaging, such as wavelength, contrast and detection bandwidth, are studied and analyzed based on the measurements.

## **1.4 Outline of this dissertation**

This work is organized as follows:

Chapter 2 firstly introduces the theoretical and technical background of optoacoustic imaging, which reviews the main principles of optoacoustic imaging, including the signal generation and sound propagation in tissue. Afterwards, representative reconstruction approaches for optoacoustic imaging are introduced, including the backprojection and mode-based methods. At end of this chapter, the existing implementations of optoacoustic endoscopy and corresponding image display methods are discussed.

Chapter 3 introduces several implementations of optoacoustic endoscopy probes based on different scanning geometries, illumination configurations and ultrasound transducers. For example, a curved endoscopy probe is implemented based on the IVUS detector, which could achieve better image quality than the linear scanning configuration. Besides, a hybrid optical resolution and acoustic resolution optoacoustic endoscopy with a single sensor is proposed. Apart from single element based endoscopy probe, the merits and imaging performance achieved with a miniaturized linear transducer is investigated, which could allow the endoscopic deployment of MSOT.

Chapter 4 describes two endoscopy systems designed for esophagus imaging. An IVUS based endoscopy probe is first introduced. With a diameter less than 3.6 mm, it can be cooperated with working channel of conventional optical endoscope. In order to enhance the image

quality, a spherical focused detector is used for endoscopy implementation, enhancing the image quality with the ultrasound focusing capability.

Chapter 5 analyzes the importance of ultrawide detection bandwidth of ultrasound transducers for esophagus imaging. Utilizing two detectors with 15 and 50 MHz center frequencies, phantom and fresh pig esophagus samples were measured to compare the imaging performance of both detectors.

Chapter 6 introduces two improved approaches to enhance the image reconstruction performance. The fast sparse recovery method is implemented to accelerate the model-based reconstruction process. Besides, a geometrical super resolution approach for optoacoustic image quality enhancement is proposed. These two methods can be used to enhance the image quality of datasets acquired in the curved or linear scanning endoscopy configurations or tomography scanning systems.

Chapter 7 validates the imaging capability of optoacoustic on esophagus samples. High resolution optoacoustic mesoscopy and the developed endoscopy systems are applied to measure pig and human esophagus samples. The frequency bandwidth required for distinguishing layer structures of esophagus wall is investigated.

Finally, the main work of this thesis is summarized and the future developments of optoacoustic endoscopy system are given.

## **Chapter 2      Theoretical and technical background**

This chapter introduces the theory of optoacoustic imaging and the general knowledge of optoacoustic endoscopy.

Section 2.1 describes the main principles of optoacoustic imaging, including the signal generation and sound propagation in tissue.

Section 2.2 analyzes the common reconstruction approaches for optoacoustic imaging, including the backprojection and model-based methods.

Section 2.3 discusses the current implementations of optoacoustic endoscopy and corresponding image display methods.

### **2.1      General knowledge of optoacoustic imaging**

#### **2.1.1      Optoacoustic signal generation and properties**

A. G. Bell first reported the phenomena that sound can be generated by light in 1880. With the development of techniques, optoacoustic imaging based on this phenomenon has shown great potentials in preclinical applications in recent ten years [56-58]. At present, biomedical optoacoustic imaging is a fast-growing field of research. The schematic of a simple optoacoustic imaging system is illustrated in Fig. 2.1. The image object is first illuminated by short pulse laser light in the range of ns. The absorption of light by the object leads to a slight temperature rise. Then the object relaxes by diffusing heat energy and emitting optoacoustic waves [56, 57]. There are two important conditions for optoacoustic signal generation [56, 57]. One is the thermal confinement. It requires that the excitation time should be shorter than it takes for the heat to diffuse to neighbor region, which is characterized by the thermal relaxation time  $\tau_{th}$ . The detailed relationship can be characterized as:  $\tau_{th} = \frac{d_c^2}{D_T}$ , where  $d_c$  is

the targeted resolution element (the minimal diameter of the absorber), and  $D_T$  is the thermal diffusivity (about  $1.4 \times 10^{-3} \text{ cm}^2 \text{ s}^{-1}$  in soft tissue). Generally, the  $\tau_{th}$  should be less than  $1 \mu\text{s}$  [56]. Another condition is the stress confinement, which means that the volume expansion of the absorber during the excitation pulse should be negligible. It requires the stress relaxation time  $\tau_s$  should be less than  $\frac{d_c}{v_s}$ , where  $v_s$  is the speed of sound. For a resolution of  $100 \mu\text{m}$ ,  $\tau_s$  should be less than  $67 \text{ ns}$ . In reality, nanosecond lasers (less than  $10 \text{ ns}$ ) are generally employed [58].

Under thermal and stress confinement, optoacoustic signals can be generated, and ultrasound transducers are used to record optoacoustic waves. Image reconstruction techniques can be applied afterwards to form optoacoustic images. The generation and propagation of the acoustic wave is given by the following wave equation [57, 59, 60]:

$$(\nabla^2 + k_a^2)p(r, t) = -\frac{\beta}{C_p} \frac{\partial H(r, t)}{\partial t} \quad (2.1)$$

where  $p(r, t)$  indicates the acoustic pressure at a position  $r$  and time  $t$ ,  $H(r, t)$  indicates the heating function, which is obtained as a product of absorption coefficient and light fluence.  $\beta$  is the thermal expansion coefficient of the tissue and  $C_p$  is the specific heat at constant pressure.  $k_a$  represents the acoustic wave number given as  $k_a = \omega/v_s$ , where  $\omega$  is the temporal frequency and  $v_s$  is the speed of sound.

Meanwhile, the acoustic pressure at a certain position  $\vec{r}$  inside the object can be expressed as:

$$p_0(\vec{r}) = \Gamma H_r(\vec{r}) = \Gamma \mu_a(\vec{r}) \Phi(\vec{r}) \quad (2.2)$$

Where  $\mu_a(\vec{r})$  is the absorption coefficient of the object (unit:  $\text{cm}^{-1}$ ). The local optical fluence is  $\Phi(\vec{r})$ .  $\Gamma = \beta v_s^2 / C_p$  is the Grüneisen parameter, which describes the conversion properties of the medium [57, 59, 60].

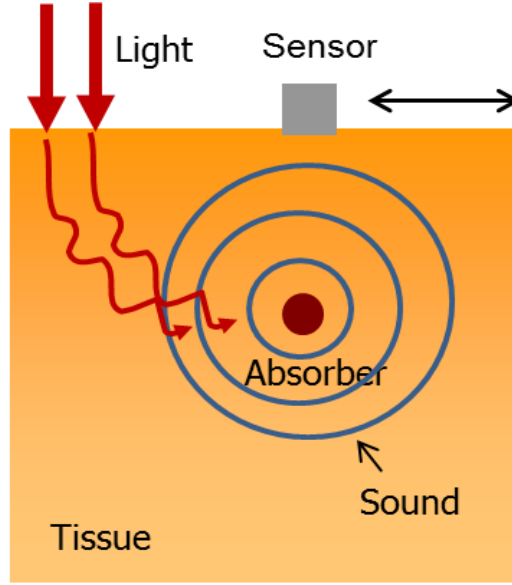


Figure 2.1. Illustration of a prototypic optoacoustic system. The laser light illuminates the tissue sample, and the absorber emits optoacoustic waves. Ultrasound sensors were scanned position by position to collect optoacoustic waves.

The optoacoustic equation Eq. 2.1 can be solved with the Green function approach [60]. Under stress confinement and with delta heating  $H_t(t) = \delta(t)$ , the expression of the acoustic field can be written as:

$$p_\delta(r, t) = \frac{\Gamma}{4\pi v_s^2} \frac{\partial}{\partial t} \left\{ \frac{1}{v_s t} \int_V H_r(r') \delta\left(t - \frac{|r-r'|}{v_s}\right) dr' \right\} \quad (2.3)$$

Where the integration is implemented over the illumination region  $V$ , and  $r'$  is a point within the object. From the equation, it can be explained that a detector at the position  $r$  and time  $t$  senses the integrated sound pressure, originating from optoacoustic point source on a spherical shell with radius  $v_s t$  and center at  $r$ . The optoacoustic signal can be simulated based on the analytical solution of the pressure wave equation for a homogenous spherical absorber with radius  $a$  positioned at  $r_s$ :

$$p_\delta(r, t) = p_0 U(a - |R - v_s t|) \frac{(R - v_s t)}{2R} \quad (2.4)$$

Where  $U$  is the Heaviside function,  $R$  defines as the distance of the absorber from the detection position,  $p_0$  is the amplitude of the initial pressure and  $v_s$  is the speed of sound.

Four spheres with radius  $a = 15, 25, \text{ and } 50 \mu\text{m}$  were simulated and illustrated in Fig. 2.2.

Fig. 2.2(a) shows the duration of the simulated pulse, which correlates with the propagation

---

time of sound along the sphere diameter and scales with the size of the sphere. The theoretical frequency response is obtained by fast Fourier transformation of each simulated optoacoustic signals as shown in Fig. 2.2(b). The frequency spectra are very broad, ranging from low frequencies corresponding to the dimensions of the absorber, to high frequencies generated from the object boundaries. The maximal amplitude of the spectra defines the central frequency  $f_c$  of the source, and the rough approximation of  $f_c$  for a given feature size  $a$  can be defined as:  $f_c \sim \{0.7 \dots 0.8\} \frac{v_s}{a}$ . The full width at half maximum of the lobe defines the bandwidth  $B_w$  of the signal as the ratio  $\frac{B_w}{f_c} = \text{const}$ . It can be noted that the frequency and bandwidth scale with the diameter of the optoacoustic source. The small objects result in higher center frequency and broader bandwidth. Anatomical structures vary from centimeter range to micrometers, thus generates optoacoustic waves from several kilohertz to a hundred megahertz. In reality, however the spectra of the recorded optoacoustic waves are usually narrower than the theoretical values as plotted in Fig. 2.2. First, the limited detection bandwidth of the ultrasound transducers restricts the recorded frequencies. Besides, the image object is hard to be illuminated uniformly as the light fluence rapidly decays towards the center of the sample. Furthermore, the positioning of the object relative to the detector may influence the signal shape. Nevertheless, broadband detection devices are optimal to record optoacoustic signals in order to enhance the image quality.

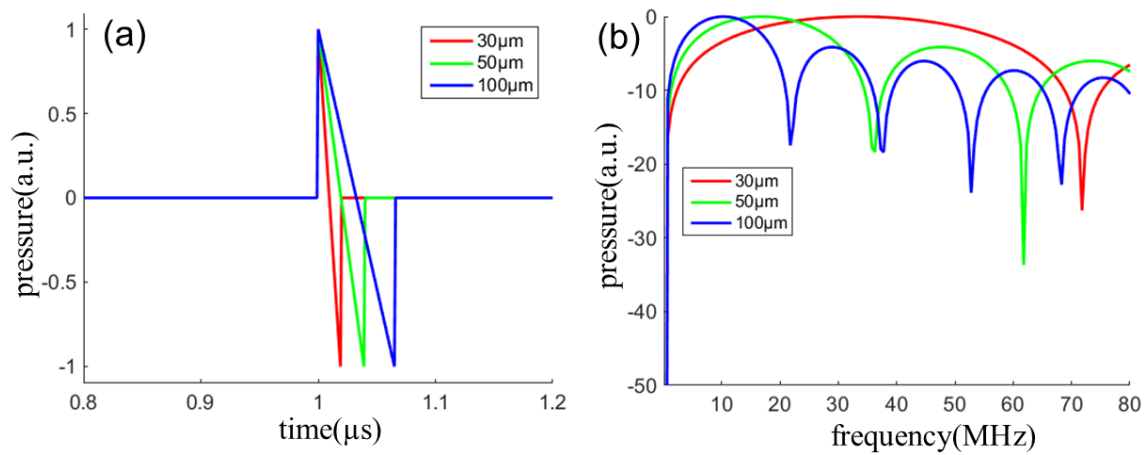


Fig. 2.2. Ideal optoacoustic signals from simulated spheres with different diameters: 30  $\mu\text{m}$  in red, 50  $\mu\text{m}$  in green and 100  $\mu\text{m}$  in blue respectively. The time signals are presented in (a) and the corresponding frequency spectra are shown in (b). The diameter of the spheres determines the maximum frequency. The larger sphere contains lower frequency components.

The amplitude of the generated optoacoustic waves is proportional to the absorbed laser energy, which describes the map of the optical absorption properties of tissue [56-58]. Important intrinsic absorbers in biological tissue are oxygenated ( $\text{HbO}_2$ ) and deoxygenated (HHb) hemoglobin, tissue pigments like melanin and lipids [51]. Fig. 2.3 shows their absorption spectra. We can see the absorption of these pigments is strongly sensitive to the wavelength. At shorter wavelengths, like the visible range, hemoglobin absorption is much higher and can exceed that of other chromophores by more than two orders of amplitude. It is the very strong preferential absorption of hemoglobin that enables the vasculature to be visualized with high contrast in optoacoustic imaging. In this work, the wavelength of 532 nm is used to characterize the vasculature structure of tissue measurements. The optical absorption of hemoglobin drops two orders of magnitude in the range of 650-900 nm, where light can penetrate relatively deep up to several centimeters. Otherwise, light penetration is hindered by the absorption of hemoglobin or water.

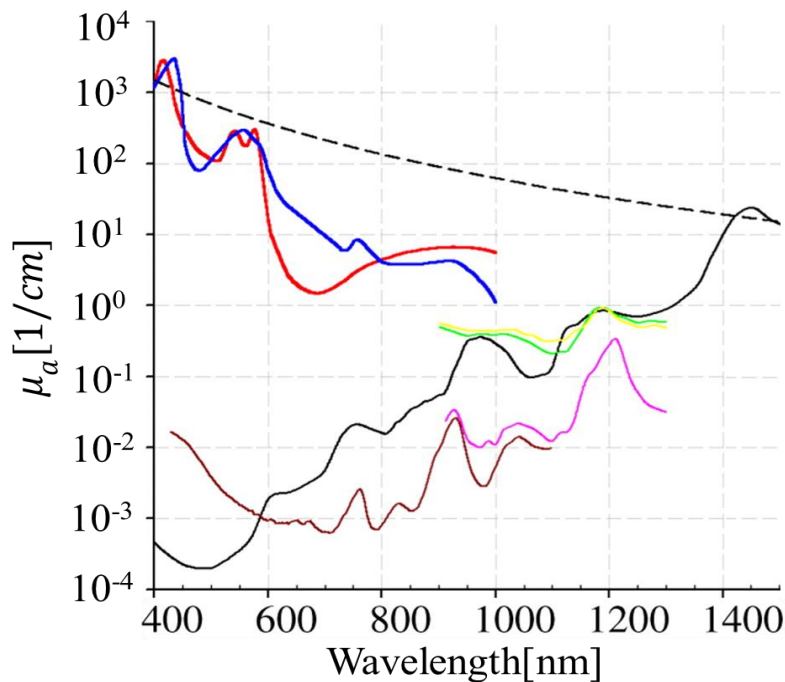


Fig. 2.3. Absorption coefficient spectra of several endogenous tissue chromophores. Red line: oxyhemoglobin, blue line: deoxyhemoglobin, black line: water, brown line: lipid (a) (20% by volume in tissue), lipid (b), pink line, black dashed: melanin, Collagen (green line) and elastin (yellow line) spectra. Data compiled by Scott Prahl, Oregon Medical Laser Center (<http://www.omlc.ogi.edu/spectra>).

Besides intrinsic absorbers, different types of exogenous contrast agents can be used to highlight specific biological target because of their high absorption. For example, organic dyes, such as indocyanine green (ICG) has been widely used in clinics [48]. Beside, nanostructures, such as nanorods or nanoparticles, can be used for preclinical measurements [48]. Through adjusting their properties, the peak absorption wavelength can be tuned to NIR wavelengths, which can enhance the penetration depth. More importantly, multispectral optoacoustic tomography can identify or even quantify sources of contrast according to their absorption spectra based on the unmixing techniques [6, 48].

### 2.1.2 Penetration depth

It is known that light scattering is very strong in biological tissue in the visible and NIR wavelength range [9]. As for pure optical imaging approaches, the directionality of light is rapidly degraded over 1 mm depth, resulting in the degradation of spatial resolution [9]. For example, optical coherence tomography, which depends on the backscattered light, can

achieve maximum 1.5 mm imaging depth [39]. However, the scattering of sound is orders of magnitude lower in tissue than light, which allows the absorbers to be resolved with a high spatial resolution even though the illumination light is diffused [9]. Therefore, optoacoustic imaging can achieve much deeper imaging depth with high resolution comparing to pure optical imaging modalities.

Penetration depth is a very important factor to evaluate the imaging technique. For optoacoustic, the imaging depth is limited ultimately by optical and acoustic attenuations. For soft tissue, optical attenuation determines the imaging depth although acoustic attenuation is significant. Optical attenuation is dependent on both the absorption and scattering coefficients, which is strongly wavelength-dependent [51]. The optical attenuation coefficient  $\mu_e$  is derived from the diffusion theory and expressed as  $\mu_e = (3\mu_a(\mu_a + \mu'_s))^{1/2}$ , in which  $\mu_a$  and  $\mu'_s$  are the absorption and reduced scattering coefficients. In homogeneous scattering media, light becomes diffuse beyond the mean free paths (approx. 1 mm), and the irradiance decays exponentially with depth [9].  $1/\mu_e$  is the depth at which the irradiance has decreased by  $1/e$  and termed the penetration depth. For example, at wavelength of 700 nm,  $\mu_s$  is set the value of  $1.6 \text{ cm}^{-1}$ [9].  $\text{HbO}_2$  and  $\text{HHb}$  are the main absorbers. The  $\mu_e$  is approximate as  $0.13 \text{ mm}^{-1}$ . The optical penetration depth  $1/\mu_e$  is thus about 8 mm. This means light is attenuated by approximately a factor of 4 for each additional centimeter depth. Accounting with the acoustic attenuation, the total attenuation of sound and light is thus over one order of magnitude per centimeter [51]. Despite this, optoacoustic imaging has demonstrated several centimeters penetration depth through optimization of wavelength, light delivery approach and high sensitivity transducers. In this work, the wavelength of 532 nm is mainly used to characterize the vasculature structure of samples. Light penetration is hindered by the absorption of hemoglobin and thus achieved few millimeters penetration depth in general.

### **2.1.3 Acoustic reflection and attenuation**

When optoacoustic waves propagate through tissue, several issues are needed to be considered for the reconstruction process, like acoustic reflection and attenuation.

#### *A. Acoustic reflection*

Acoustic reflection takes place at the interface between two media with different acoustical properties. Because of the acoustic impedance mismatch, partial acoustic waves are reflected back. If the impedance difference between the two media is large, the relative amplitude of the wave transmitted to the second medium is very low, resulting in low SNR of recorded optoacoustic signals. This explains why acoustic coupling medium is needed between tissue and ultrasound detector. In biological tissue, acoustic inhomogeneity is more common, resulting in degradation of reconstruction. For example, boundaries between tissues and bones can cause serious acoustic reflection, producing artifacts in the reconstructed image[61].

### *B. Acoustic attenuation*

Frequency dependent acoustic attenuation is an important factor, which can affect optoacoustic signals transmission and image reconstruction. This phenomenon is generally determined by the frequency spectra of ultrasound signals, the acoustic and thermodynamical properties of the medium [62, 63]. In optoacoustic imaging, the ultrasonic waves are generated by thermal expansion of structures with varying dimensions resulting in very broad signal bandwidth [62, 63]. Normally it ranges from few kHz up to 100 MHz or more. In the low-megahertz frequency range, acoustic waves in tissue have the properties of low scattering and deep penetration. The attenuation is temperature and frequency dependent. The frequency dependency of acoustic attenuation can be represented by the expression  $\mu = af^b$ , where  $\mu$  is the attenuation coefficient,  $a$  and  $b$  are constants,  $f$  is the frequency of sound [57]. A mean value of acoustic attenuation equals about  $0.6 \text{ dB cm}^{-1}\text{MHz}^{-1}$  for soft tissue. The attenuation increases with the frequency and the penetration depth decreases with the frequency. Since spatial resolution depends ultimately on the frequency content recorded by the detector, frequency-dependent acoustic attenuation limits the maximum frequency content and thus defines the ultimate practically achievable spatial resolution limit.

For simplicity, optoacoustic reconstruction algorithms usually do not consider the acoustic reflection and attenuation issues. However, acoustic reflection and attenuation can induce artifacts and degrade image resolution. Therefore, an improved image reconstruction method will be introduced in chapter 6 to solve these issues.

## 2.2 Optoacoustic image formation

Optoacoustic images reconstructed from a set of measured optoacoustic signals reflect the absorbed energy distribution. The easiest case relies on the focusing ability of transducers or using focused light. By scanning the focused detector or light, a sequence of A-scan images is acquired, and optoacoustic images can be formed by aligning A-scan images in the focusing regions. This image formation method does not require computational reconstruction and is frequently used in the fields of optoacoustic microscopy [5, 47]. Besides, several reconstruction schemes are employed for optoacoustic tomography. The spherical radon transform also known as backprojection, is widely used due to its simple implementation and high efficiency. Model-based approaches are capable of incorporating information regarding the detection geometry, acoustic attenuation, and transducer properties in the reconstruction process, resulting in more accurate reconstruction [64, 65].

### 2.2.1 Backprojection algorithm

The backprojection algorithm is an analytical solution to Eq. 2.1 under assumption of thermal and stress confinements, and delta heating. The pressure wave at time instant  $t$  and at position  $r$  is given by [57, 59, 60]:

$$p(r, t) = \frac{\Gamma}{4\pi c} \frac{\partial}{\partial t} \int_{S'} \frac{H(r')}{|r-r'|} dS' \quad (2.5)$$

$S'$  is a spherical surface (or arc in the 2D case) with  $|r - r'| = ct$ .  $H(r')$  is the optical absorption distribution, i.e., the amount of energy absorbed in the tissue per unit volume,  $c$  is the speed of sound in the medium and  $\Gamma$  is the Grueneisen coefficient (dimensionless) [59]. Optoacoustic image reconstruction then inverts Eq. 2.5 to retrieve the absorbed energy distribution  $H(r')$  based on a set of measured optoacoustic signals  $p(r, t)$  (projections). Several reconstruction approaches exist for this purpose [57, 59, 66]. Herein, we use an approximate version of the backprojection algorithm, which is expressed in discrete form as [61, 66, 67]:

$$H(r'_j) = \sum_i \left\{ p(r_i, t_{ij}) - t_{ij} \frac{\partial p(r_i, t_{ij})}{\partial t} \right\} \quad (2.6)$$

Where  $r_i$  is the position of the  $i$ -th measurement point,  $r_j'$  the position of the  $j$ -th point in the region of interest, and  $t_{ij} = |r_i - r_j'|/c$ . The backprojection method is also known as delay-and-sum beamforming technique and spherical radon transform. This method can be easily implemented for different detection geometries. Time-resolved optoacoustic signals are backprojected to spherical shells and then summed them up in order to form an image. This method is very efficient and has been widely used to reconstruct large amount of data for real-time optoacoustic imaging.

However, the backprojection method uses the time derivative term as an approximation to reconstruct. Since derivative time acts as a ramp filter in the frequency domain, backprojection method enhances image boundaries while leads to the loss of low frequency information. Additionally, negative values appearing in the reconstructed image limit the applicability of the method for quantitative imaging. Besides, factors such as the transducer properties or variations of speed of sound cannot be taken into account in the backprojection formula, which degrades the reconstruction accuracy.

### 2.2.2 Model-based algorithm

Model-based methods are based on numerically modeling the forward optoacoustic problem and using that model in an optimization algorithm [64, 65]. A model of optoacoustic signal propagation is built on a grid. This model can then be inverted and multiplied with the measured signals to form an optoacoustic image. The integral in Eq. 2.5 is discretized to form a model matrix using an interpolated model matrix method, resulting in the following matrix equation,

$$Ax = b \quad (2.7)$$

Where  $b$  is the recorded data and  $x$  is the reconstruction image.  $A$  is obtained by linear interpolation of the heating function over the image grid. Efficient inversion of Eq. 2.7 requires regularization. We selected conventional Tikhonov regularization with parameter ( $\lambda$ ), and assuming an initial pressure rise distribution is smoothly varying. The objective function to be minimized in this case is given as,

$$\Omega = \|Ax - b\|_2^2 + \lambda \|x\|_2^2 \quad (2.8)$$

whereby  $\| \cdot \|_2$  represents the L2 norm. The above objective function can be solved using normal equations [68], *i.e.*,

$$x_{tikh} = (A^T A + \lambda I)^{-1} A^T b \quad (2.9)$$

However, Eq. 2.9 is computationally expensive due to the time-consuming matrix inversion. Alternatively, the LSQR approach can be employed [69], *i.e.*

$$x_{LSQR} = V_k ((B_k^T B_k + \lambda I_k)^{-1} \beta_0 B_k^T e_1) \quad (2.10)$$

where  $B_k$  represents a bi-diagonal matrix,  $V_k$  is the right orthogonal matrix resulting from Lanczos bidiagonalization [69, 70] and  $\beta_0$  is defined as  $\|b\|_2^2$ .  $e_1$  is  $[1 \cdots]^T$ . Eq. 2.10 can be inverted in a faster fashion compared to Eq. 2.9 since it involves inverting the diagonal matrix, which is computationally efficient.

Model-based algorithms show superior performance over analytical techniques. The main reason is that model-based method can integrate the characteristics of the transducer and other properties of light and sound transmission into the reconstruction model, resulting in more accurate reconstruction. However, model-based methods usually require large numbers of repeated sparse matrix-vectors multiplications in an iterative manner, causing significant computational cost [65, 71]. Accelerated model-based methods are developed to reduce the computation cost [71-73]. For example, the angular discretization method was used to generate the model matrix, which effectively reduced the computational cost and saved memory [71, 72]. Other approaches performed inversion on parallel-processing platforms based on graphics processing units (GPU), which enabled real-time model-based reconstruction [73, 74]. In chapter 6, a fast model-based reconstruction approach is proposed to reduce the computation time and enhance the image quality of limited view scenarios.

## 2.3 Technical aspects of optoacoustic endoscopy implementation

### 2.3.1 Existing configurations

As mentioned, optoacoustic imaging has shown great potential for clinical applications. Label-free optoacoustic technique in particular is well suited for endoscopy [75] and disease detection can be enhanced via the application of multispectral optoacoustic tomography [6].

Several optoacoustic endoscopy implementations and animal measurements have been proposed [50, 52-55, 76-79]. The first example of optoacoustic endoscopy was a probe for 1D sensing of treatment depth after photodynamic therapy [76]. High frequency intravascular imaging catheters have been used for optoacoustic sensing of rabbit arteries [80]. Initially using outside illumination and *ex vivo* imaging, these approaches have now evolved and shown the possibilities of using an integrated illumination and detection system to improve the feasibility of *in vivo* intravascular optoacoustic imaging [77, 78]. The gastrointestinal tract of a rat was imaged *ex vivo* using a 4.2 mm diameter optoacoustic imaging probe comprising an integrated light guiding optical fiber, an ultrasonic detector and a mechanical rotating acoustic and optical reflector for sectorial B-scan imaging [53]. This system was further miniaturized to 3.8 mm equipped with a spherical focused ultrasound transducer to enable simultaneous optoacoustic and ultrasonic endoscopy of the esophagus, the colon and the lymphovascular system near the colon of a rat *in vivo* [52]. Recent implementations of the system achieved additional size reduction to 2.5 mm to fit through the working channel of a standard colonoscopy for endoscopic guidance [55]. Optoacoustic endoscopes operating on ultrasonic diffraction limitations using focused ultrasound detectors, could achieve lateral resolution spanning from hundreds to tens of micro-meters with an imaging depth up to several millimeters. Such acoustic resolution optoacoustic endoscopes (AR-OE) have been showcased to provide high-resolution visualization of the intestinal vasculature of small animals *in vivo* [52, 54, 81, 82]. Even higher resolution can be achieved by optical-resolution optoacoustic endoscopy (OR-OE) using a focused laser beam, in analogy to intra-vital optical microscopy [79, 83-86].

In general, the typical configurations of optoacoustic endoscopy implementations can be divided into two categories. The first one is simply aligning the illumination fiber with the ultrasound detector, which makes the light overlaying with the detection view of the transducer as illustrated in Fig. 2.4(a). Such implementation has been widely used in optoacoustic intravascular imaging, where a single element transducer is used to record signals, such as IVUS detector [50, 78, 87]. The diameter of the IVUS based endoscopic probe can be minimized to 2 mm or even smaller. For such implementation, the working distance of the endoscopic probe is determined by the overlay region between the

illumination light and the detection view of ultrasound detectors. Normally the working distance of such probe is limited to few millimeters. In order to get volumetric images, proximal translational and rotation stages are required, and torque coils are used to transfer the pulling and rotating force to scan the probe. This design has a quite simple structure without complex components inside the probe. The image resolution is usually determined by the focusing properties of ultrasound transducers as no reconstruction method is employed. Currently, high frequency intravascular imaging catheters have been reported for detecting optoacoustic waves from *in vivo* rabbit arteries [50, 78, 87]. Optoacoustic endoscopy probe based on IVUS transducers in this configuration will be further introduced in chapter 3 and 4.

Another representative implementation as illustrated in Fig. 2.4(b) has a more complex structure. Ultrasound transducer with a hole in the center is used to record optoacoustic waves. Illumination fiber passes through the hole, leading to a coaxial overlay between the detection view of the transducer and the light. In order to get side-view detection, a reflector that can reflect both light and sound is used to redirect the detection path. As shown in Fig. 2.4(b), a micro rotation motor connected to the reflector is used to get a full view scanning. For this implementation, the illumination and detection components keep stationary, thus effectively reduce motion during scanning. By gradually pulling the probe, 3D images can be formed. Due to the coaxial overlay between the illumination and detection, this probe has longer imaging distance in principle. In order to improve the image quality, focused ultrasound detectors are applied to improve the lateral resolution. Thus the working distance is determined by the focal length of the detector. Even though micro-motor avoids rotating the whole probe, the micro-motor itself will take space, increasing the diameter and length of rigid part of the endoscopic probe. Nevertheless, such endoscopic implementations have demonstrated the ability of imaging small animals *in vivo* [53]. For example, an optoacoustic endoscopic probe with 3.8 mm in diameter and about 38 mm long was developed for imaging gastrointestinal tracts of rabbits and rats *in vivo* [53]. This system enabled simultaneous optoacoustic and ultrasonic imaging of the esophagus, colon and neighbor tissue. Recent implementations of the system featured an additional size reduction to 2.5 mm to fit through the working channel of a standard video endoscopy [55].

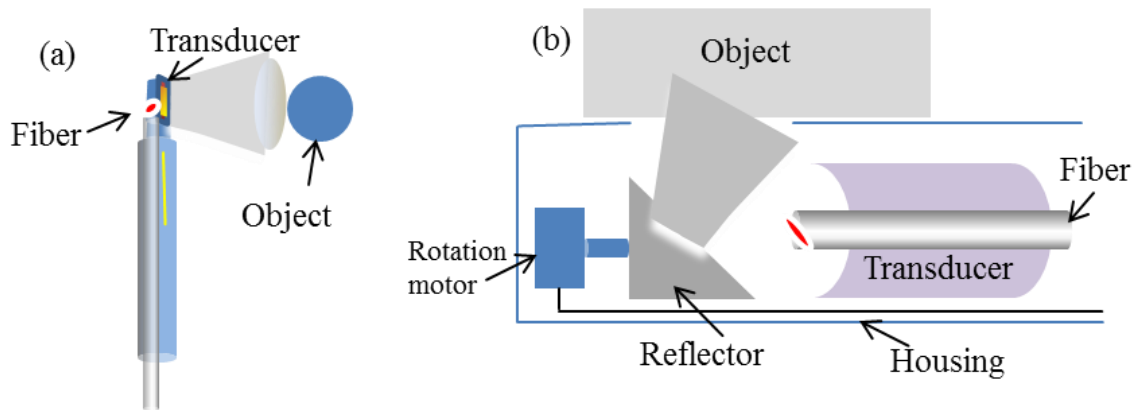


Fig. 2.4. (a) Schematic of the single alignment design. (b) Implementation with micro-reflector.

### 2.3.2 Ultrasound transducers

In order to minimize diameters of endoscopy probes, ultrasound sensors with limited size are usually used to record optoacoustic signals. In this work, IVUS transducers and spherical focused detectors are employed for endoscopy implementations. The corresponding endoscopy systems based on these two types of transducers will be introduced in Chapter 3 and 4. The main properties are introduced here:

#### (a) Intravascular ultrasound detector

IVUS detectors commercially used in clinical intravascular ultrasound applications has been widely applied to intravascular optoacoustic imaging [77, 80, 88, 89]. The diameter of IVUS detectors can be minimized to few hundreds of micros. According to different applications, IVUS transducers with different center frequencies are manufactured, ranging from few MHz to 80 MHz [78]. Generally, the detection field of IVUS can be divided into near field and far field. The near field area is adjacent to the transducer face and has a converging beam profile, which has high sensitivity. Because of its good detection directionality, IVUS can achieve similar image quality in the near field. However, the detection sensitivity decreases in the far field and the detection aperture gets expanded. As shown in Fig. 2.5(a), the near field length is dependent on the diameter ( $d$ ) and center frequency of the transducer ( $F$ ):  $L_N = \frac{d^2}{4\lambda} = \frac{d^2 F}{4V}$ , where  $V$  is the velocity of sound in the material. For example, for a 15 MHz IVUS detector with diameter of 0.8 mm, the length of near field length  $L_N$  is about 3.7 mm. In the near field,

the signal amplitude is relative constant, while it drops dramatically in the far field as illustrated in Fig. 2.5(a). The corresponding simulated sensitivity field of the 15 MHz IVUS is illustrated in Fig. 2.5(b).

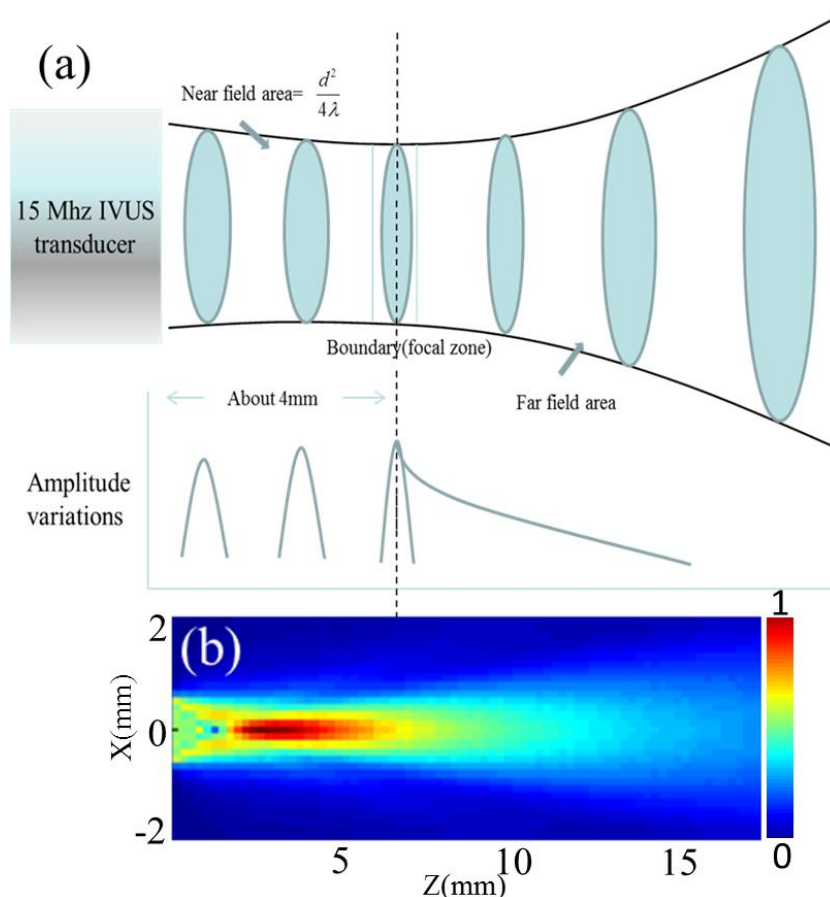


Fig. 2.5. (a) Illustration of the detection properties of 15 MHz IVUS sensor in the near field and far field. (b) Simulated sensitivity of a 15 MHz IVUS detector.

A single 100  $\mu\text{m}$  microsphere was imaged by the 15 MHz IVUS detector at different depths. The result is shown in Fig. 2.6(a). The lateral resolution characterized by the FWHM (Full Width Half Maximum) value is displayed in Fig. 2.6(b). It can be seen the lateral resolution varies slightly in the near field (below 5 mm) and decreases rapidly in the far field. The SNR values (determined by the ratio of the maximum signal intensity to the stand deviation of the background) shown in Fig. 2.6(c) reveals that the signal intensity gradually increases in the near field and drops rapidly in the far field.

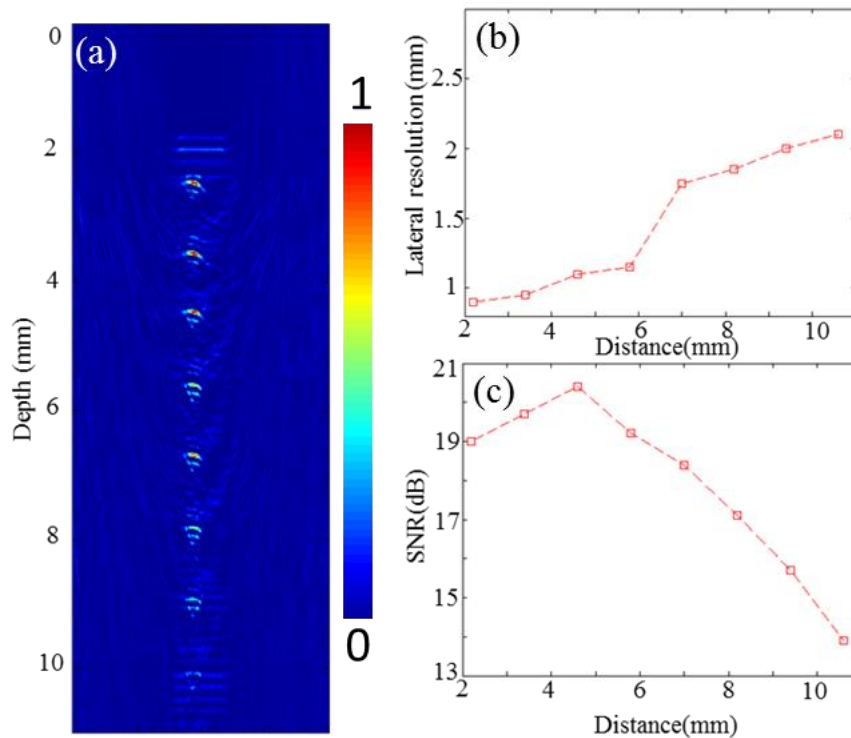


Fig. 2.6. (a) Optoacoustic images of a 100µm microsphere at different depths. (b) Lateral resolution changes along the depth direction; (c) SNR changes along the depth direction.

### (b) Focused detector

Currently there is no effective reconstruction approach to enhance the image quality of the radial scanning optoacoustic endoscopy (detailed analysis is presented in the coming section). Thus the lateral resolution is determined by the focusing properties of the transducer. To enhance the resolution, focused ultrasound transducers can be applied to achieve high resolution images in the focused region. For example, a spherical focused detector with a focal length of 7 mm is used for endoscopy implementation and the details will be introduced in the chapter 4. The simulated sensitivity fields of this transducer are shown in Fig. 2.7(a). From the simulation, we can see the length of the focal zone is about 2 mm. In the region outside of the focal zone, the resolution decreases rapidly. A 10 µm suture was scanned by this detector along the depth direction and the corresponding image was displayed in Fig. 2.7(b). High resolution images of sutures (thread with high absorption) were acquired inside the focus, while they elongated outside of the focal region.

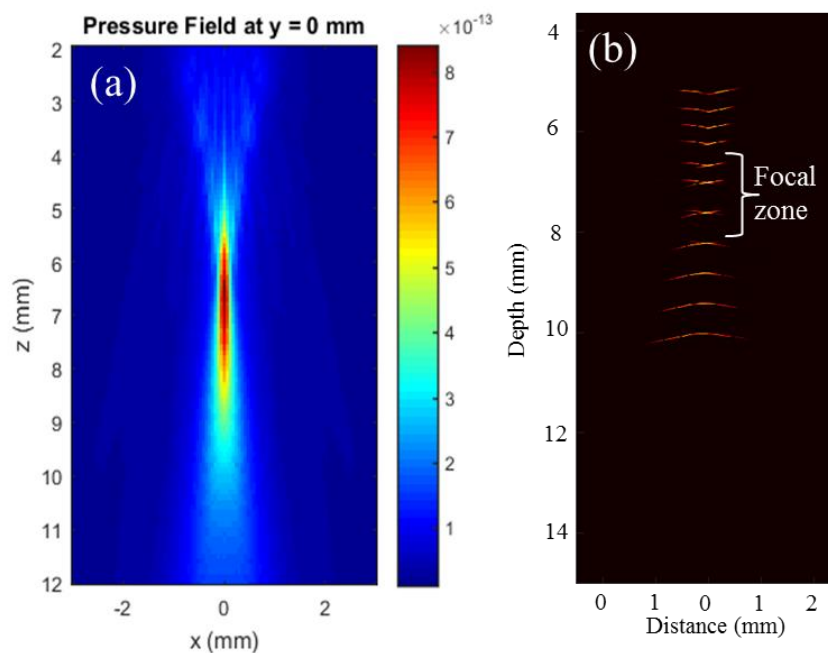


Fig. 2.7. (a) Simulated sensitivity field of the focused detector. (b) Optoacoustic image of a 10  $\mu\text{m}$  suture measured at different depth.

### 2.3.3 Image display approaches

For optoacoustic endoscopy, the image reconstruction method is determined by the scanning geometries. If the ultrasound detector is scanned linearly or along a small arc, computational methods can be applied to improve the image quality. Endoscopy implementations with linear or curved scanning geometries will be introduced in Chapter 3 and corresponding image reconstruction approaches are described in Chapter 6. Here the imaging formation methods for the radial helical rotation scanning are discussed. For the radial scanning geometries, image formation is based on measurements capturing only a small acceptance angle of the ultrasound field emitted from tissue. Although optoacoustic image reconstruction methods in the frequency and time domains have been extensively studied, few stable optoacoustic reconstruction algorithms are available for the radial scanning mode [57, 90]. The reason can be contributed to the special scanning geometry. When the endoscopy probe revolves around its axis inside the luminal organ, the image object cannot be immersed and only a small acceptance angle of the ultrasound field emitted from the object is captured. Besides, the illumination moves with the detector in the radial scanning mode and the

distance between the detector and object is not constant. All of these factors limit the performance of backprojection or mode-based reconstruction methods on the radial scanning geometry. Therefore, optoacoustic images acquired in the radial scanning geometry are currently displayed by converting detected optoacoustic waves in polar coordinates into Cartesian coordinates. Hilbert transform is often used to enhance the envelope of optoacoustic signals.

## 2.4 Summary and discussion

In the first section of this chapter, the theoretical background of optoacoustic imaging was introduced. The theory of optoacoustic signal generation was explained in details. The thermal and stress confinements were used to define the requirements for optoacoustic signal generation. Afterwards, the analytical estimation of optoacoustic signal intensity was given based on the absorption coefficient and light fluence. The acoustic reflection and attenuation issues were studied to understand the behavior of optoacoustic wave propagation in soft tissue. Besides relying on the focusing properties of transducers, computational reconstruction methods, including backprojection and model-based methods were introduced separately in the second part of this chapter. In the last section, representative implementations of optoacoustic endoscopy were introduced as well as the detection properties of common ultrasound transducers used for optoacoustic endoscopy. The representative IVUS and focused detectors were characterized respectively.

## **Chapter 3     Implementations of optoacoustic endoscopy probes**

In order to optimize the development of optoacoustic endoscopy system, several implementations of optoacoustic endoscopy probes were built based on different scanning geometries, transducers and illumination settings and then tested on phantoms and biological samples to analyze the imaging performance.

Section 3.1 presents a curved endoscopy probe. The curved geometry offers larger effective acceptance angle, which can improve image quality compared to rotational systems. Phantom and tissue experiments are conducted to test its performance.

Section 3.2 describes the hybrid optical and acoustic resolution optoacoustic endoscopy probe. Laser light is transmitted to tissue by two types of illumination for achieving optical and acoustic resolution imaging. The hybrid endoscopy system can gain optical resolution imaging of the surface and tomography imaging for the deeper features.

Section 3.3 introduces a transducer array based endoscopy probe. This section investigates the merits and imaging performance achieved with a miniaturized linear transducer array. Phantom and tissue measurements are conducted to demonstrate the implementation concept for real-time multispectral imaging and investigate its imaging performance as a function of different detector configurations.

Section 3.4 summarizes this chapter and discusses future developments.

### **3.1 Curved endoscopy probe**

Current endoscopy probes are mostly scanning in radial scanning mode. Radial mode means the detector incrementally revolves around its axis while B-scan images are captured. This

radial mode arrangement can be easily controlled to get cross-sectional images of luminal organs. However, image formation in the radial mode is based on measurements capturing only a small acceptance angle of the ultrasound field emitted from tissue, which may compromise image performance compared to systems using a larger ultrasound collection aperture. In this part, we interrogate the merits of optoacoustic endoscopy implemented by translating a sound detector in linear or curved geometries. The linear and curved detection geometries are achieved by employing an intravascular ultrasound transducer within a plastic guide shaped to a line or a curve. This geometry offers larger effective acceptance angle, along the direction of image formation, which can improve image quality compared to rotational systems [54]. Linear scanning only detects a small fraction of the view offered by rotational systems; however the technique can be combined with conventional optical endoscopy approaches, for example by inserting the optoacoustic detector through the working channel of an optical scope. Therefore linear scanning offers a different working approach in optoacoustic endoscopy.

### 3.1.1 Endoscopy probe implementation

A schematic of the endoscopy system and a photograph of the distal end of the proposed curved optoacoustic tomography endoscopy probe are shown in Fig. 3.1(a) and (b), respectively. A commercial IVUS sensor (2.5-Fr, Atlantis SR Pro, Boston Scientific, Natick, MA) with a center frequency of 15 MHz is used for signal detection. This IVUS detector has the same properties as the one introduced in last section of this chapter. The transducer was inserted in the bigger lumen of a two-lumen flexible polyethylene terephthalate (PET) tube (Boston Scientific, USA) with an outer diameter of 2.5 mm. The transducer could be translated within the lumen using a proximal translation stage. A curved metal wire (0.5 mm in diameter) was inserted into the second lumen of the tube to give the tube a specific shape. This defined the detection geometry. The tube was cut open at the sensing side of the transducer to improve propagation of sound. For illumination we used a nanosecond pulsed laser (Phocus, Oportek USA). The illumination wavelength was 700 nm. A fiber bundle was used to guide laser light onto the sample. The light fluence at the surface of the sample was  $18 \text{ mJ/cm}^2$ . The detected acoustic signals were amplified by 63 dB (AU-1291, Mited Inc., Hauppauge, New York, USA) and recorded with the data acquisition card.

Two imaging configurations were investigated, *i.e.* a linear geometry with the ultrasound element scanned along a straight line and a curved geometry with the ultrasound element scanned over a  $90^\circ$  arc with a radius of 22.6 mm as shown in Fig. 3.1(b). The length of the scanning aperture was 36 mm in both cases and data from 200 consecutive scanning positions averaged over 5 laser pulses were acquired. The signals measured were deconvolved with the electrical impulse response of the system and bandpass filtered between 1-20 MHz. Then image reconstruction was performed using filtered back-projection [91]. Negative values resulting from the use of an approximate algorithm were set to zero.

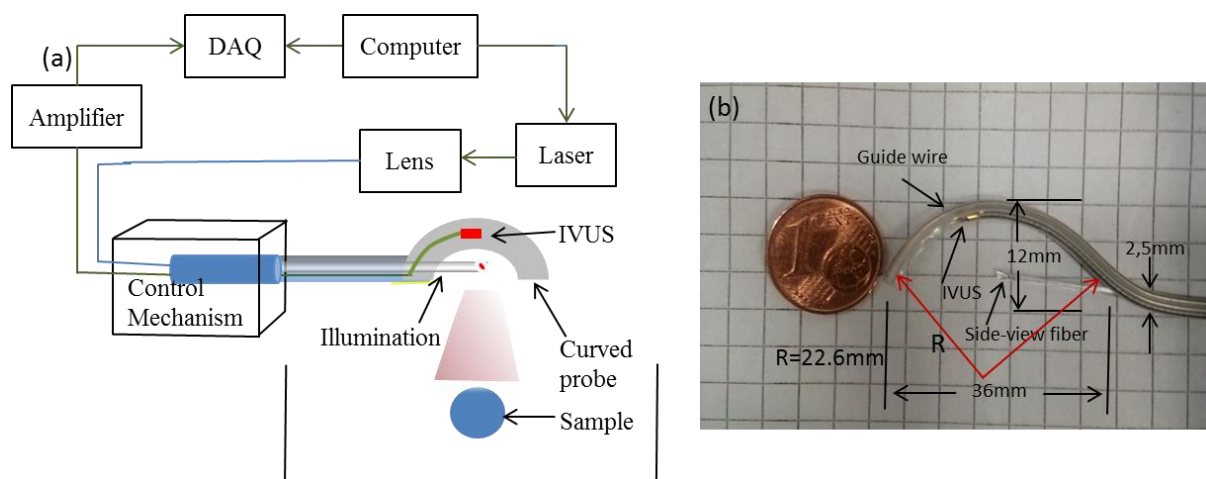


Fig. 3.1. (a) Schematic illustration of the imaging setup. (b) Photograph of the distal end of the curved endoscopy probe.

### 3.1.2 Characterization measurements

To characterize the resolution and overall imaging performance of the system under defined conditions we constructed a phantom of black polyethylene microspheres (Cospheric BKPMS; diameter range 180–210  $\mu\text{m}$ ), embedded in a 1.9 cm diameter 2% w/v agar (Sigma, Germany) cylinder [Fig. 3.2(a)]. Images obtained from the linear geometry [Fig. 3.2 (b)] and curved geometry [Fig. 3.2(c)] reveals the imaging ability of the two implementations. The image obtained by linear scanning shows, as expected, a lateral elongation of the reconstructed microspheres. The image also contains some visible artifacts. Conversely, the image obtained by the curved geometry exhibits better definition of the actual size and shape of the spheres and reduces the appearance of artifacts. Fig. 3.2(d) shows the profiles obtained

through the images of the microspheres along the direction of detector translation and confirm a significant improvement of lateral resolution. For example, the resolution characterized as the FWHM along the lateral direction of microsphere 3 is improved from 520  $\mu\text{m}$  in linear mode to 207  $\mu\text{m}$  in curved mode, the latter value representing the true size of the sphere.

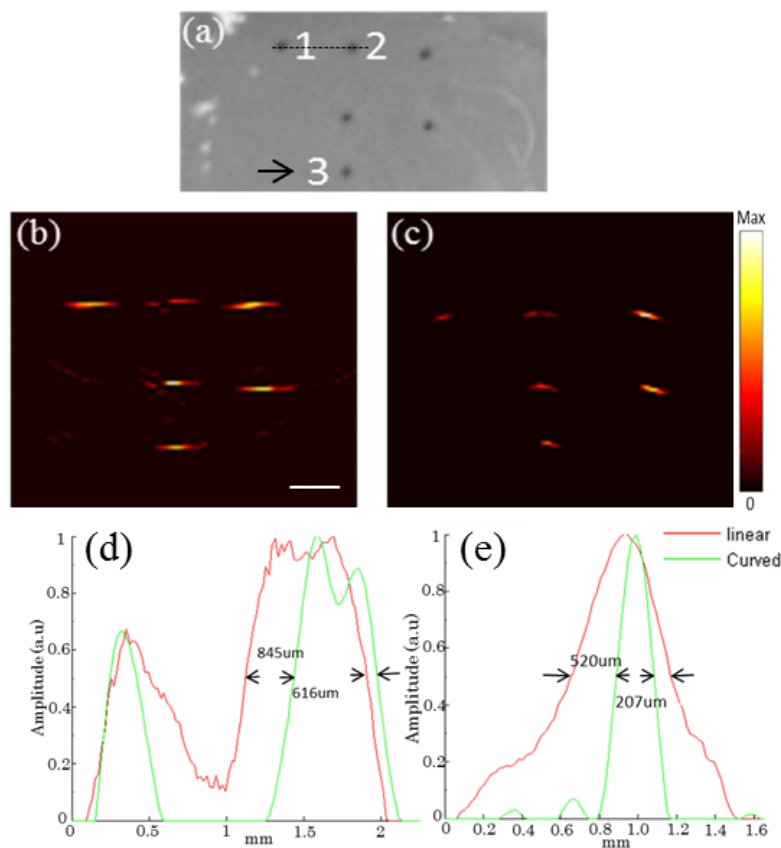


Fig. 3.2. (a) Photograph of the microsphere phantom. (b) The result in the linear geometry and (c) in the curved geometry. (d) The lateral profile (the black dash line) through microsphere 1 and 2, respectively and (e) the profile through microsphere 3 (the black arrow). Scalebar 1 mm.

A second phantom was built to examine the imaging fidelity in resolving more complex patterns. The phantom was constructed by printing a pattern of circles, a line and a triangle on a sheet of paper using a laser printer. The phantom was similarly embedded in a 1.9 cm diameter 2% w/v agar cylinder. An illustration of the 2D phantom is shown in Fig. 3.3(a). Reconstructed results of linear and curved configurations are then shown in Fig. 3.3(b) and (c), respectively. In analogy to the microsphere phantom, the reconstruction in the curved

geometry better resolves the absorbing features of the phantom and shows fewer artifacts compared to the results obtained in the linear geometry. Fig. 3.3(c) correctly captures the size of the big circles measuring double the diameter of the small circles as printed on the phantom. However in the linear mode, those features are hardly resolved and the circles cannot be clearly identified as circular objects in Fig. 3.3(b). The shape of all objects is better resolved and appears more continuous in the curved scan than in the linear scan.

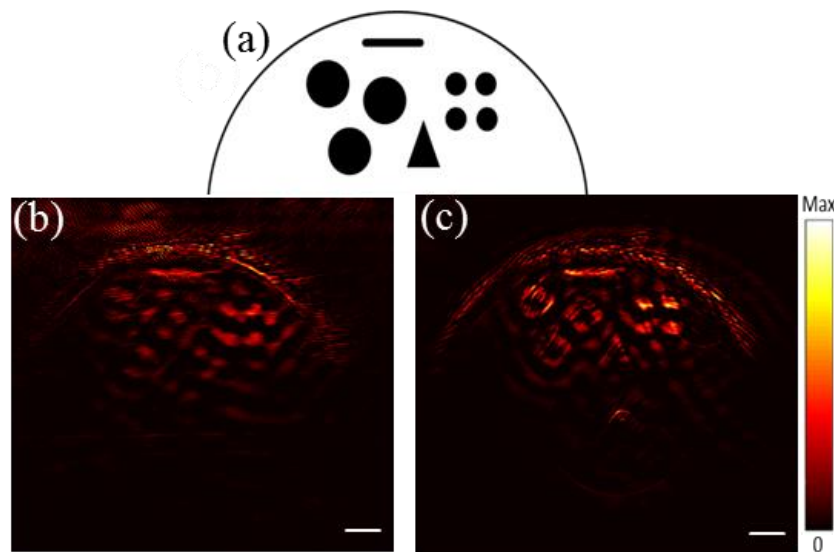


Fig. 3.3. (a) Illustration of the pattern printed onto the paper phantom. Reconstruction results in the linear (b) and curved (c) mode. Scalebar 1 mm.

To examine the characteristics of the two geometries *in vivo*, we employed a four-week-old athymic nude-Foxn1<sup>nu</sup> mouse with a 4T1 subcutaneous tumor. All procedures were approved by the District Government of Upper Bavaria. The mouse was anesthetized under 1.8% isoflurane anesthesia. Sound coupling was achieved using a water bed where the tumor was immersed, whereby the mouse was kept outside the water and its body temperature was maintained at 36 °C. Fig. 3.4(a) shows a photograph of an *ex vivo* cryoslice through the 4T1 tumor, in a plane that is approximately the same as the one imaged in the two scanning configurations. The corresponding reconstructions of the linear and curved modes are presented in Fig. 3.4 (b) and (c). The tumor boundaries are resolved with higher contrast in the curved mode geometry, compared to the linear mode. The overall resolution achieved is also better in curved scanning mode, as evident in the insets of Fig. 3.4(b) and (c).

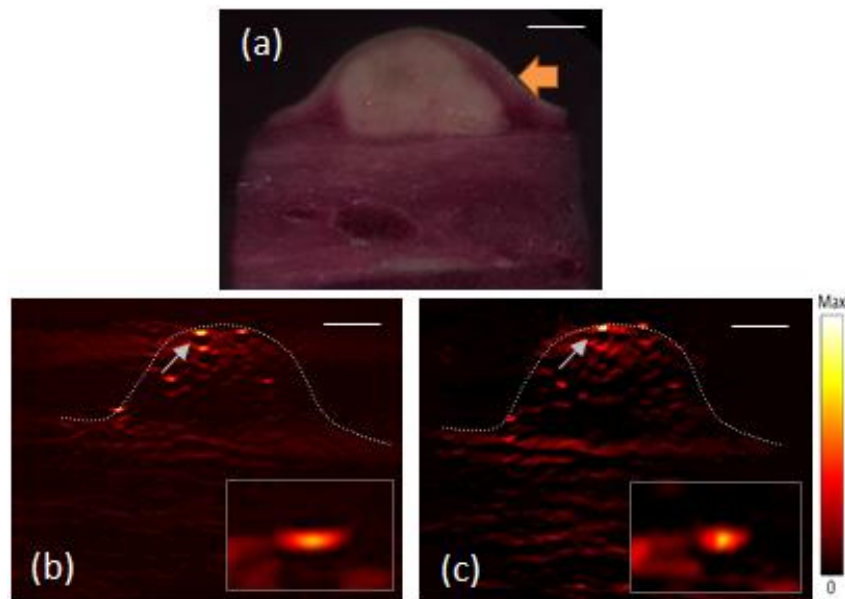


Fig. 3.4. (a) Photograph of a cryoslice through a mouse containing the tumor (arrow) the tumor corresponding to the imaged cross-section. Reconstruction images in the linear (b) and curved (c) mode. The tumor is indicated with a dotted line, and the curved detector allows for better tumor delineation and higher contrast to noise ratio compared to the linear scan which showcases higher background and lower overall resolution. The inserts depict a magnified in-scale view of a central vessel resolved in the tumor, indicated on (b) and (c) by an arrow and demonstrate the resolution improvement in curved scanning. Scalebar 2 mm.

Optoacoustic endoscopy can be based on the translation of a single ultrasound element in linear and curved geometries. This approach can offer miniaturized designs and cost-effective implementations. We analyzed the image performance achieved by a linear and curved scan using phantoms and mice *in vivo*. The curved scanning geometry achieved better image quality than the linear scanning configuration. The resolution characterized by the microsphere phantom was 27% more accurate in the curved mode than the linear scanning mode against the known dimensions of the phantoms imaged. In the paper phantom, the shape structure of the circles and triangle obtained in the curved mode resembles much more the reference image than in the linear scanning mode. In optoacoustic imaging sources generated inside the region of interest radiate spherical waves in all directions. In a curved geometry, where detectors partially surround the region of interest, a larger portion of the acoustic field can be detected thus resulting in the detection of more complementary information and better image quality. This makes the curved geometry particularly interesting for a detailed examination of lesions such as polyps or flat adenomas in colonoscopy.

Conversely, the linear geometry offers a limited viewing angle which reduces the image quality with respect to lateral resolution over the curved geometry. In the linear approach, the lateral resolution is proportional to the detector size  $R_L(h) = \sigma$  [57], whereas in the curved geometry lateral resolution scales by  $R_C(r) = (r/r_0)\sigma$  [57].  $\sigma$  represents the diameter of the detector,  $r$  is the position and  $r_0$  is the radius of the detection arc.

Image quality in both geometries could be further enhanced using a detector with a larger sensing angle. The IVUS detector utilized herein has a quite narrow field of view due to its rather big shape. A transducer with a large aspect ratio (large in elevation and narrow in scanning direction) would satisfy such conditions, or alternatively the combination of a big detection element with a negatively focused lens. The implementation herein employed fixed illumination. This is advantageous from a tomographic reconstruction point of view, but the limitation lies in that a high power laser is necessary to illuminate the whole area of interest. In combination with high repetition rate lasers necessary to impart fast imaging performance, this might be problematic from a laser safety limit point of view. Therefore, future implementations will scan the illumination unit together with the detection unit and use lower energy lasers. The change of the acoustic field due to the modification of illumination conditions can be overcome by using model-based reconstruction algorithms [92]. Overall, the presented concept could be used together with optical endoscopes to yield hybrid optical and optoacoustic imaging performance better than the one achieved by optical imaging alone.

### **3.2 Hybrid OR and AR optoacoustic endoscopy probe**

Optoacoustic endoscopes operating on ultrasonic diffraction limitations using focused ultrasound detectors, achieve lateral resolution spanning from hundreds to tens of micrometers with an imaging depth up to several millimeters. Such acoustic resolution optoacoustic endoscopes have been showcased to provide high resolution visualization of the intestinal vasculature of small animals *in vivo* [52, 54, 81, 82]. Even higher resolution can be achieved by optical-resolution optoacoustic endoscopy using a focused laser beam, in analogy to intra-vital optical microscopy [83-86]. However, as intra-vital microscopy, OR-OE is affected by light scattering in tissue and thus limited to superficial structures. Herein,

we propose an optical resolution (OR) and acoustic resolution (AR) optoacoustic endoscope appropriate for improving the endoscopic depth and resolution range [79].

### 3.2.1 Hybrid endoscopy probe

Fig. 3.5(a) presents the schematic overview of the OR/AR-endoscope. A custom-designed unfocused ultrasound transducer (Imasonic, France) with a center frequency of 20 MHz is used for the detection of ultrasound signals. The diameter of the transducer is 2 mm and the sensing area has a rectangular shape with a length of 0.25 mm and a width of 1.6 mm, yielding an acceptance angle of 80 degrees as derived experimentally from point-source measurements. A GRIN-lens fiber (GT-MMFP-10  $\mu\text{m}$ , GRINTECH, Germany) is secured beneath the transducer for OR illumination. This fiber has a core diameter of 10  $\mu\text{m}$ , a numerical aperture of 0.1, and consists of a gradient index lens, a coreless spacer and a prism. To align the illumination focus, the GRIN-lens is placed with a tilt angle of 5 degrees in relation to the transducer. Such arrangement prevents the fiber tip from blocking the transmission path of optoacoustic signals. Using a beam profiler (SP620U, OPHIR Beam Gauge, US), we measured the beam diameter based on the FWHM value, which at the focus region estimates to be  $\sim 8.7 \mu\text{m}$  [Fig. 3.5(b)]. To implement AR imaging, a multi-mode fiber (400  $\mu\text{m}$  diameter) with a broad side-view illumination has been aligned with the transducer at a tilt angle of 30 degrees. With such an arrangement, the overlapping areas between the laser beam and the acoustic axis begin at about 1 mm distance from the transducer sensing surface, and extend over a large depth. Illumination is provided by a 532 nm laser, with a pulse repetition rate of 2 kHz and energy of 1 mJ/pulse and pulse width of 0.9 ns (Wedge HB532, BrightSolutions SRL, Pavia, Italy). The beam is attenuated, collimated and guided through a pinhole (10  $\mu\text{m}$  in diameter, Thorlabs) to ensure spatial filtering. It is then passed into a telescopic lens array (Thorlabs) to adjust the beam diameter to match the back aperture of a low NA microscope objective (L-4X, Newport), which is mounted on a manual fiber coupler (F-91TS, Newport). Finally, the beam is tightly focused and coupled into the OR and AR fibers respectively. The light fluence at the surface of the sample is measured to be about 10 mJ/cm<sup>2</sup> for OR imaging and about 6 mJ/cm<sup>2</sup> for AR imaging. The recorded optoacoustic signals without averaging are amplified by a low noise amplifier (63 dB, AU-1291, Miteq

Inc., Hauppauge, New York, USA) and sampled by a high-speed digitizer, operating at 1 GS/s (NI PCI-5124, USA; 12 bit resolution; max sampling rate 4 GS/s).

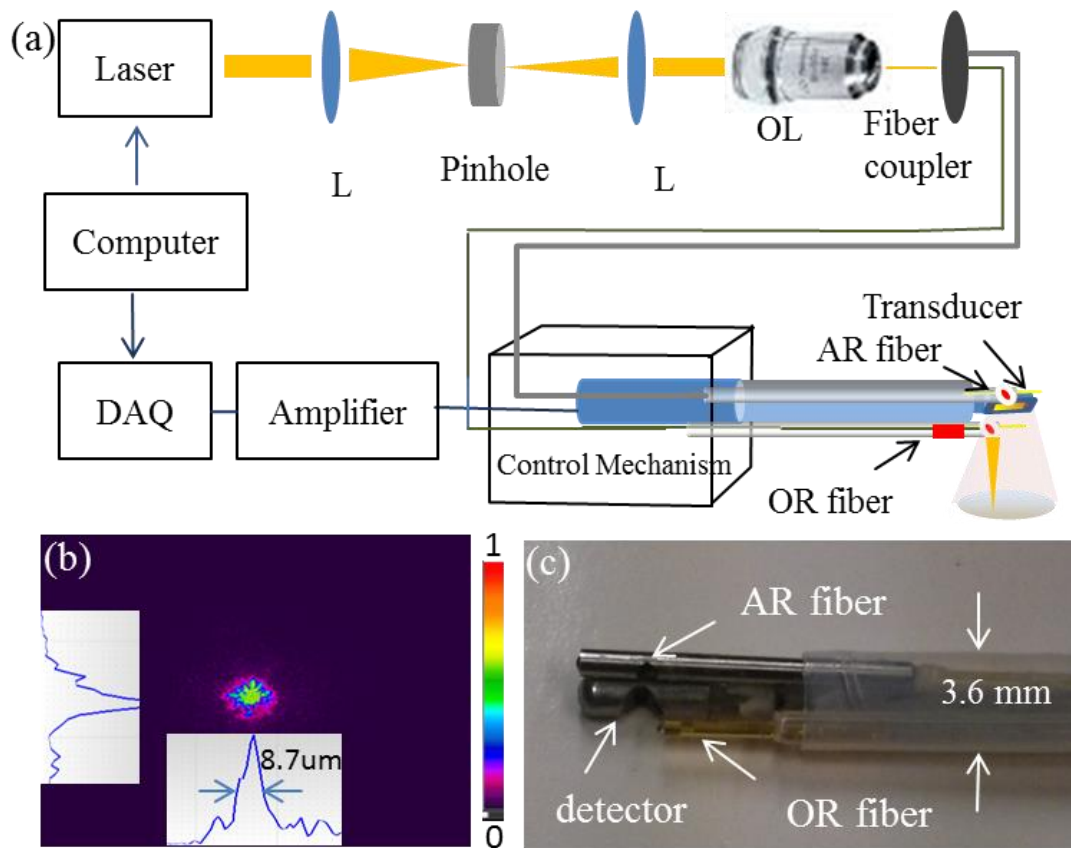


Fig. 3.5. (a) Schematic illustration of the imaging setup with alignment of various modules; Abbreviations: L, Lens; OL, objective lens. (b) Laser beam intensity profile at the focal distance. (c) Photograph of the distal end of the hybrid endoscopy probe.

The endoscope probe is encapsulated in a medical-grade (polyethylene terephthalate) tube with an outer diameter of 3.6 mm, which can readily pass through 3.8 mm working channels of commercial video endoscopes. Fig. 3.5(c) shows the enlarged photograph of the probe. To obtain volumetric images, fast linear and rotational stages (Oriental Motor, Japan) are employed. The probe is scanned linearly along the direction of the lumen and rotated to get adjacent cross-sectional images. This scanning mode is suitable only for limited-view imaging of the lumen volume, *i.e.* an imaging mode that is appropriate for operation under optical endoscope guidance, whereby the hybrid optoacoustic endoscope is operated through the working channel of an optical endoscope. However, 360 degrees rotation could also be

contemplated for endoscopes designed to operate in stand-alone mode, *i.e.* without white-light endoscopy guidance. In the current implementation, OR and AR scans are performed by sequentially coupling the light into the corresponding fiber. The linear and rotational scanning step sizes are 0.01 mm and 0.01 degrees for OR imaging, and 0.08 mm and 0.1 degrees for the AR imaging. Hilbert transform is performed to process the OR data; the filtered back-projection method is used to reconstruct the AR data as described previously [91].

### 3.2.2 Characterization measurements

To characterize the resolution of the system, we measured a phantom with several sutures (10  $\mu\text{m}$  diameter) embedded in scattering agar (6% intra-lipid) at different depths (0.3 mm to 4 mm). The suture positions are illustrated in Fig. 3.6(a). In order to quantify the OR resolution, point-spread-functions (PSFs) were measured by imaging the first suture at different distances from the OR fiber. Fig. 3.6(b) and (c) present the OR images with results of these measurements. Evidently, the width of PSF shows a clear depth-dependency following the diameter variation of the laser beam, and the corresponding beam diameter characterized as FWHM along the depth direction is depicted in Fig. 3.6(c). The highest signal intensity corresponds to the focal distance of the optical illumination (*i.e.*, 0.8 mm from the probe surface), as indicated by the white arrow in Fig. 3.6(b). From this specific position, the lateral resolution is estimated to be 13  $\mu\text{m}$ , as illustrated in the inset of Fig. 3.6(c). To determine the combined OR and AR resolution, a B-scan image of the phantom was obtained and shown in Fig. 3.6(d). The detector was kept at 0.5 mm distance from the phantom surface. OR readouts are presented in green while AR measurements are marked in red. Obviously, the OR mode can only resolve the first suture because of optical scattering. The AR mode on the other hand can image much deeper, obtaining a lateral resolution of  $\sim 250$   $\mu\text{m}$  at depths of at 1.5 mm. Fig. 3.6(e) presents the AR resolution as a function of the imaging depth. To demonstrate the volumetric imaging ability of the hybrid endoscope, a four suture phantom was imaged as illustrated in the Fig. 3.6(f, inset). The phantom was built by fixing sutures (10  $\mu\text{m}$  in diameter) at two different layers of  $\sim 1$  mm separation. Subsequently, the sutures were arranged in a luminal structure, and scanned cylindrically over 10 degrees. Fig. 3.6(f) depicts the corresponding 3D image, showing the overlay of the OR and AR optoacoustic scans.

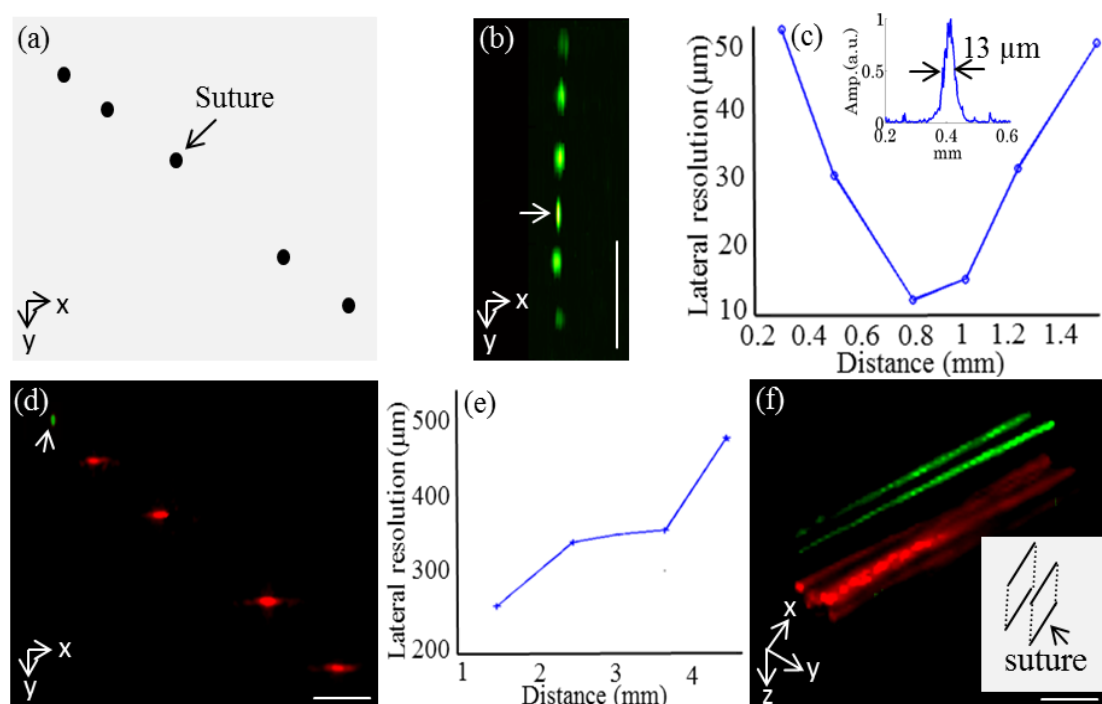


Fig. 3.6. (a) A schematic illustration of the suture phantom. (b) Optoacoustic images of a 10  $\mu\text{m}$  suture imaged with OR illumination at different depths, scale bar 500  $\mu\text{m}$ . (c) Graphical representation of the OR beam diameter characterized as FWHM along with the depth direction. The inset shows a lateral line profile of the suture (indicated by the white arrow in (b)) in the focus region of the GRIN fiber. (d) Optoacoustic images of sutures acquired at different depths with OR and AR illumination, the +y axis corresponds to depth direction, scale bar 1 mm. (e) Lateral AR resolution graph along the depth direction. (f) The corresponding 3D image, showing the overlay of normalized OR and AR optoacoustic images of the suture phantom; the +z axis corresponds to depth direction; scale bar 1 mm. The OR images are presented in green while the AR image are in red.

In order to assess the imaging performance of the system on biological specimens, a fresh mouse ear was imaged *ex vivo*. A luminal structure was casted by rolling the mouse ear inside a plastic tube. A photograph of the ear imaged prior to rolling is shown in Fig. 3.7(a). Volumetric images were obtained by scanning the probe cylindrically over 20 degrees and linearly along the lumen longitudinal dimension over 3 mm, with the distance between the mouse ear and the probe kept about 1 mm during scanning. By linearly pulling the probe, we acquired sectional images [indicated by the dash line in Fig. 3.7(b)] in the AR and OR mode respectively, which are displayed in Fig. 3.7(d) and (e). The maximal amplitude projections of the volumetric images acquired in AR and OR modes are shown in Fig. 3.7(b) and (c)

respectively. As can be seen, the AR image resolved the large vessels, which accurately matched those visible in the photograph. Of note, numerous smaller vessels are distinguishable on the OR image, which are not visible on the AR readouts [e.g. indicated by the white arrow in Fig. 3.7(c)].

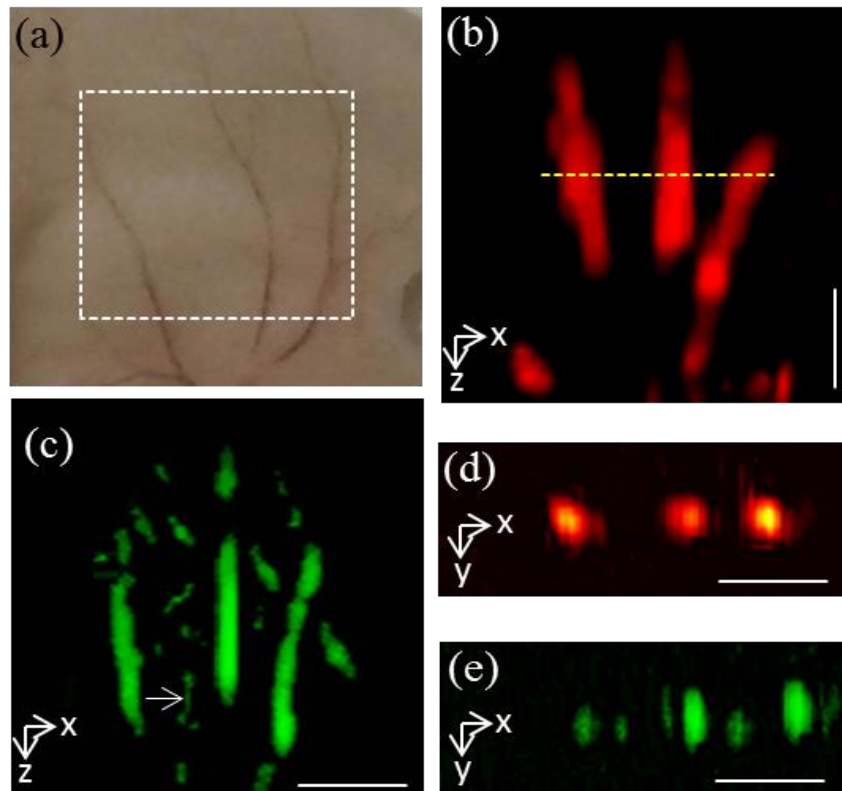


Fig. 3.7. Optoacoustic images of a mouse ear *ex vivo*. (a) The photograph of the mouse ear shows the scanning area (highlighted by a dash square). (b) and (c) Volumetric maximal amplitude projection images acquired in AR and OR mode respectively, from the mouse ear boxed by the dash square in (a). (d) and (e) Corresponding AR and OR sectional images in the position marked by the yellow dash line in (b). Red and green colors represent the AR and OR images, respectively. Scalebar 500  $\mu\text{m}$ .

The data presented herein demonstrate the feasibility of hybrid optical resolution and acoustic resolution optoacoustic endoscopy with a single sensor for the first time to our knowledge. The diameter of the probe is 3.6 mm, compatible with the working channel of white-light optical endoscopes. As shown, by focusing the laser light with the GRIN fiber, an optical resolution of the order of 13  $\mu\text{m}$  can be achieved, with an impressive SNR of 20 dB (determined based on the ratio of the peak signal intensity and average noise) based on the characterization of a 10  $\mu\text{m}$  diameter suture with the laser energy below the ANSI safety limit

(20 mJ/cm<sup>2</sup>). The results of the *ex vivo* measurements of the mouse ear and phantoms show that the proposed hybrid endoscopy system can gain optical resolution imaging of the surface and tomography imaging for the deeper features. It should be noted that, due to the short working distance of the OR fiber, the probe in the current implementation must be close to the sample surface, thus only a limited luminal segment can be imaged at a time. To improve the applicability of the presented endoscope to obtain circumferential images of the big lumen, a GRIN fiber with longer focal distance should be applied. Besides, advanced ultrasound transducers, such as optical interferometry based ultrasound detectors, could increase both the sensitivity and AR resolution [93]. Furthermore, beam-splitting or preferably two time-interleaved laser sources could be employed for concurrent imaging, which can further improve imaging efficiency. The presented concept of using two different fibers to achieve dual OR and AR imaging can improve endoscopic applications, yielding additional information inaccessible to previous implementations.

### **3.3 Linear array-based endoscopy probe**

Single detector based endoscopy normally needs a complex control system to scan the endoscopy probe. For example, the gastrointestinal tract of a rat was imaged *ex vivo* using a 4.2 mm diameter photoacoustic imaging probe composed of an integrated light guiding optical fiber, an ultrasonic detector and a mechanical rotating acoustic and optical reflector for sectorial B-scan imaging [53]. This system was further miniaturized to 3.8 mm equipped with a spherical focused ultrasound transducer to enable simultaneous optoacoustic and ultrasonic endoscopy of the esophagus, the colon and the lymphovascular system near the colon, of a rat *in vivo* [52, 55]. Recent implementations of the system feature an additional size reduction to 2.5 mm to fit through the working channel of a standard colonoscope for endoscopic guidance [55]. However, due to the limitation of laser repetition rate, the imaging speed is restricted. Then motion issues during scanning hinder the ability of real time sectional imaging or volumetric imaging for *in vivo* measurements. Herein, we present a novel endoscopy concept for intracavitary applications in humans. In contrast to single transducer implementations, transducer arrays can be employed in rotation or translation mode and can offer real-time 2D image formation based on parallelized tomographic

detection in analogy to a previously reported real-time MSOT handheld device [94]. By using a multitude of transducers operating in parallel, arrays can accelerate detection by minimizing scanning times.

### 3.3.1 Transducer array based endoscopy probe

A schematic representation of the probe is depicted in Fig. 3.8(a). Key components of the system are a miniaturized linear multi-element transducer array and an illumination unit arranged in a way so that signals are generated confocal to the ultrasound detection plane. In this way, a single light pulse can be used to form a 2D image. A picture of the experimental setup is shown in Fig. 3.8(b). The key component is a 64 element, linear transducer array catheter with a diameter of 3 mm and insertion length of 1.2 m (Vermon, France). The detector is manufactured using piezocomposite technology with a central frequency of approximately 7 MHz and a nominal transmit-receive bandwidth of 60%. The elements have a rectangular shape and are arranged in a row with a pitch of 205  $\mu\text{m}$ . Their height is 2 mm. A real picture of the array is shown in Fig. 3.8(d). The schematic map of the endoscopy system is illustrated in Fig. 3.8(c). As for the light source, we use an optical parametric oscillator (OPO) with a tuning range in the near-infrared (680 nm - 980 nm) and pumped with a frequency doubled diode-pumped Nd:YAG laser (Phocus, Oportek). The laser pulse duration is below 10 ns whereas the pulse repetition frequency is 10 Hz. Light is coupled into a custom silica fused-end fiber bundle consisting of a linear output and oriented to create a stationary illumination zone of  $\sim 3\text{mm}$  height on the surface of the sample, coinciding with the ultrasound detection plane. The incident light energy was kept below the laser safety standards of 20  $\text{mJ}/\text{cm}^2$  at wavelength of 740 nm.

A custom-built acquisition system with 64 channels, a sampling rate of 40 megasamples per second, 12 bit digital resolution, amplification of 32 dB and triggered by the laser's Q-switch was used to record the time-resolved optoacoustic signals. A motorized translation stage (Thorlab) was used to scan the array along its longitudinal axis. To investigate the image quality for different detection apertures, the array was scanned over a 4 cm range with a step size of 205  $\mu\text{m}$ . Two samples were imaged: To characterize the imaging performance of the system under defined conditions a 2D phantom was built by printing a complex pattern on a

sheet of paper using a laser printer (FS-C5400DN). A photograph of the complex pattern is shown in Fig. 3.9(a). The paper was embedded into a turbid agar cylinder made of 2% w/v agar (Sigma, Germany) and 6% v/v intralipid (Sigma-Aldrich, Germany). The second sample was a freshly sacrificed nude CD1 mouse with a 4T1 tumor on its back. The goal of this experiment was to see whether it was possible to identify the infiltration depth of the tumor in the image. Both samples were immersed in water used as coupling medium to propagate the acoustic waves from the sample to the detector.

Before reconstruction, the measured signals were corrected for the electrical impulse response of the system and bandpass filtered between 800 kHz and 8 MHz. The image reconstruction was done with the 2D IMMI method on a 301x301 grid with a pixel size of 77  $\mu\text{m}$  [65, 71]. In addition we applied top-hat filtering with a disc shaped kernel of 8 pixels for background subtraction.

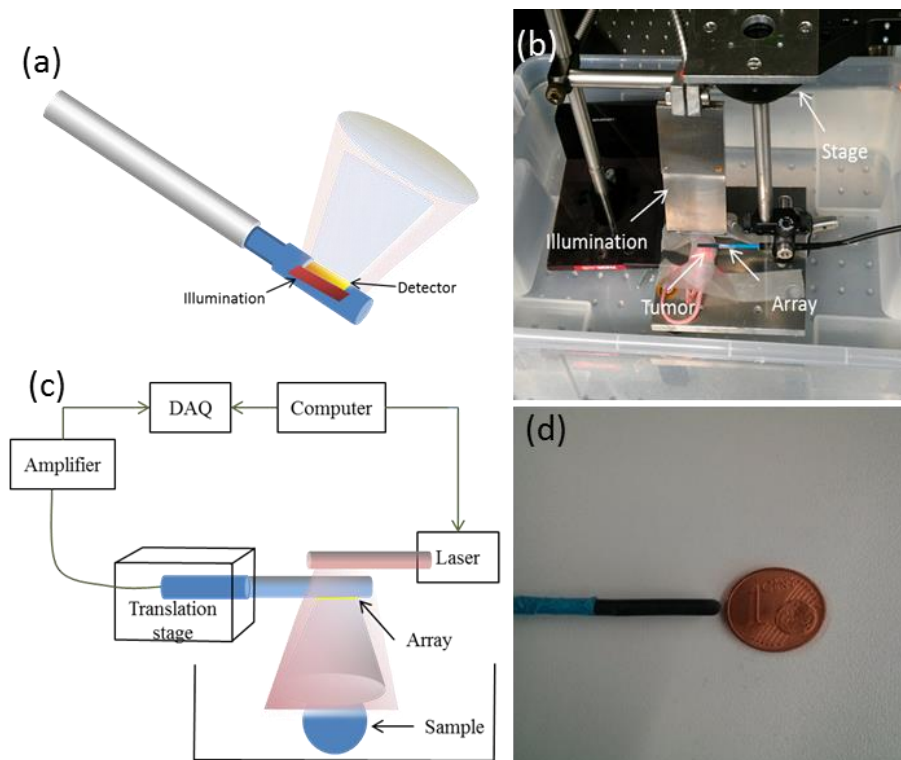


Fig. 3.8. (a) Schematic representation of the optoacoustic endoscopy probe. (b) Photograph of the experimental setup. (c) Schematic of the system. (d) Picture of the array.

### 3.3.2 Characterization measurements

Fig. 3.9(b) – (f) show the reconstruction of the phantom for different scanning distances by linearly scanning the array apertures. Fig. 3.9(g) depicts the correlation coefficient between the reconstruction result and the reconstruction with the longest aperture for different lengths of the detection aperture. The profiles through the reconstruction along the two lines indicated in Fig. 3.9(b) are shown in Fig. 3.9(h) and (i), respectively. The ability to discern the two points along line 2, which are separated by  $460\ \mu\text{m}$ , shows that the lateral resolution is better than  $460\ \mu\text{m}$ . Perpendicular to it, all structures can be distinguished, even the one which are only  $140\ \mu\text{m}$  apart. Thus the resolution along the acoustic axis of the array is around  $140\ \mu\text{m}$ . For shorter detection apertures, we perceive reduced reconstruction accuracy manifested by an increased blurring of structures along the scanning direction. The blurring increases significantly for apertures shorter than  $1.5\ \text{cm}$ . Perpendicular to it, which is along the acoustic axis of the transducer; the resolution loss due to the shorter detection aperture is less.

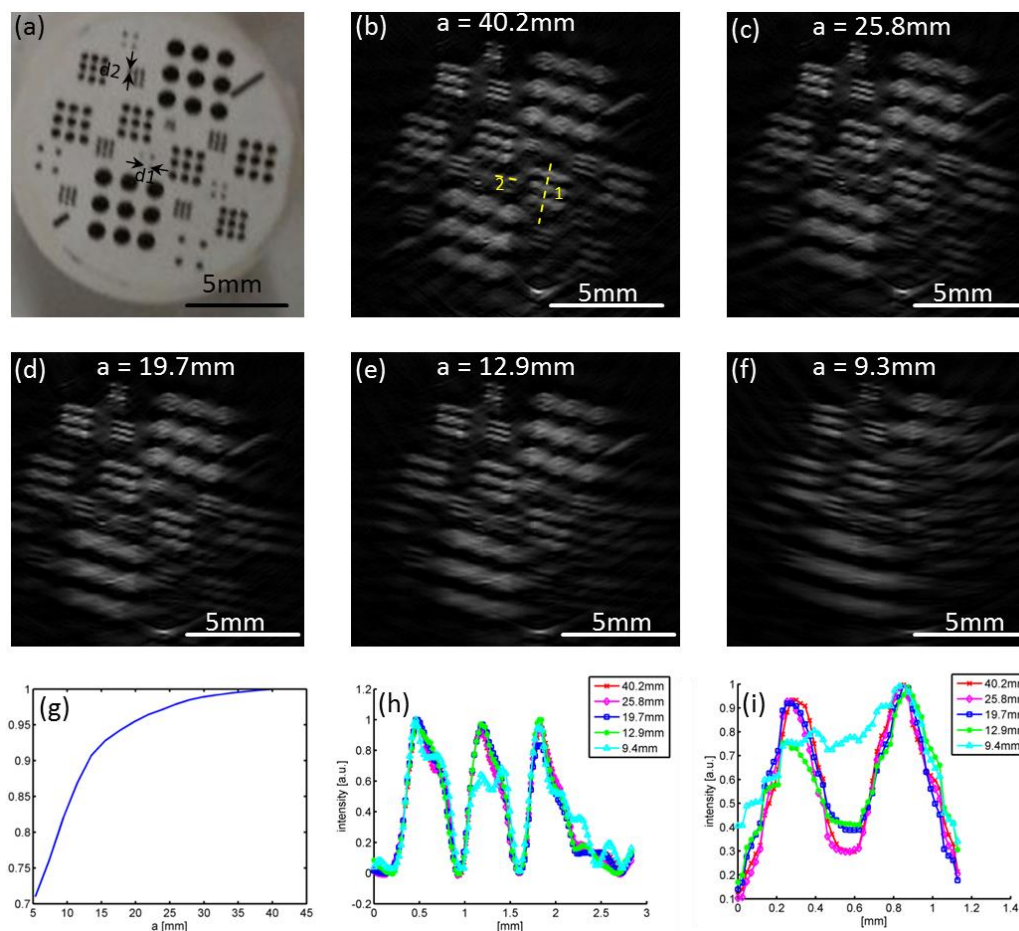


Fig. 3.9. (a) Photography of the phantom. (b) – (f) Reconstructions with different lengths of the detection aperture. The distance between individual transducer elements is  $205\mu\text{m}$ . (g) Cross-correlation coefficient between reconstruction and reconstruction with the longest detection aperture for different detection apertures. (h) Profile along line 1 shown in (b). (i) Profile along line 2 shown in (b). Distance  $d_1=460\mu\text{m}$ . distance  $d_2=140\mu\text{m}$

Fig. 3.10 shows the reconstruction results of the tumor experiment. Panel Fig. 3.10(a) shows a photograph of a cryosliced mouse with a 4T1 tumor on its back for comparison. Panels Fig. 3.10(b)-(f) display the reconstruction results as a function of the aperture length. The tumor and surrounding tissue structures can be recognized clearly. The penetration depth is about 1 cm below skin surface. Only small differences are visible in the reconstructions for apertures between 2 cm and 4 cm. On the other hand, below 2 cm the reconstruction accuracy decreases significantly, especially in the deeper tissue structures.

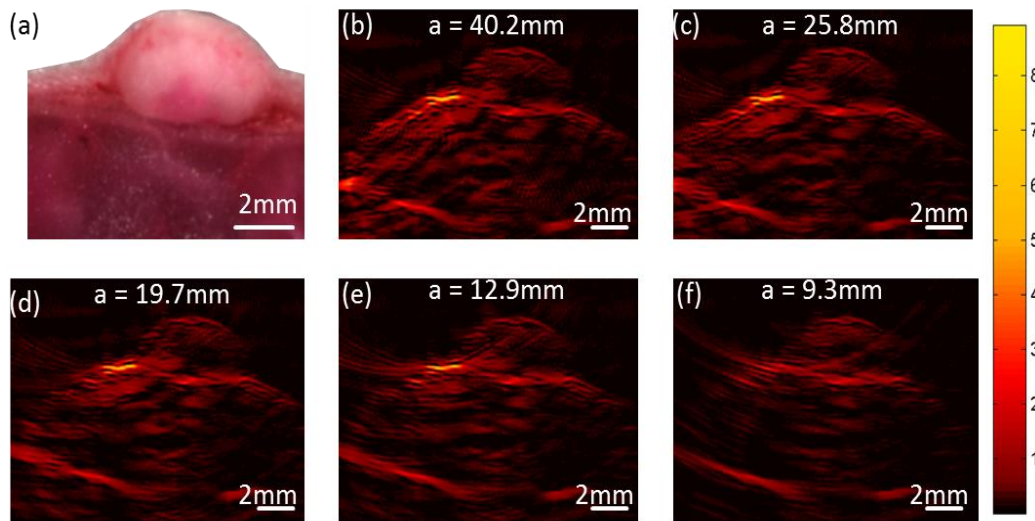


Fig. 3.10. (a) Photograph of a cryosliced through a HT1 tumor implanted on the back of a nude CD1 mouse. (b) – (f) Reconstruction result for different detection apertures.

In summary, we implemented a novel concept for endoscopic multispectral optoacoustic tomography. We have analyzed the influence of the length of the detection apertures on the reconstruction result and have seen that we can delineate tumor boundaries and resolve structures even 1 cm deep inside tissue. Accuracy of the reconstruction depends hereby on the detection aperture of the array utilized. Significant improvement could be achieved by increasing the detection aperture to about 2 cm. For longer detection apertures, additional improvement is marginal. The reason for this behavior is the directivity of the elements due to their finite width. This prevents them from covering a larger area. More elements and a longer detection aperture would therefore increase the field of view of the whole system, but would not provide additional complementary information to improve the reconstruction. To increase their field of view, the width of the elements should be reduced; however at the cost of the SNR.

Producing small arrays is a requirement for this implementation. In this experiment we used an array with 3 mm out diameter and a detection aperture of 12 mm and 64 elements.

Increasing the detection aperture to 2 cm or beyond is therefore realistic. The next step is to combine detection and illumination unit in one encapsulated device. Overall the presented results have proven the great potential of endoscopic multispectral optoacoustic tomography

to be applied to clinical diagnosis, for instance in early stage tumor detection, determination of infiltration depth, distinction between benign, malignant and premalignant lesions.

### **3.4 Summary and Discussion**

In this chapter, three optoacoustic endoscopy probes were built based on different scanning geometries, illumination settings and ultrasound transducers. These implementations tried to analyze the influence of different configurations on the imaging performance of optoacoustic endoscopy. For example, we interrogated the merits of optoacoustic endoscopy implemented by translating a sound detector in linear or curved geometries. The linear and curved detection geometries were achieved by scanning an intravascular ultrasound transducer within a plastic guide shaped to line or a curve. This concept could be used together with optical endoscopes to yield hybrid optical and optoacoustic imaging. Comparing to the radical scanning geometry, the curved scanning geometry achieved better image quality as demonstrated by phantom and biological measurements.

Besides, we proposed the implementation of hybrid optical and acoustic resolution optoacoustic endoscopy. Laser light was transmitted to tissue by two types of illumination achieving optical and acoustic resolution imaging. The imaging performance of the hybrid endoscope was validated on phantoms and biological samples, which show that the proposed hybrid endoscopy system can gain optical resolution imaging of the surface and tomography imaging resolution for the deeper features for the first time. The presented concept of using two different fibers to achieve dual OR and AR imaging can improve endoscopic applications, yielding additional information inaccessible to previous implementations.

Furthermore, a miniaturized linear transducer was used for optoacoustic endoscopy implementation, which could allow the endoscopic deployment of MSOT. By using a multitude of transducers operating in parallel, arrays can accelerate detection by minimizing scanning times. The presented results have proven the great potential of real-time endoscopic multispectral optoacoustic tomography compared to single element scanning based endoscopy probes.

Overall, the three endoscopy probes have shown the influence of scanning geometries, illumination settings and transducers on the development and performance of optoacoustic endoscopy. The gained knowledge is helpful to optimize the development of optoacoustic endoscopy probes for esophagus imaging. However, all probes introduced in this chapter are designed for small animal imaging and not optimal for human or large animal esophagus imaging. For example, the curved endoscopy probe has fixed illumination, impairing the capability of volumetric imaging. The limited focal length of the GRIN fiber inside the hybrid endoscopy probe limits its imaging distance to 1 mm, preventing imaging large esophageal lumens with diameters up to several centimeters. The array based endoscopy probe can only acquire cross-sectional images in a very limited field of view. Therefore, new implementations of optoacoustic endoscopy systems should be developed for esophagus imaging.

## **Chapter 4    Optoacoustic endoscopy system development**

The influence of scanning geometries, illumination and transducers has been investigated to optimize the development of optoacoustic endoscopy probes. In order to apply optoacoustic for endoscopy applications, the endoscopy imaging system, including the illumination source, the acquisition component, and the mechanical movement unit, have been developed and integrated with the optoacoustic endoscopy probes, enabling optoacoustic imaging inside the gastrointestinal organs. Existing optoacoustic endoscopy systems are mainly designed for small animals (like rats and rabbits), which are not suitable for imaging gastrointestinal organs of human or large animals. In this chapter, two optoacoustic endoscopy systems are developed for esophagus imaging, and the performance are validated on phantoms. Section 4.1 first introduces the scanning control system, which enables volumetric scanning of endoscopy probes introduced. The IVUS based endoscopy system is then described in section 4.2. Afterwards, the capsule endoscopy system is presented in section 4.3. At last section, we summarize this chapter and discuss the challenges and necessary improvements of endoscopy systems for in vivo esophagus imaging.

### **4.1    The scanning control system**

A schematic of the endoscopy system is shown in Fig. 4.1. This system includes four main parts. First, for the illumination source, we utilized a 532 nm laser wavelength with a pulse repetition rate of 2 kHz, energies of 1 mJ/pulse, and pulse widths of 0.9 ns (Wedge HB532, BrightSolutions SRL, Pavia, Italy). The laser beam was focused and coupled into the fiber. A custom-designed hybrid rotary joint (Princetel, Inc, US) was made, which enabled continuously rotation of optical and electrical paths. The joint had the ability of free coupling for fibers with different diameters. Beside the optical channel, it has four electrical channels.

Several supporting components of the system were made by 3D printer. As shown in Fig. 4.1, the rotary joint was combined with the rotation and translation stages (Oriental Motor, Japan), and the endoscopy probe was stabilized by the probe holder, mounted on the rotation stages. In this system, an electrical amplifier (63 dB, AU-1291, Miteq Inc., Hauppauge, New York, USA) was connected between the rotary joint and the ultrasound detector. This configuration can help to improve the SNR. The reason is that the rotary joint may introduce artifacts to the signal transition path during rotation process. If the amplifier is connected after the rotary joint, the SNR decreases as artifacts induced by the rotary joint are amplified. Once optoacoustic signals passed through the rotary joint, a high-speed digitizer, operating at 2 GS/s (CS122G1, Gage, Lockport, Illinois, USA; 12 bit resolution; max sampling rate, 2 GS/s) was used to record the ultrasound waves. This control system allows moving endoscopy probes in radial or linear scanning geometries.

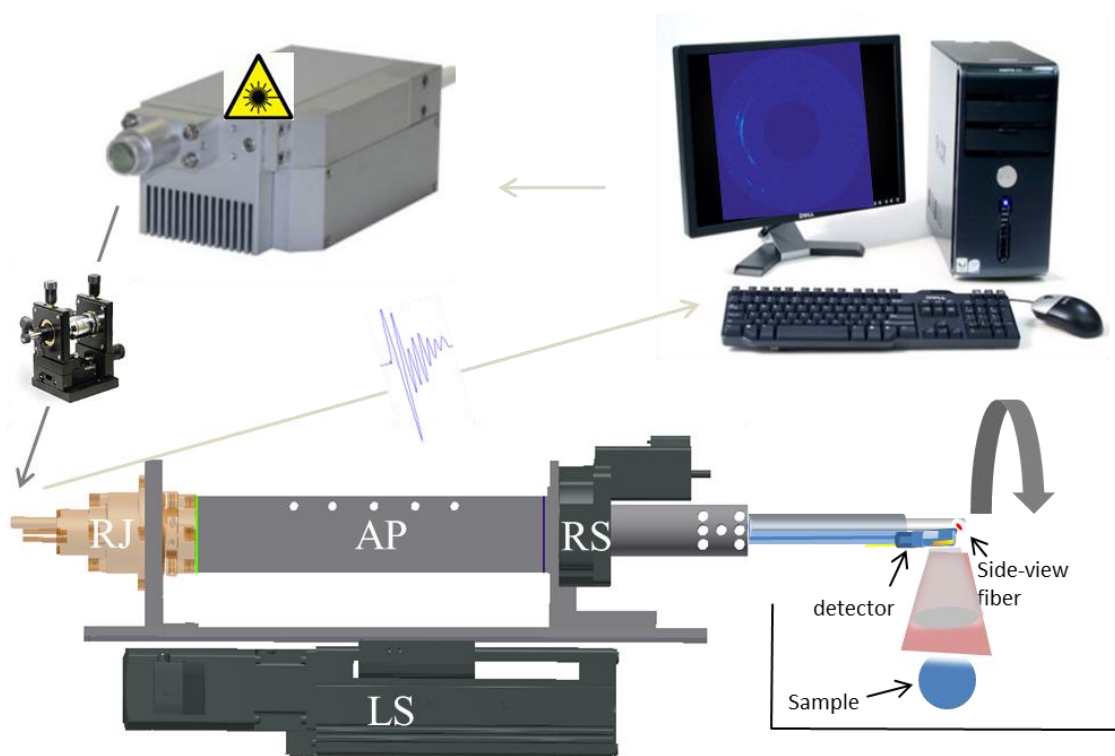


Fig. 4.1. Schematic of the endoscopy system, including the scanning control unit and endoscopy probe. Aberrations: LS, translation stages; RS, rotation stage; AP, Amplifier; RJ, rotary joint.

## 4.2 IVUS-based endoscopy system

Optoacoustic endoscopy has been so far implemented using dedicated endoscopes operating using rotational and translational scanning of ultrasound sensors [50, 53, 55].

Implementations of this concept have been presented using single-element unfocused [53] and focused [55] detectors. The detector incrementally revolves around its axis while B-scan images are captured. This radial mode arrangement can be easily controlled to get cross-sectional images of a lumen. However, it is difficult to get a full-view image of a big lumen, because the working distance of the probe is limited by the overlap region between the detection view and illumination [55, 88]. The uncovered area would increase when the probe is not positioned at the center of the lumen. In addition, motion artifacts limit the volumetric imaging performance of measurements *in vivo* [95]. We have implemented an endoscopy probe by aligning a single element detector with a side-view fiber. The endoscopy probe is fully encapsulated inside a plastic tube connected with a cylindrical housing made of stainless steel. The housing is cut with an open window and then covered with plastic membrane. With such implementation, the endoscopy probe can be centered and stabilized inside the housing during volumetric scanning. Phantom and *ex vivo* pig esophagus samples are measured to test its performance and practicability.

### 4.2.1 System implementation

A picture of the endoscopy system and a photograph of the distal end of the proposed optoacoustic endoscopy probe are shown in Fig. 4.2. A commercial IVUS sensor (2.5-Fr, Atlantis SR Pro, Boston Scientific, Natick, MA) with a center frequency of 15 MHz was used for signal detection. The active element had a disc-like shape with a diameter of 0.8 mm yielding an acceptance angle of 30 degrees as derived experimentally from point-source measurements. In order to optimize the signal detection sensitivity over a larger depth range, a side-view fiber (600  $\mu\text{m}$  in core diameter) was aligned to the transducer with a tilt angle of about 15 degrees, and the overlapped areas between the laser beam and the acoustic axis [indicated by the dash lines in Fig. 4.2(b)] started about 2 mm distance from the transducer sensing surface and extended over a large depth. An example of the beam shape emitting the optical fiber is presented in Fig. 4.2(b), resulting in a broad illumination pattern. The signal

wire of the transducer and the fiber has been immersed in a custom-designed torque coil (3.2 mm in diameter), which can accurately transfer the rotation force from the proximal rotation stage. The probe was fully encapsulated in a plastic tube (3.6 mm in diameter). In order to stabilize the probe during scanning, a cylindrical housing was connected to the end of the plastic tube. The metal housing was made of a stainless steel tube (wall thickness of 0.5 mm, and 6 mm in outer diameter) with a 320 degree open cut. PET membrane (25  $\mu\text{m}$  wall thickness) was fully covered the lumen to form 320 degrees detection window for optical and acoustic transmission. The whole length of the metal housing was 25 mm and the length of the membrane window was 20 mm.

The IVUS detector was scanned along the center axis of the metal housing and can acquire 20 mm long volumetric images without moving the plastic tube. This configuration can make the endoscopy probe centered inside the lumen and keep constant distance to the image object. The control system mentioned in section 4.1 was used for volumetric scanning. Larger imaging field of view can be achieved by either extending the length of the metal housing or moving the plastic tube. The recorded signals were firstly bandpass filtered between 1-20 MHz and the image reconstruction was performed using Hilbert transform subsequently.

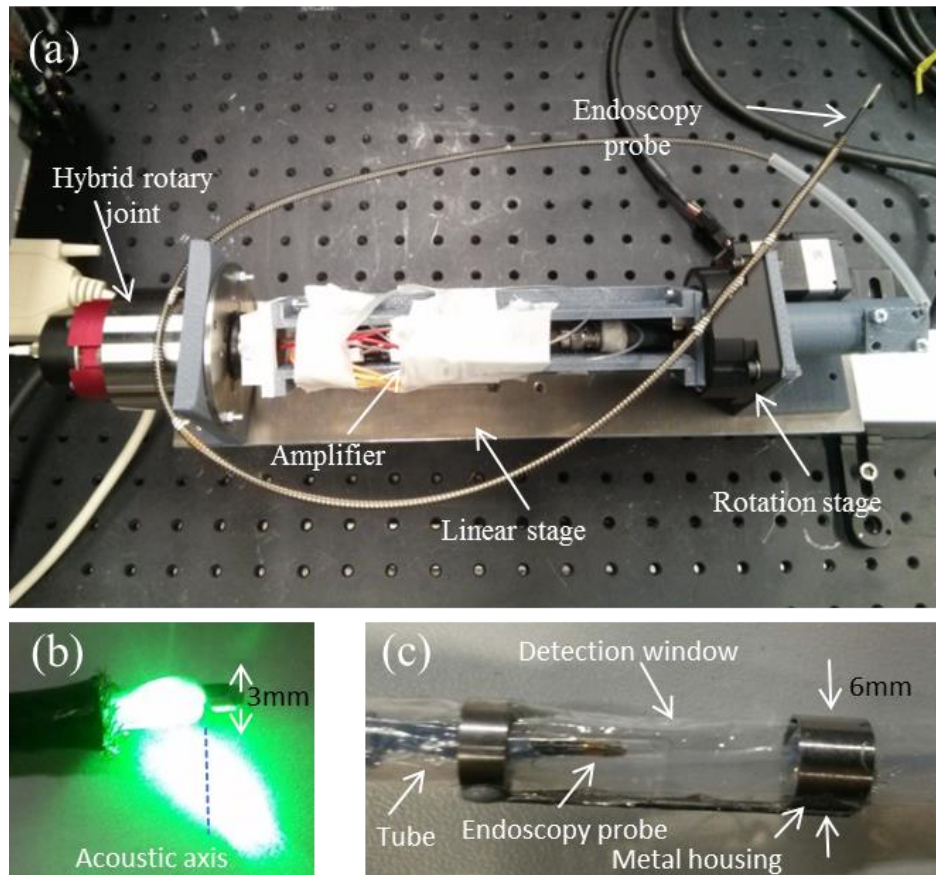


Fig. 4.2. (a) Picture of the imaging setup. (b) illumination pattern. (c) Photograph of the distal end of the endoscopy probe, including the metal housing head.

#### 4.2.2 System characterization

To characterize the imaging performance of the system, we imaged two phantoms as shown in Fig. 4.3. The first phantom included four sutures (100  $\mu\text{m}$  in diameter) which were fixed in several layers using semi-transparent tapes, and rolled into the shape of a cylinder. Sutures were arranged at different distances to the center of the tube and one full view B-scan image is shown in Fig. 4.3(a). The radial and transverse resolutions were quantified using this phantom by analyzing the FWHM values. And the resolution dependencies on the target distance from the surface of the probe are plotted in Figs. 4.3(c) and (d), respectively. As presented in Fig. 4.3(c), the transverse resolution depicts strong target distance dependence. For example, it shows a minimum value of 650  $\mu\text{m}$  at 2.2 mm distance from the transducer surface, and gradually increases with the target distance. The radial resolution appears much

less variations around  $180\ \mu\text{m}$ . To test the volumetric imaging capability of the system, another phantom with cylinder shape made of black tape was imaged. The cylinder covered the metal housing area without any extra support, forming a 300 degrees cylindrical contour. Fig. 4.3(b) shows the reconstructed 3D image, where the tape surface is clearly recovered with uniform image quality.

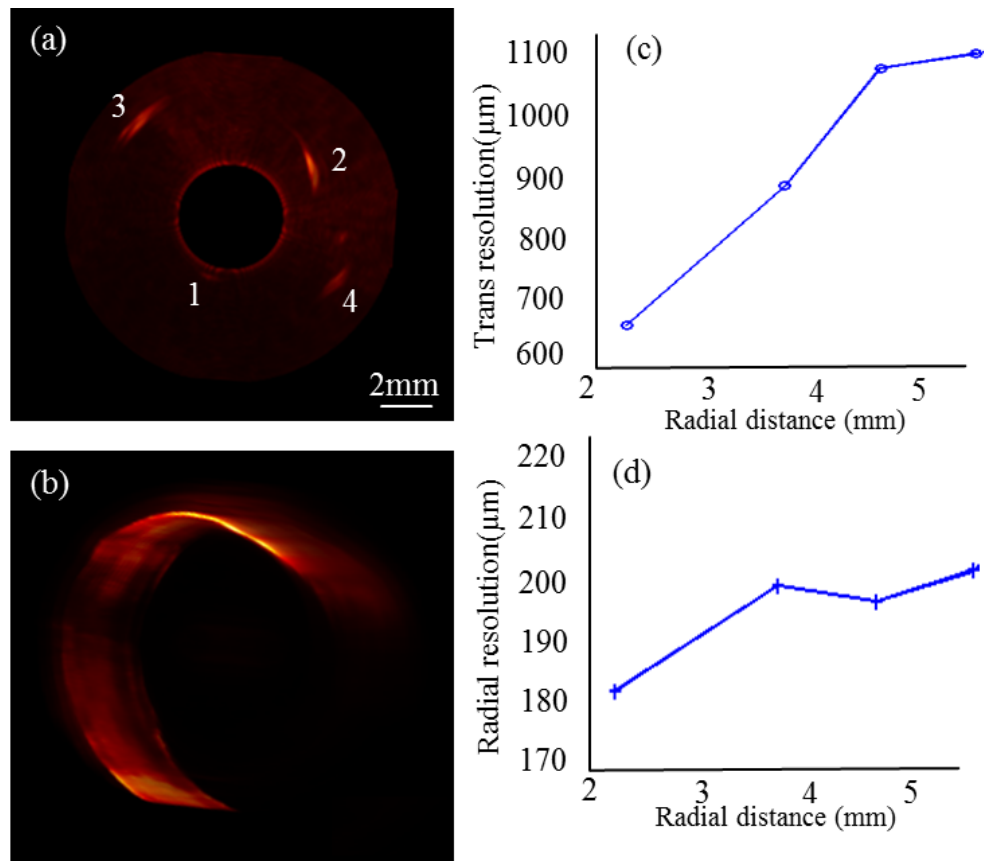


Fig. 4.3. (a) One B-scan optoacoustic image of the suture phantom, suture positions are labeled from 1 to 4 along the radial direction. (b) Volumetric optoacoustic image of the black tape phantom. (c) and (d) transverse resolution and axial resolution along the depth direction.

### 4.3 Focused detector based endoscopy system

IVUS based endoscopy probes have been introduced in section 4.2 and will be further discussed in chapter 5. Even though IVUS based endoscopy is easy to implement with a simple structure, poor lateral resolution determined by the size of the IVUS sensor limits its

wide use. Therefore, transducers with ultrasound focusing ability can be used to improve the image resolution.

### **4.3.1 System implementation**

As mentioned in Chapter 2, a spherical focused detector [made of polyvinylidene difluoride (PVDF) Precision acoustic, UK] with focal length of 7 mm is used for endoscopy implementation. The diameter of the sensing area as shown in Fig. 4.4(a) is about 3 mm. The simulated sensitivity fields of this transducer are shown in Fig. 4.4(b). From the simulation result, we can see the length of the focal zone is about 2 mm, where high quality images can be obtained. Outside of the focal zone, the resolution decreases rapidly. A multimode fiber with diameter of 600  $\mu\text{m}$  was aligned side of the transducer for illumination. A 10  $\mu\text{m}$  suture was imaged by this detector along the depth direction and the corresponding image is displayed in Fig. 4.4(c). The result showed high resolution images of sutures were acquired in the focus, while sutures located outside of the focus got elongated. The starting and ending points of the focal zone are located where the on-axis pulse-echo signal amplitude drops to -6dB of the amplitude of the focal point, which is illustrated by the white rectangle. Therefore, the image object should be positioned inside the focus of the transducer to obtain high quality images. The control system described in section 4.1 is applied for helical volumetric scanning.

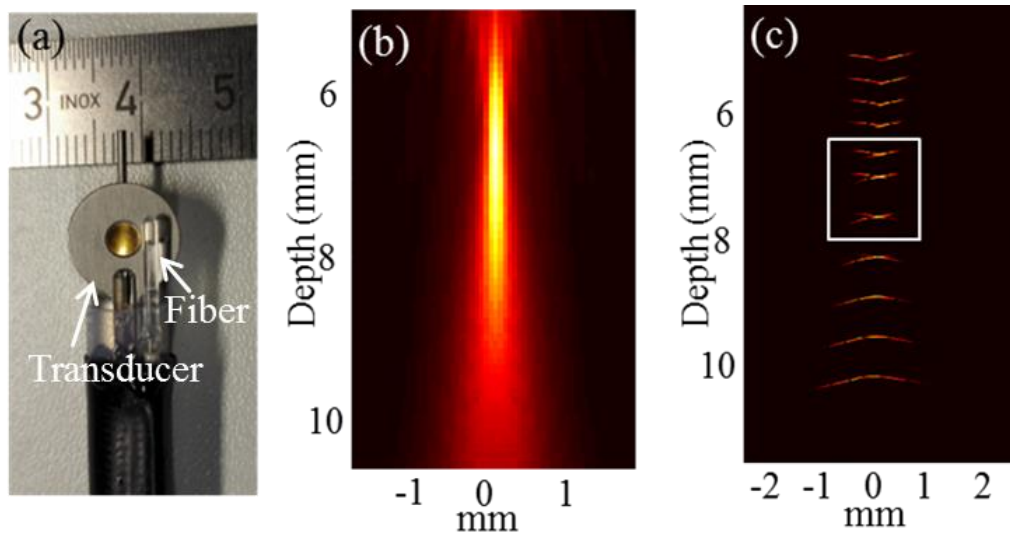


Fig. 4.4. (a) The endoscopy probe. (b) Simulated sensitivity fields of the PVDF detector. (c) Optoacoustic image of the suture phantom.

### 4.3.2 System characterization

The detection bandwidth is characterized based on the 10  $\mu\text{m}$  suture phantom and the corresponding raw signal of the suture located in the focus is shown in Fig. 4.5(a). The detection bandwidth is calculated and displayed in Fig. 4.5(b). It can be noted that the -6 dB frequency bandwidth is from 7- 49 MHz and the center frequency is about 28 MHz. Based on the FWHM values, the lateral and axial resolution is characterized as 67 $\mu\text{m}$  and 51  $\mu\text{m}$  as shown in Fig. 4.5(c) and (d).

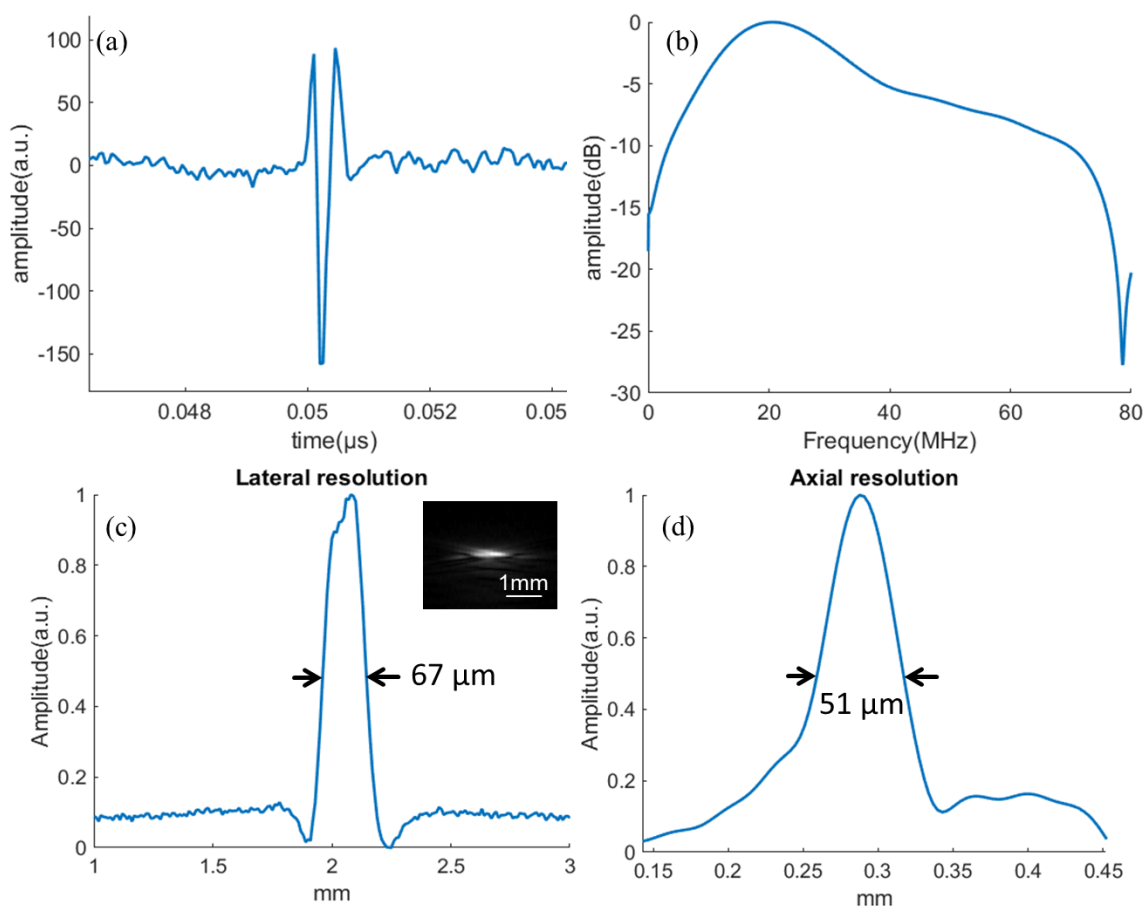


Fig. 4.5. (a) The raw optoacoustic signal of a 10  $\mu\text{m}$  suture. (b) the corresponding frequency spectrum. (c) and (d) are lateral and axial resolution profiles characterized by the suture measurement as shown in the inset of (c).

The endoscopy probe was scanned in radial scanning configuration and a paper phantom with complex structure was imaged. The absorber structure illustrated in Fig. 4.6(a) was printed in paper and then rolled into a plastic tube to form a cylindrical structure as shown in Fig. 4.6(b). The tube has a diameter of 14 mm. The endoscopy probe was inserted inside the plastic tube and positioned in the center. In such arrangement, the paper object was located inside the focus of the transducer. With a rotation speed of 1 frame/second, volumetric image of the phantom was acquired and shown in Fig. 4.6(c). Absorber features are clearly resolved, which matches the reference well. The maximum intensity projection image is shown in Fig. 4.6(d), where structures, like the lines and cross, are well reconstructed. It can be seen that the ellipse regions are recovered with low contrast. The reason can be that the endoscopy probe is shifted from the center axis of the tube, making the ellipses outside of the focus of the transducer.

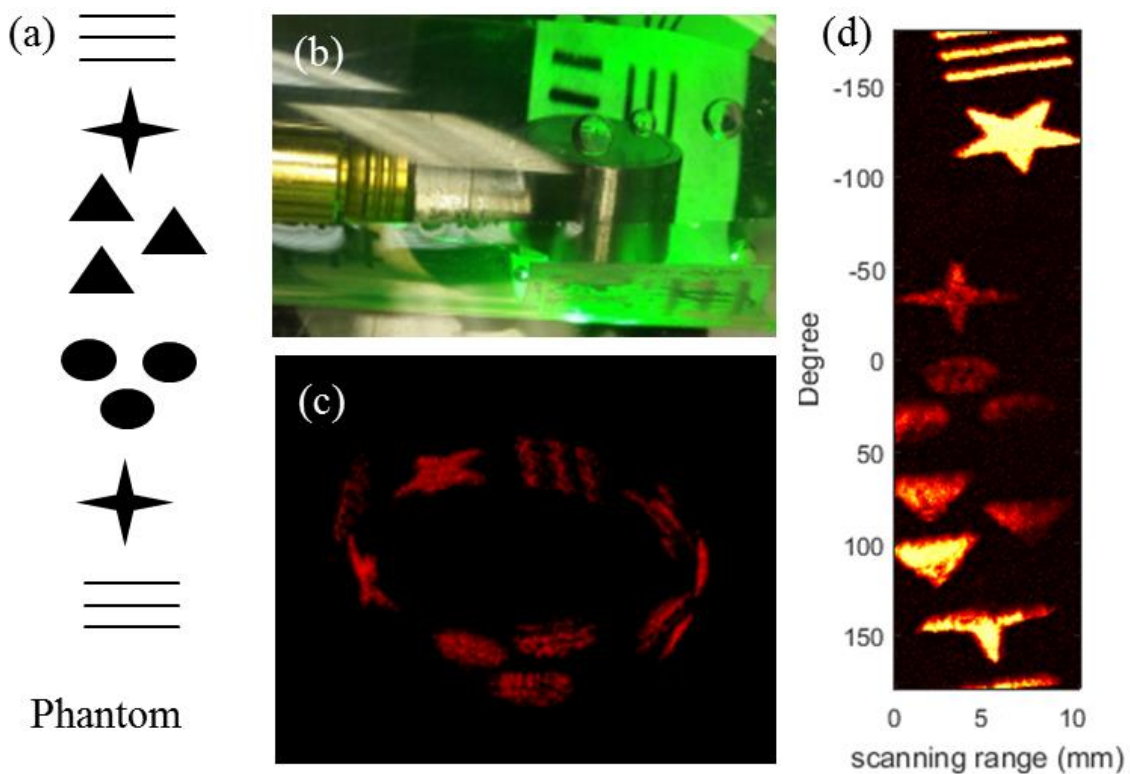


Fig. 4.6. (a) Reference image of the paper phantom. (b) Picture of the phantom and endoscopic probe; (c) Volumetric optoacoustic image. (d) MIP image of the phantom.

## 4.4 Summary and discussion

In this chapter, two implementations of optoacoustic endoscopy systems were introduced. The IVUS based endoscopy probe has diameter of 3.6 mm, which can easily pass through the working channel of video endoscope. The probe is controlled by the proximal actuation mechanism using torque coils to accurately transmit the rotating force. This design has more simplified distal structure with less mechanical components inside the probe. However, limited sensitivity of the IVUS probe and poor resolution restricted the ability of acquiring high quality images. Besides, the limited imaging distance of the IVUS probe only enables partially scanning the esophagus wall of large animals. In the future, high sensitivity IVUS transducers or other types of advanced sensors with minimal size can be used to enhance the performance of this design. In order to improve the image quality, a spherical focused detector based endoscopy probe was implemented. Several phantom measurements were used to characterize the transducer and results have showed that high quality images were

reconstructed in the focus regions of the detector. Biological samples, including esophagus tissues from human and pigs, will be measured to validate the practicability of the developed endoscopy systems and corresponding results will be introduced in chapter 7.

## **Chapter 5     Importance of ultrawide bandwidth for endoscopy performance**

Optoacoustic (photoacoustic) imaging has been successfully shown to resolve anatomical and functional features beyond the penetration depth of pure optical imaging, which indicate great potential to widely impact endoscopic applications. In-vivo rat and rabbit esophagus measurements have been reported [52-55]. The capability of resolving layers of esophagus samples from human or pigs have been shown in previous sections. In order to further enhance the performance of optoacoustic endoscopy on measuring esophagus samples, the necessary detection bandwidth of ultrasound transducers used for optoacoustic esophagus imaging is studied. In this chapter, we simulate the frequency response of esophagus wall and then validate the simulation results with experimental pig esophagus measurements. Utilizing two detectors with 15 and 50 MHz center frequencies, phantom and fresh pig esophagus samples are measured to compare the imaging performance of both detectors. Furthermore, we analyze the frequency bandwidth of optoacoustic signals in relation to morphological layer structures of the esophagus wall. This study will help to optimize the selection of ultrasound transducers for esophagus imaging.

### **5.1 Introduction**

Optoacoustic endoscopy has been considered as an alternative endoscopy technique, which is administered analogously to OCT but allows visualization of hemodynamic and molecular contrast [52, 54, 79]. In addition, optoacoustics can penetrate deeper than OCT, possibly allowing more comprehensive staging. Optoacoustic imaging is insensitive to photon scattering within biological tissues, providing high-resolution optical visualization deeper in tissue than conventional optical imaging methods. [7, 9]. Multispectral optoacoustic methods have been widely applied to resolve vascular structures and tumor hypoxia, as well as the bio-

distribution of targeted photo-absorbing agents or circulating particles [6, 8]. Optoacoustic endoscopy has been shown to resolve the superficial vascular structure of the esophageal lumen of rats and rabbits [52-55]. However, imaging of human esophageal lumen has not yet been investigated. The layer thickness of the mucosa and submucosa in the human esophageal wall varies from a few hundred  $\mu\text{m}$  to millimeters, which is markedly greater than the thickness of rat and rabbit esophageal wall, possibly requiring different operational characteristics in terms of detected bandwidth. Blood vessels in these layers range from thin capillaries with a diameter of several  $\mu\text{m}$  located in the lamina propria layer to larger vessels with a diameter of up to a hundred  $\mu\text{m}$  in deep layers [96]. Thus, the frequency content of optoacoustic signals generated in the esophagus wall is intrinsically broadband.

In this study, we interrogated the frequency bandwidth that is best suited for human esophageal imaging. This investigation relates to the selection of a transducer for developing an optoacoustic endoscope for human studies. First, we performed simulations to explore the frequency response of different layer structures in the esophagus wall. Then, we employed two intravascular ultrasound transducers with central frequencies of 15 and 50 MHz to measure esophageal samples. Images acquired with the two transducers were analyzed to identify the frequency contributions of different layers in the esophageal wall. We summarize our findings and discuss the implications in the selection of components for esophageal optoacoustic endoscopy.

## **5.2 Simulations and experimental measurement**

### **5.2.1 Simulations**

To understand the requirements needed for optoacoustic imaging of esophagus wall, we simulated the optoacoustic response of main absorbers in different layers of esophagus wall. The simulated esophagus wall of human is composed of several different tissue layers as illustrated in Fig. 5.2(a). From the lumen outwards, the superficial structures include epithelium lamina propria, muscularis mucosa, submucosa and muscularis propria [96]. The main optoacoustic source of the esophagus wall comes from hemoglobin at wavelength of 532 nm. The epithelium is composed of a layer of epithelial cells, while the lamina propria

contains rich capillaries and lymph vessels, measuring around 10 to 20  $\mu\text{m}$  in diameter [96]. The muscularis mucosa is mainly composed of several thin layers of smooth muscle fibers. These three layers are termed as the mucosa layer. Besides, blood vessels and lymphatic vessels (ranging from 30 to 50  $\mu\text{m}$  in diameter) run through the submucosa layer [96]. The muscularis propria is a thick layer of muscular fibers, where blood vessels with diameter up to 100  $\mu\text{m}$  exist [96]. For the simulation, all layer structures enriched with blood vessels are selected. The frequency responses of vessels with diameters of 10  $\mu\text{m}$  in LP layer, 30 and 50  $\mu\text{m}$  in SM layer and 100  $\mu\text{m}$  in MP layer are calculated to ensure the simulated model close to the real esophagus wall. The optoacoustic signal simulation was based on the analytical solution of the pressure wave equation for a homogenous spherical absorber with radius  $a$  positioned at  $r_s$  [57]:

$$p_\delta(r, t) = p_0 U(a - |R - v_s t|) \frac{(R - v_s t)}{2R} \quad (5.1)$$

Where  $U$  is the Heaviside function,  $R$  defines as the distance of the absorber from the detection position,  $p_0$  is the amplitude of the initial pressure and  $v_s$  is the speed of sound. Four spheres with radius  $a = 5, 15, 25,$  and  $50 \mu\text{m}$  were simulated respectively, which are selected based on the normal size of vessels in different layers of esophagus wall. The duration of the simulated pulse correlates the propagation time of sound along the sphere diameter, thus scales with the size of the sphere. The theoretical frequency response is obtained by fast Fourier transformation of each simulated optoacoustic signals. For the simulation, acoustic attenuation is not considered. Thus it should be noted that frequencies of the recorded ultrasound waves are lower than the simulated values due to acoustic attenuation and limited detection bandwidth of ultrasound transducers [62].

### 5.2.2 Imaging setup

To validate the simulation results, we performed measurements of phantoms and pig esophagus samples using two detectors with different detection bandwidths. Fig. 5.1(a) shows a schematic of the endoscopy control system, and Fig. 5.1(b) shows a photograph of the distal end of the optoacoustic endoscopy probe. One detector was a commercially available IVUS transducer (2.5-Fr, Atlantis SR Pro, Boston Scientific, Natick, MA, USA) with a central frequency of 15 MHz and a disc-shaped active element of lead zirconate titanate (PZT) with a

diameter of 0.8 mm; the other was a custom-designed IVUS transducer with a central frequency of 50 MHz and a disc-shaped PZT element with a diameter of 0.4 mm. Point-source measurements indicated that the respective acceptance angles of the two detectors were 30 and 40 degrees. Figs. 5.1(c) and (d) indicate the respective simulated sensitivity fields of the two detectors calculated using the software package Field II [23].

Light from a 532 nm laser (Wedge HB532, BrightSolutions SRL, Pavia, Italy) with a pulse repetition rate of 2 kHz was delivered via a 400- $\mu\text{m}$ -core multimode side-viewing fiber. Pulse energy was 1 mJ, and pulse width was 0.9 ns. The laser beam was focused and coupled into the fiber through several lenses (Thorlabs), yielding an optical fluence of approximately 12  $\text{mJ}/\text{cm}^2$  at the fiber tip. In order to optimize optoacoustic sensitivity over a larger depth range, the side-viewing fiber was aligned so that the laser beam was tilted 15 degrees relative to the ultrasound beam. The two beams began to overlap at approximately 2 mm from the sensing surface of the transducer.

The ultrasound detector was connected to a low noise amplifier (63 dB, AU-1291, Miteq, Hauppauge, New York, USA), and amplified signals passed through a hybrid rotary joint (Princetel, USA) to a high-speed digitizer operated at 1 GS/s and 12-bit resolution (CS122G1, Gage, Lockport, IL, USA; maximum sampling rate of 2 GS/s). This arrangement reduced noise generated by the rotary joint during rapid rotation. The endoscopy probe was rotated and translated using mechanical stages (Oriental Motor, Japan). Recorded signals were digitally band-pass filtered based on transducer bandwidth, and images were reconstructed using the Hilbert transform.

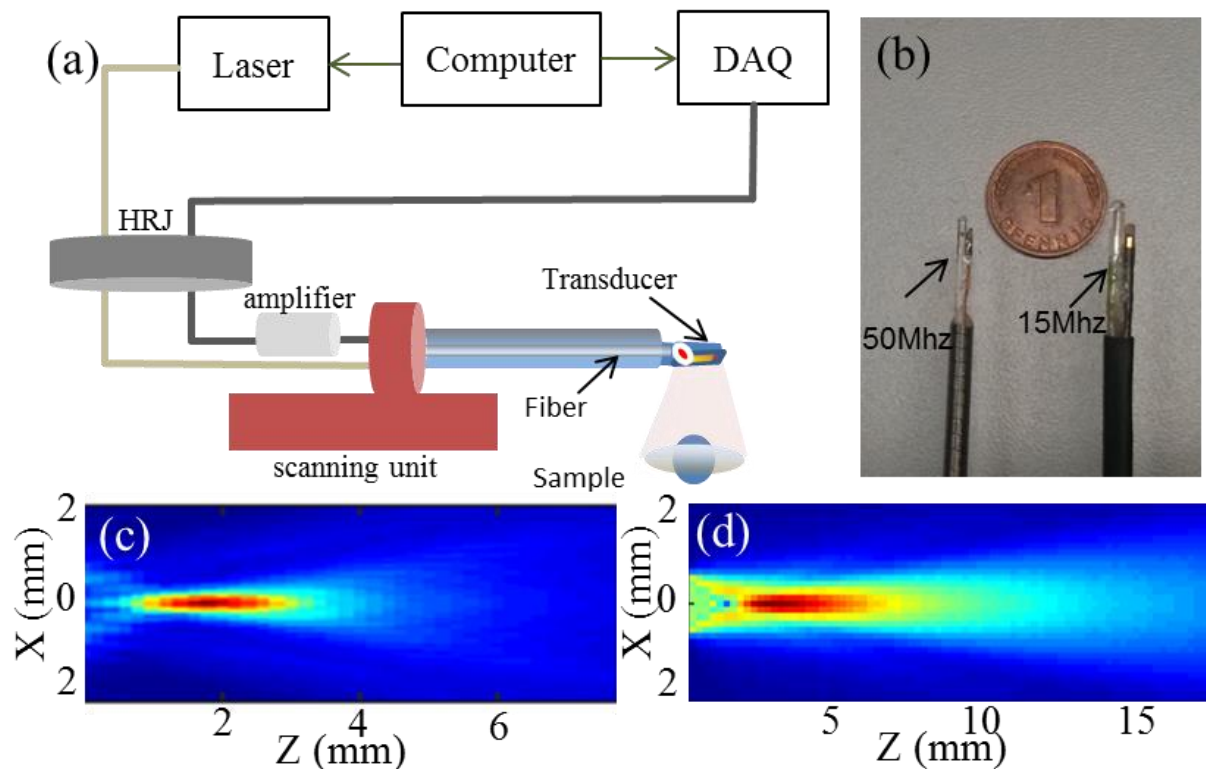


Fig. 5.1. Schematic of the optoacoustic endoscopy system and simulated sensitivity fields of both transducers. (a) Schematic illustration of the endoscopy set-up. (b) Photograph of the distal end of the two endoscopy probes with central frequencies of 15 or 50 MHz. (c,d) Simulated sensitivity fields of the (c) 15-MHz detector and (d) 50-MHz detector.

### 5.2.3 Phantom and tissue measurements

Bandwidth detection characteristics of the two detectors were determined by scanning a phantom consisting of an agar cylinder containing four,  $10\ \mu\text{m}$  microspheres positioned at different depths within the agar. The phantom was scanned along the transversal axis. To prevent the detected optoacoustic signals from being affected by variable illumination effects, the excitation laser beam was guided through a fiber bundle and microspheres were fully illuminated.

For ex vivo experiments, fresh esophageal sections 6 cm long were obtained from a 1-year-old male pig. The sections were cut open and packed into a polyethylene tube to form a cylindrical structure, as shown in Fig. 5.5(a). This facilitated imaging the esophageal tissue, since on its own, the sample tended to collapse onto itself. Samples were imaged along

several sections using linear or radial scanning using both transducers. Optoacoustic images obtained using the 50 MHz detector were reconstructed using data from three frequency bands (5-20, 20-50 or 50-80 MHz), which were selected using appropriate bandpass filters. Our goal was to investigate the signal frequencies contributed by different layers of the esophageal wall.

## **5.3 Results**

### **5.3.1 Simulation results**

Fig. 5.2 shows the simulated optoacoustic response of an esophageal wall. Fig. 5.2(a) shows the layer structure with red structures representing blood vessels, which were assumed to be the only optoacoustic absorbers at the excitation wavelength of 532 nm. This simulation predicts that EP and MM layers will be visualized with lower optoacoustic contrast because of the relatively low abundance of vessels, while the LP, SM and MP layers will be visualized with high contrast. Fig. 5.2(b) shows variations in the simulated blood vessel diameter with increasing depth in the esophageal wall. Fig. 5.2(c) shows the simulated frequency response of blood vessels with different diameters. The simulation predicts that LP capillaries with an average diameter of 10  $\mu\text{m}$  emit a peak frequency of approximately 150 MHz (at -6 dB), much higher than the peak frequencies of 60 MHz emitted by vessels in the SM layer and of 10-20 MHz emitted by larger vessels in the MP layer.

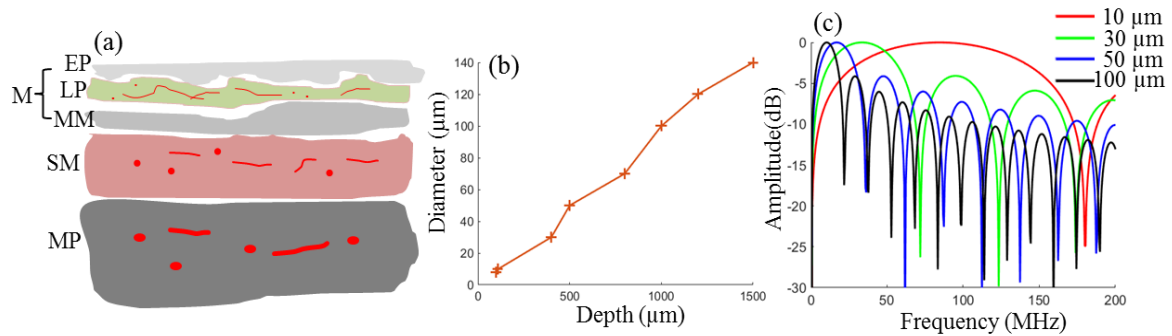


Fig. 5.2. Simulated frequency response of blood vessels in different layers of the esophageal wall. (a) Layer structure of the superficial esophageal wall. Red structures represent blood vessels. EP, epithelium; LP, lamina propria; M, mucosa; MM, muscularis mucosa; MP, muscularis propria; SM, submucosa. (b) Diameter of simulated blood vessels with increasing depth in the esophageal wall. (c) Frequency response of simulated blood vessels with diameters of 10-100  $\mu\text{m}$ .

### 5.3.2 Experimental results

Figs. 5.3(a) and (c) show optoacoustic images of the microsphere phantom based on data collected using the 15 and 50 MHz detectors, respectively. The ultrasound beams diverge with distance from the probe. Figs. 5.3(b) and (d) show lateral and axial profiles of the optoacoustic signal generated by a microsphere located approximately 2 mm from the probe. Based on full width at half-maximum values, axial and lateral resolution were, respectively, 186 and 782  $\mu\text{m}$  for the 15 MHz transducer and 69 and 421  $\mu\text{m}$  for the 50 MHz transducer.

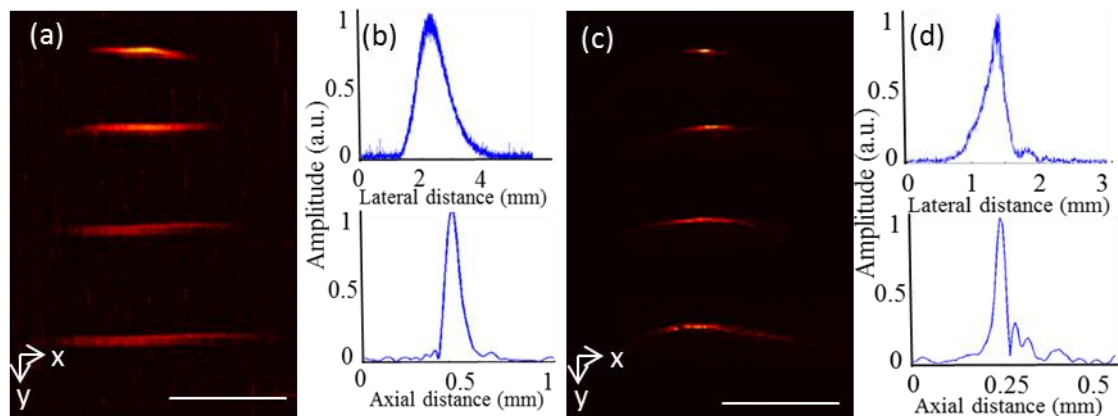


Fig. 5.3. Optoacoustic imaging of a microsphere phantom using the 15- and 50-MHz transducers. (a,c) Images acquired using the (a) 15 MHz or (c) 50 MHz detector. (b,d) Lateral and axial profiles of optoacoustic signal through the first microsphere using the (b) 15 MHz or (d) 50 MHz detector.

To analyze the bandwidth detection characteristics of each detector, we performed a fast Fourier transform of the optoacoustic signals generated by the first microsphere. Fig. 5.4 shows the optoacoustic signal and corresponding bandwidth for each detector. Pulse-width is at least 2-fold narrower for the 50 MHz detector, which explains its higher axial resolution. For the 15-MHz transducer, the central frequency of the spectrum lies at 15 MHz, and bandwidth at  $-6$  dB is 8-22 MHz, corresponding to a fractional bandwidth of 93%. For the 50-MHz transducer, the central frequency lies at 47 MHz, and bandwidth is 20-76 MHz, corresponding to a fractional bandwidth of 110%.

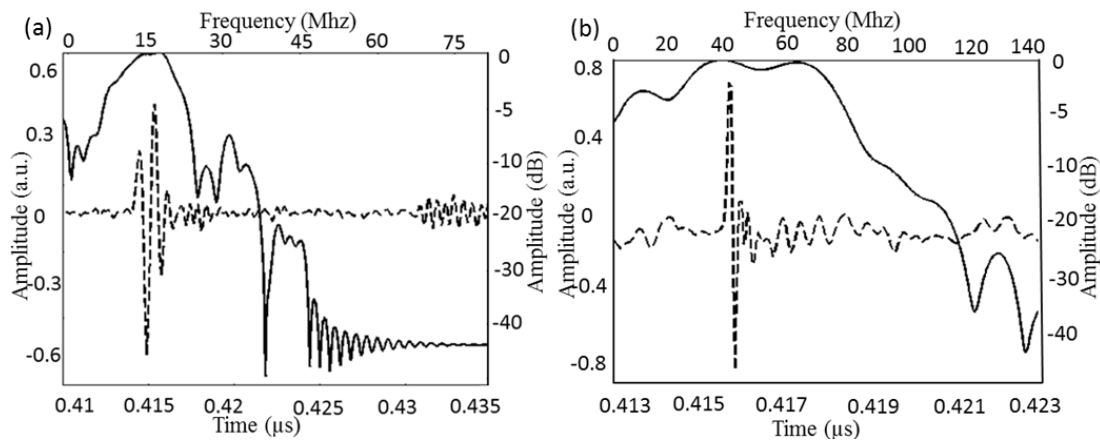


Fig. 5.4. Bandwidth detection by the 15 and 50 MHz transducers during optoacoustic imaging of a microsphere phantom. (a) Raw optoacoustic signal and the corresponding Fourier-transformed spectrum (dashed line) for the 15-MHz detector. (b) Raw signal and spectrum (dashed line) for the 50 MHz detector.

Next we used the two transducers to image *ex vivo* samples of pig esophagus. Fig. 5.5(a) shows the orientation of the sample, which was measured along the longitudinal axis as well as in cross-section. Fig. 5.5(b) shows the layered structure in a longitudinal cross-section of the sample. Figs. 5.5(c) and (d) show optoacoustic images of a longitudinal section corresponding approximately to the position shown in Fig. 5.5(b). Figs. 5.5(e) and (f) show optoacoustic images of a cross-section from the same sample. The 15 MHz probe achieves penetration depth over 2 mm; however, it does not resolve vessel structures in mucosa well, and it fails to resolve the EP, LP and MM layers. Vascular structures in the SM and MP layers are resolved poorly. The 50 MHz probe, in contrast, resolves vessel structures better, but at shallower depths (approximately 1.5 mm). The 50 MHz probe also resolves the layers of the mucosa better, as indicated by the blue dashed lines in Fig. 5.5(d). Both transducers reveal clear separation between the mucosa and SM layer, despite the fact that the intervening MM layer comprises several thin layers of smooth muscle fibers, which are expected to show low optoacoustic contrast relative to neighboring tissue.

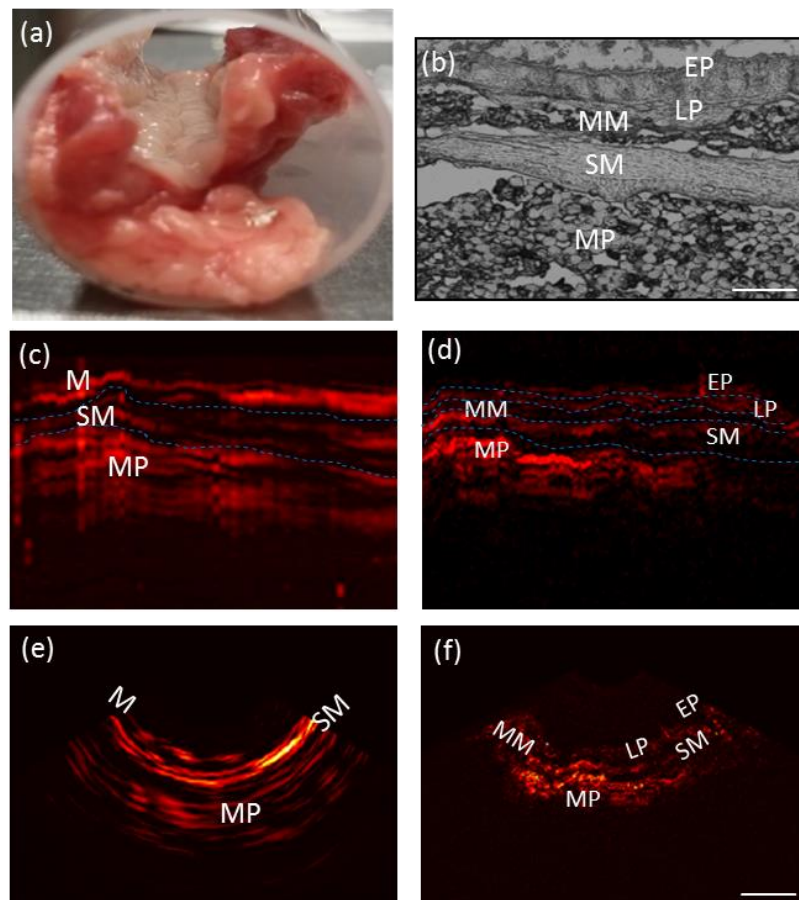


Fig. 5.5. (a) The picture of the rolled esophagus sample; (b) A histological image of the sample along the longitudinal direction. (c) and (d) are sectional optoacoustic images corresponding to the sliced position of (b) acquired by the 15 and 50 MHz detectors. Blue dash lines are used to help identifying layer structures. (e) and (f) are cross-sectional images of the sample acquired by the 15 and 50 MHz detectors. Abbreviations: EP, squamous epithelium; LP, lamina propria; MM, muscularis mucosa; M, mucosa (including the EP, LP and MM layers); SM, submucosa; MP, muscularis propria. Scalebar 500  $\mu\text{m}$ .

Finally, we examined which frequency bands in the optoacoustic signal are important for reconstructing the layers of the esophageal wall. Fig. 5.6 shows optoacoustic image reconstruction of a cross-section of pig esophagus using different frequency bands collected using the 50 MHz detector. Fig. 5.6(a) shows the image reconstructed using all frequencies in the detection bandwidth. Fig. 5.6(b) shows the image reconstructed using 5-20 MHz; this image clearly shows the MP layer, while the mucosa and SM layer are less well resolved, and imaging depth does not extend past 1.5 mm. This image is similar to the one in Fig. 5.5(c), acquired using the full detection bandwidth of the 15 MHz transducer. Fig. 5.6(c) shows that

reconstruction using 20-50 MHz reveals detailed structure in the mucosa and SM layer at depths down to 1 mm. Fig. 5.6(d) shows the reconstruction using 50-80 MHz, which reveals fine structures, such as capillary dots in the LP layer and vessel edges in the SM layer, albeit to a limited penetration depth of only 600  $\mu\text{m}$ . These results indicate that the layer features of the esophageal wall are visualized much better by combining all frequency bands collected by the 50-MHz transducer.

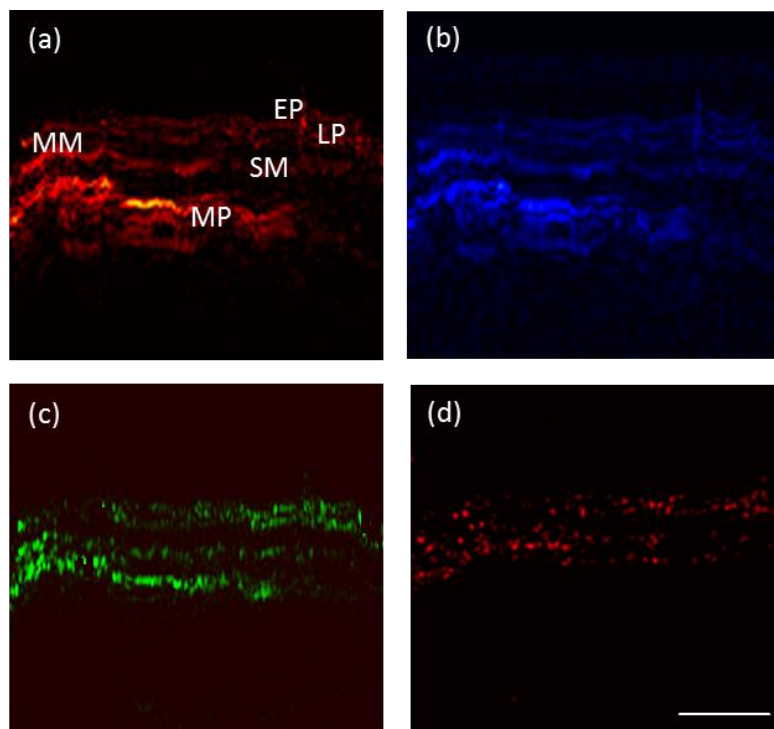


Fig. 5.6. Sectional optoacoustic images of esophagus wall with different frequency contents. (a) Reconstruction result of all frequency contents within the detection bandwidth of the 50 MHz IVUS sensor (5-80 MHz); (b) 5-20 MHz; (c) 20-50 MHz; (d) 50-80 MHz. Scalebar 500  $\mu\text{m}$ .

## 5.4 Summary and Conclusion

This study examined what optoacoustic detection bandwidth is necessary for esophagus imaging in order to reconstruct the layered structure of the esophageal wall. Simulations suggested that a wide frequency band is necessary, and this was confirmed in imaging experiments with ex vivo pig esophagus. The 50-MHz detector was better than the 15 MHz detector at resolving the LP and SM layers, although the 15 MHz detector was able to image

deeper. Optoacoustic signals ranging from 5 to 20 MHz corresponded mainly to gross structure in the MP layer, signals from 20-50 MHz corresponded to finer structure, especially in the LP and SM layers, and signals from 50-80 MHz corresponded to even finer features of the LP and SM layers. Small vessel structures could not be adequately imaged even when detecting the full bandwidth of the 50-MHz detector (5-80 MHz). These results suggest that ultrawide bandwidth detectors ranging from a few MHz to 100 MHz can provide reasonable resolution of esophageal layers.

Our work with phantoms and *ex vivo* samples has identified two hardware and software limitations that need to be addressed when developing optoacoustic endoscopic probes. One limitation is the apparent trade-off between the ability to resolve esophageal layers, which was better with the 50 MHz detector in our experiments, and the ability to resolve features deeper within the wall, which was better with the 15 MHz detector. Both abilities are critical for esophageal cancer staging [14, 46, 97]: high-resolution imaging of the esophageal wall allows detailed analysis of the mucosa and SM layer, which is important for detecting esophageal cancer in earlier stages; deeper imaging offers the possibility of detecting more advanced lesions that have invaded into the wall [15, 98]. The development of accurate optoacoustic endoscopes will require optimizing this trade-off. A good solution may be an ultrawide bandwidth transducer covering the bandwidths of the 15 and 50 MHz detectors or an even wider bandwidth. Such transducers are commercially available, but they are too large for endoscopy applications.

The second limitation identified in our work is the finite aperture effect of the detector, which led to relatively low lateral resolution in our reconstructed images. Although it may be possible to improve this resolution using more advanced reconstruction methods, this is likely to be extremely challenging in the case of endoscopy imaging [90]. A potentially more feasible option is to use focused ultrasound detectors that can provide high-resolution images at the focus [52, 55].

The present study makes clear that ultrawide bandwidth transducers are necessary for optoacoustic endoscopy capable of resolving the layers of the esophageal wall. It further suggests the need to strike a reasonable balance between resolution and imaging depth in

order to permit accurate early staging of esophageal cancer. The present work may help guide the design of optoacoustic endoscopes that are more accurate than ultrasound and provide more clinically useful information than confocal or OCT.

## **Chapter 6 Image quality enhancement methods**

In this chapter, two improved optoacoustic image reconstruction methods are introduced to enhance the reconstruction performance. These approaches can be applied to reconstruct datasets acquired in the curved and linear scanning endoscopy. Moreover, they can be used to enhance image quality of tomography configurations.

Section 6.1 presents an improvement of the fast converging Split Augmented Lagrangian Shrinkage Algorithm method based on Sparse Equations and Least Square (LSQR) inversion for improving the reconstruction speed. We further show image fidelity improvement when using a coherence factor to weight the reconstruction result. Phantom and *in vivo* measurements demonstrate that the proposed method provides images of reduced artifacts and faster convergence compared to existing sparse recovery methods.

Section 6.2 investigates a method that integrates information from multiple optoacoustic images acquired at sub-diffraction steps into one high resolution image by means of an iterative registration algorithm. Experimental validations performed in target phantoms and ex-vivo tissue samples confirm that the suggested approach renders significant improvements in terms of optoacoustic image resolution and quality without introducing significant alterations into the signal acquisition hardware or inversion algorithms.

### **6.1 Accelerated sparse recovery method**

Model-based approaches are capable of incorporating information regarding detection geometry, acoustic attenuation, and transducer properties in the reconstruction process [99, 100], resulting in more accurate reconstructions. However, model-based methods require large numbers of repeated sparse matrix-vectors multiplications in an iterative manner, which results in significant computational cost [65, 71]. Accelerated model-based methods were developed to reduce the computation cost [71-73]. For example, the angular discretization

method was used to generate the model matrix, which effectively reduced the computational cost and saved memory [71, 72]. Other approaches performed inversion on parallel-processing platforms based on GPU, which enabled real-time model-based reconstruction [73, 74].

A particular challenge in optoacoustic tomography is the implementation of limited-view projections, i.e. cases where 360-degree projections are not available. This could be the case for example in imaging large volumes (whole-animals or humans), whereby access is afforded only from one side of the tissue, in analogy to ultrasound imaging. Limited-view implementations typically results in lower image fidelity and a larger number of artifacts compared to 360 degrees view datasets [65]. Nevertheless, sparsity based algorithms were shown to perform better with limited view datasets [65, 101, 102], compared to Tikhonov based reconstructions, albeit at a higher computational cost. Moreover, sparse recovery based methods may amplify noise in limited-data scenarios [103].

In this section, the sparse method proposed was implemented to accelerate the reconstruction process implemented within the SALSA framework, using least square QR (LSQR) inversion and a novel coherence factor weighting scheme for suppressing noise and artifacts[104]. The reconstruction performance was validated on several phantoms and biological tissue *ex vivo* to quantify improvements over previously described SALSA implementations.

### 6.1.1 Methods and materials

#### A. Acoustic Forward Problem

The generation and propagation of the acoustic wave is given by the following wave equation [59, 60]:

$$(\nabla^2 + k_a^2)p(r, t) = -\frac{\beta}{c_p} \frac{\partial H(r, t)}{\partial t} \quad (6.1)$$

where  $p(r, t)$  indicates the acoustic pressure at a position  $r$  and time  $t$ ,  $H(r, t)$  indicates the heating function, which is obtained as a product of absorption coefficient and light fluence.  $\beta$  is the thermal expansion coefficient of the tissue and  $C_p$  is the specific heat at constant pressure.  $k_a$  represents the acoustic wave number given as  $k_a = \omega/v_s$ , where  $\omega$  is the temporal

frequency and  $v_s$  is the speed of sound. Note that the heating function is independent both spatially and temporally i.e.  $H(r,t) = H_r(r)H_t(t)$ . The solution for the above equation is given as,

$$p(r, t) = \frac{\beta v_s}{4\pi c_p} \frac{\delta}{\delta t} \int_{R=v_s t} \frac{H_r(r')}{R} dA' \quad (6.2)$$

whereby  $R=|r-r'|$  and spherical integration is performed over surface element  $dA'$ . This integral is discretized to form a model matrix using an interpolated model matrix method to result in the following matrix equation,

$$Ax = b \quad (6.3)$$

where  $b$  is the recorded data and  $x$  is the reconstruction image.  $A$  is obtained by linear interpolation of the heating function over the image grid.

### B. Regularization & Inversion

Efficient inversion of Eq. 6.3 requires regularization. We selected conventional Tikhonov regularization with parameter ( $\lambda$ ), assuming an initial pressure rise distribution that is smoothly varying. The objective function to be minimized is given as,

$$\Omega = \|Ax - b\|_2^2 + \lambda \|x\|_2^2 \quad (6.4)$$

whereby  $\| \cdot \|_2$  represents the L2 norm. The above objective function can be solved using normal equations [68], i.e.,

$$x_{tikh} = (A^T A + \lambda I)^{-1} A^T b \quad (6.5)$$

However, Eq. 6.5 is computationally expensive due to the time-consuming matrix inversion. Alternatively, an LSQR approach can be employed [69], i.e.

$$x_{LSQR} = V_k ((B_k^T B_k + \lambda I_k)^{-1} \beta_0 B_k^T e_1) \quad (6.6)$$

whereby  $B_k$  represents a bi-diagonal matrix,  $V_k$  is the right orthogonal matrix resulting from Lanczos bidiagonalization [69, 70] and  $\beta_0$  is defined as  $\|b\|_2^2$ .  $e_1$  is  $[1 \cdots]^T$ . Eq. 6.6 can be inverted in a faster fashion compared to Eq. 6.5 since it involves inverting the bidiagonal matrix, which is computationally efficient.

### C. Proposed SALSA acceleration with coherence factor

The proposed method is based on applying a sparsity constraint and accelerating the reconstruction with the help of bidiagonal matrices. The accelerated Split Augmented Lagrangian Shrinkage Algorithm (ASALSA) is proposed herein as an improved version of SALSA minimization implemented using Krylov subspace optimization. In this case, the objective function to be minimized is,

$$\Omega = \|Ax - b\|_2^2 + \lambda \|x\|_1 \quad (6.7)$$

Sparsity optimization schemes are expected to offer better performance over conventional Tikhonov regularization for limited projection data [105, 106]. Eq. 6.4 assumes a smooth solution and hence results in large number of unknowns and edge smoothing. Eq. 6.7 assumes the number of unknowns to be sparse (by considering only non-zero entries) and is known to perform well in limited data scenarios. Eq. 6.7 is minimized using the SALSA scheme, which has demonstrated the fastest convergence among existing sparsity norm based optimization schemes [107]. In this scheme, we utilize a variable splitting approach, wherein a new variable is introduced in the optimization procedure. The above objective function is now split into two quadratic minimizations with the help of the temporary variable ( $v$ ) given as,

$$\omega = \|Ax - b\|_2^2 + \alpha \|x - v_k - d\|_2^2 \quad (6.8)$$

$$\tilde{\omega} = \lambda \|x\|_1 + \frac{\alpha}{2} \|x_{k+1} - v - d_k\|_2^2 \quad (6.9)$$

where  $\alpha$  represents the regularization parameter (depends on the noise). Eq. 6.8 is solved using a *maximum a posteriori* (MAP) based algorithm to obtain an estimate for initial pressure rise ( $x$ ). Eq. 6.9 is minimized to obtain an estimate for  $v$ , using a soft thresholding operation (which acts as a derivative for sparsity minimization). The update for the alternated direction method of multiplier (ADMM) parameter is given as  $d_{k+1} = d_k - (x_{k+1} - v_{k+1})$ . The minimizations in Eqs. 6.8 and. 6.9 and the ADMM parameter update are repeated until convergence.

The original SALSA algorithm involved inversion of a large matrix during the optimization procedure [107]. To accelerate inversion, we recast the SALSA algorithm, as indicated in Table I, by using the LSQR solver. Faster computations are achieved by using LSQR iterative inversion schemes for enabling accelerated SALSA (termed as ASALSA) reconstruction

using the L1-norm based approach. It can be seen that Eq. 6.4 applies a smoothness constraint ( $\|x\|_2$ ); hence noise will be smoothed out during reconstruction. Conversely, since Eq. 6.7 applies sparsity constraint, it may amplify weak signal and noise [103]. To suppress noise amplification and artifacts arising due to limited view data and sparsity constraint, we introduce herein an additional operation using a coherence factor (CF) [108, 109], defined as the ratio between the energy of the coherent sum of optoacoustic signals to the total incoherent energy, i.e.

$$CF(i) = \frac{|(x_{recon})_i|^2}{N \sum_{i=0}^N |(x_{back})_i|^2} = \frac{|(x_{recon})_i|^2}{A^T b^2} \quad (6.10)$$

where  $N$  represents the total number of pixels in the reconstructed domain.  $x_{recon}$  is the reconstructed image obtained using ASALSA and  $x_{back}$  is the backprojection reconstruction. The numerator in Eq. 6.10 represents the energy of the coherent sum of the signals, and the denominator is the total energy sum. The CF values can be interpreted as a focusing quality index estimated from the measured optoacoustic data, ranging from 0 to 1. It is maximal when all signals emitted by an optoacoustic absorber at position  $r'$  arrive in same phase at the different detector positions  $r$ . After being projected, real signals will constructively superimpose on their point of origin. In this way, good focusing properties can be achieved and consequently a sharp reconstruction. Conversely, incoherent signals will not superimpose on their point of origin after summation, but rather smear out, overall resulting into degradation of image quality. Weighting the amplitude of each image pixel with the corresponding CF can therefore suppress contributions from incoherent signals, which enables identification of noise/artifacts in the reconstructed image and consequently thresholding them. Therefore, the CF is further used for weighting the reconstructed image given as,

$$x_{recon} = CF .* x_{recon} \quad (6.11)$$

This CF weighting enables amplification of the higher optoacoustic signal, and suppresses the noise. The ASALSA algorithm along with the CF is indicated in Table 1.

TABLE I ASALSA-CF Algorithm

<p><b>Aim:</b> Estimation of <math>x</math> by solving Eq. (7).</p> <p><b>Input:</b> <math>A, b, \lambda, \alpha, \text{max\_iter}</math></p> <ol style="list-style-type: none"> <li>1. Output: <math>x</math></li> </ol> <p>Initialize ADMM parameter <math>d=0</math>.</p> <ol style="list-style-type: none"> <li>2. Calculate backprojection solution (<math>x=A^T b</math>), <math>CF=A^T b^2</math></li> <li>3. for <math>k=1,2,\dots,\text{max\_iter}</math></li> <li>4. Optimize Eq. (9): <math>v = \text{soft}(x+d, (0.5 * \lambda) / \alpha)</math></li> <li>5. Optimize Eq. (8): <math>x_l = \mathcal{S}_k((C_k^T C_k + \lambda I_k)^{-1} \beta_1 C_k^T e_1)</math>, where matrix <math>C</math> is obtained by Lanczos bidiagonalization of <math>A^T</math> with <math>k</math> iterations and <math>\beta_1</math> is the euclidean norm of <math>(A^T b + \alpha * (v-d))</math>.</li> <li>6. <math>x_{\text{recon}} = M_k((H_k^T H_k + \lambda I_k)^{-1} \beta_2 H_k^T e_1)</math>, where <math>\beta_2</math> is the euclidean norm of <math>x_l</math>.</li> <li>7. Update ADMM parameter: <math>d=d+x_{\text{recon}}-v</math></li> <li>8. end</li> <li>9. <math>CF = (x^2/CF)</math></li> <li>10. <math>x = x_{\text{recon}} * CF</math></li> </ol>
---

#### D. Optoacoustic imaging system

A multispectral optoacoustic tomography small animal scanner (MSOT256-TF, iThera Medical GmbH, Munich, Germany) was employed to experimentally examine the performance of the proposed reconstruction method. In brief, a custom-made 256-element cylindrically-focused array was used to record the optoacoustic signals. The ultrasound array covered an angle of approximately  $270^\circ$  with a radius of 40 mm, allowing simultaneous acquisition of the signals generated with each laser pulse. The central frequency of the array elements was 5 MHz with a bandwidth of 90%. The sample was illuminated with a wavelength-tunable optical parametric oscillator laser with 10 Hz repetition rate. The detected optoacoustic signals were simultaneously digitized at 40 Megasamples per second and were averaged 10 times to improve the SNR of the signal. Detailed information about the imaging setup can be found in [5, 110, 111].

### E. Phantom and tissue experiments

In order to test the performance of the proposed method, a printed paper (USAF resolution target, standard inkjet printer with black ink) embedded in a 1.9 cm diameter diffuse agar cylinder (6% by volume intralipid in the agar solution) was imaged. The absorbing features of the phantom are shown in Fig. 6.1(a). The phantom consisted of several groups of line elements of different sizes, which can be used for resolution and image quality characterization at different levels. In order to mimic limited-view scenarios, we assumed two down-sampled data sets, one employing 128 positions over 270 degrees coverage angle and one employing 128 positions over 135 degrees coverage angle.

A tissue mimicking agar phantom was also prepared to examine the ASALSA-CF performance. The phantom contained areas containing 0.016% India ink to impart higher optical absorption than background. The absorption coefficient of the ink-containing inclusions was  $\mu_a = 1.6 \text{ cm}^{-1}$ . In addition, a hollow cylindrical cavity was introduced for illustrating the nature of artifacts produced due to acoustic mismatches. The phantom was used to examine the performance of the proposed algorithm in relation to artifacts arising due to reflecting material.

Furthermore, a mouse kidney was imaged *ex vivo* to examine the performance of the proposed method with biological tissue. The kidney sample was extracted post-mortem (non-perfused) according to institutional regulations regarding animal handling protocols and subsequently embedded in a diffuse agar block (6% by volume intralipid in the agar solution) for ensuring uniform illumination of the sample.

### F. Image Reconstruction

The performance of reconstructions based on Eq. 6.6 (L2-norm), Eq. 6.8 and 6.9 (ASALSA) and Eq. 6.11 (ASALSA-CF) was compared using the experimental measurements collected from phantoms and mouse kidneys. Prior to reconstruction, the optoacoustic signals were band-pass filtered with cut-off frequencies between 0.2 and 7 MHz in order to remove low frequency off-sets and high frequency noise. A uniform speed of sound of 1510 m/s was used for all the reconstructions[112]. For all phantom measurements, images were reconstructed

with a pixel size of  $100\ \mu\text{m}$  ( $200 \times 100\ \text{pixels}^2$ ), and in the case of tissue data a pixel size of  $100\ \mu\text{m}$  ( $200 \times 180\ \text{pixels}^2$ ) was used. The regularization parameter for the L2-norm based scheme was obtained using an L-curve approach while in case of ASALSA algorithm, it was chosen heuristically. The parameters  $\alpha$  and  $\lambda$  were set as 100 and 1500 for the ASALSA algorithm. Note that in case of ASALSA algorithm, we have multiple parameters ( $\alpha$  and  $\lambda$ ) which are sensitive to noise, therefore they can be adjusted based on the image quality of the reconstructed image.

In order to further quantify the reconstruction improvement, the average intensity ( $S$ ) of the resolution lines were calculated for the paper phantom, as well as the standard deviation of background ( $B$ ) signals in the spaces between the lines. The ratio of the average signal to the standard deviation of background noise provided a contrast ratio  $CNR = 20 * \log(S/B)$ .

### 6.1.2 Results

The reconstruction results corresponding to the printed-paper USAF-resolution phantom using 256 detector elements over  $270^\circ$  are depicted in Fig. 6.1. Fig. 6.1(a) shows the structure of the paper phantom. Fig. 6.1(b) is the image reconstructed by L2-norm scheme whereas Fig. 6.1(c) indicates the reconstructed image obtained by ASALSA method. Both reconstructions result in similar initial pressure rise distribution. In contrast, the proposed ASALSA-CF method achieves sharper structure and lesser background artifacts compared to the other results. The artifact reduction is apparent from the zoomed in areas shown in the insets of Fig. 6.1(b)-(d), the zoomed region is indicated by red rectangle in Fig. 6.1(a). Even though the image intensity of line features [label 1 marked in (b)] is partially distorted, the line profiles along the red dash line indicated in Fig. 6.1(b) [shown in Fig. 6.1(e) and (d)], suggest that line features are better resolved in the image reconstructed by the proposed method.

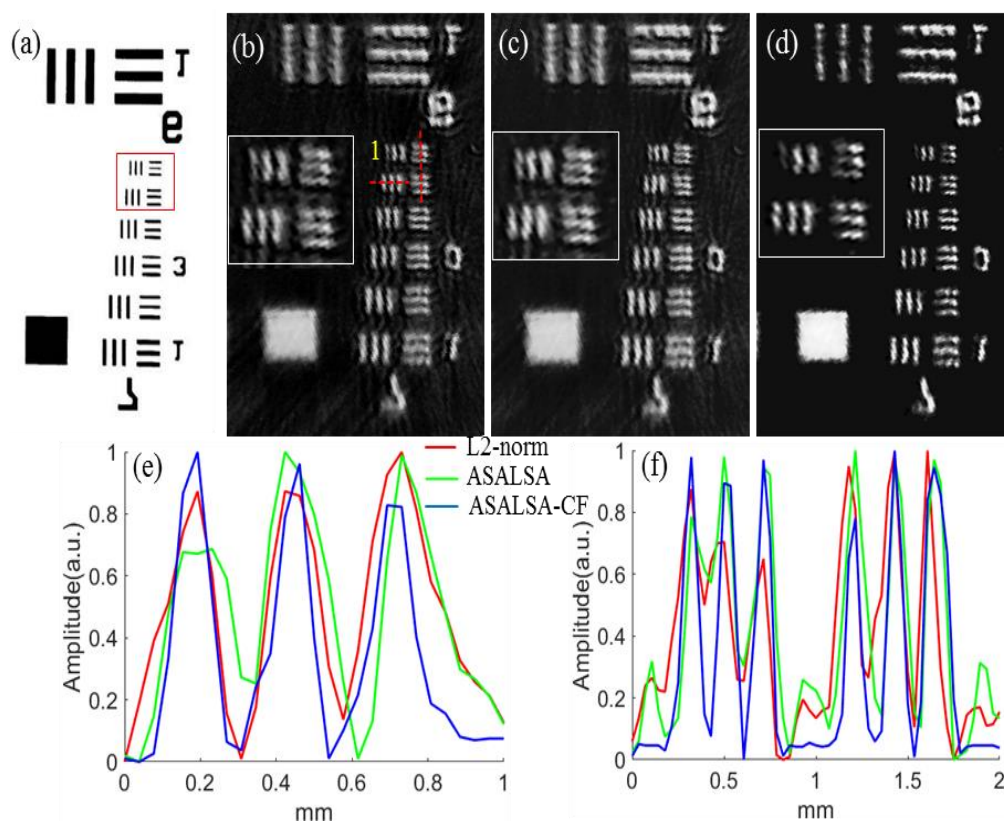


Fig. 6.1. (a) Reference USAF phantom printed on white paper with black ink, which was embedded in scattering agar. (b) The reconstructed image by L2-norm. (c) ASALSA method and (d) the proposed method. The subjects in (b-d) are the zoom-in of region marked in red rectangle of (a) respectively. The line profiles in the horizontal and vertical directions marked in panel (b) are represented in (e) and (f) respectively.

Results of the limited data situation (128 positions over  $270^\circ$ ) are depicted in Fig. 6.2. Fig. 6.2(a) shows the result reconstructed with L2-norm based algorithm. Due to limited dataset, the line features (labels 1 and 2) are heavily blurred. However, the image obtained by ASALSA method recovers the absorbing features much better compared to L2-norm based approach. Fig. 6.2(c) displays the result obtained by the proposed method (ASALSA-CF), where the line features are better distinguishable as observed in the zoomed areas. In analogy to Fig. 6.1, Fig. 6.2(c) shows fewer artifacts compared to the results reconstructed by other methods. The lateral and axial line profiles marked by the red lines in Fig. 6.1(b) also suggest significant resolution improvement achieved by the proposed reconstruction method on highly undersampled data.

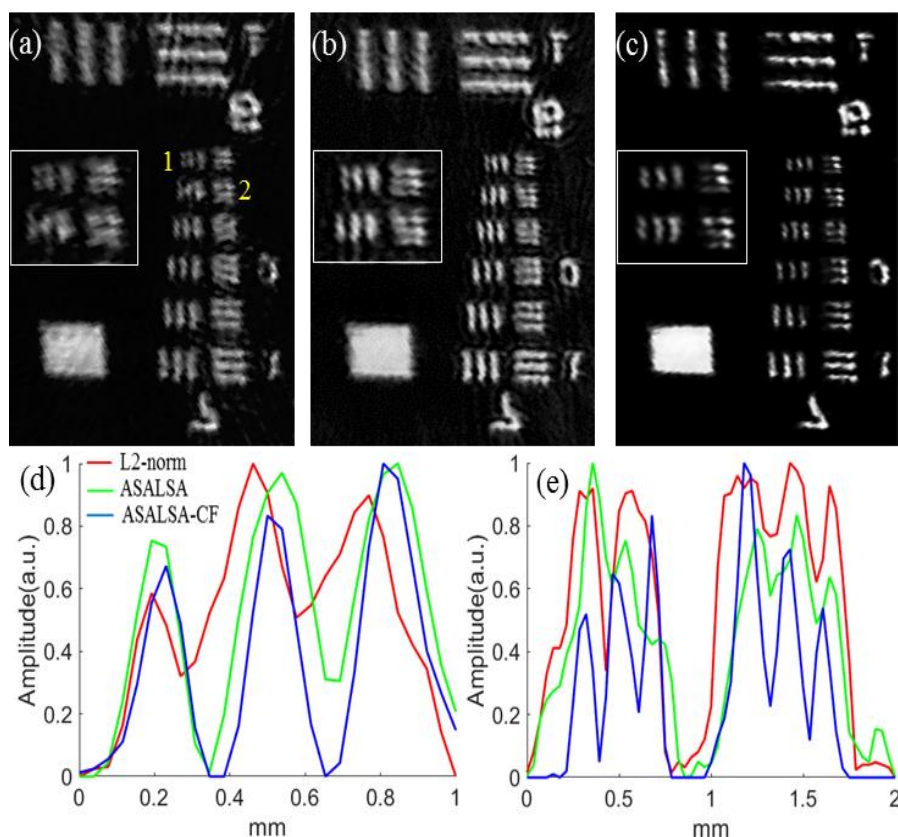


Fig. 6.2. Images reconstructed using 128 transducer positions over 270 degrees. (a) The reconstructed image by L2-norm. (b) ASALSA method and (c) the proposed method. The subjects in (a-c) are the zoom-in of region marked in red rectangle of Fig. 1(a) respectively. The line profiles in the horizontal and vertical directions marked in panel Fig. 7.1(b) are represented in (d) and (e) respectively.

Undersampled data with limited-view condition (128 transducer positions over 135 degrees) are reconstructed and the corresponding results are shown in Fig. 6.3. The L2-norm based reconstruction is fully distorted and blurred. Line features (labels 1 and 2) in Fig. 6.3(a) cannot be identified. In contrast, the ASALSA method shows better performance in resolving the line pattern. Clearly, both images contain artifacts and blurry regions. However, Fig. 6.3(c) shows fewer artifacts and line features are better resolved compared to the other reconstruction results indicating the superiority of the proposed scheme. Line profiles and zoomed images present similar resolution improvement as in previous cases. Meanwhile, the CNR values of line features (yellow labels 1, 2, 3 and 4) are calculated and displayed in Table II. It can be seen that the ASALSA-CF method achieve better image contrast than the other methods.

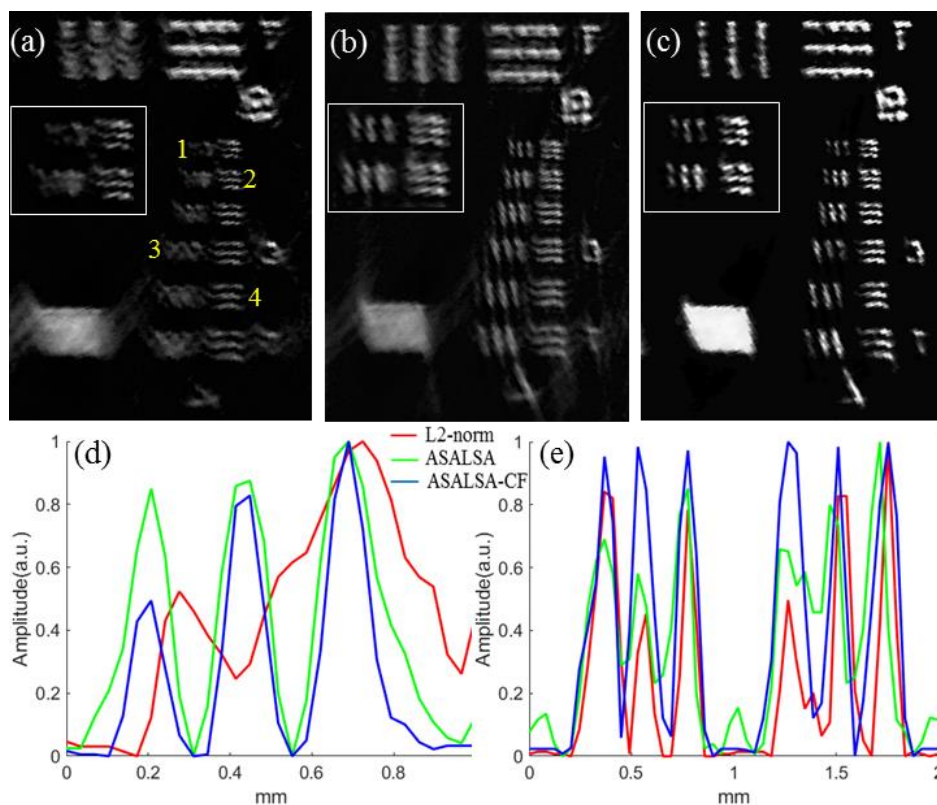


Fig. 6.3. Images reconstructed using 128 transducer positions over 135 degrees. (a) The reconstructed image by L2-norm. (b) ASALSA and (c) the proposed method. The subjects in (a-c) are the zoom-in of region marked in red rectangle of Fig. 1(a) respectively. The line profiles in the horizontal and vertical directions marked in panel Fig. 6.1(a) are represented in (d) and (e) respectively.

TABLE II  
CONTRAST (CNR) COMPARISON

Methods	OBJECT 1	OBJECT 2	OBJECT 3	OBJECT 4
L2-norm	0.1(D <sup>a</sup> )	0.4(D)	0.2(D)	1.4
SALSA	0.9	0.7	1.2	2.1
ASALSA-CF	1.2	1.4	2.4	3.7

D<sup>a</sup>: Distorted

The reconstruction results pertaining to the tissue-mimicking agar phantom containing background optical absorption and scattering are shown in Fig. 6.4. Optoacoustic signals from 128 detector positions over 180 degrees are used for reconstruction. The light

absorption takes place throughout the phantom, resulting in reflected waves (due to mismatch between air and tissue mimicking agar), thus more reconstruction artifacts are produced. The L2-norm and ASALSA results contain obvious artifacts (white arrows). However, CF weighting method removes background artifacts and the two absorbing areas are recovered with higher contrast compared to other reconstruction approaches.

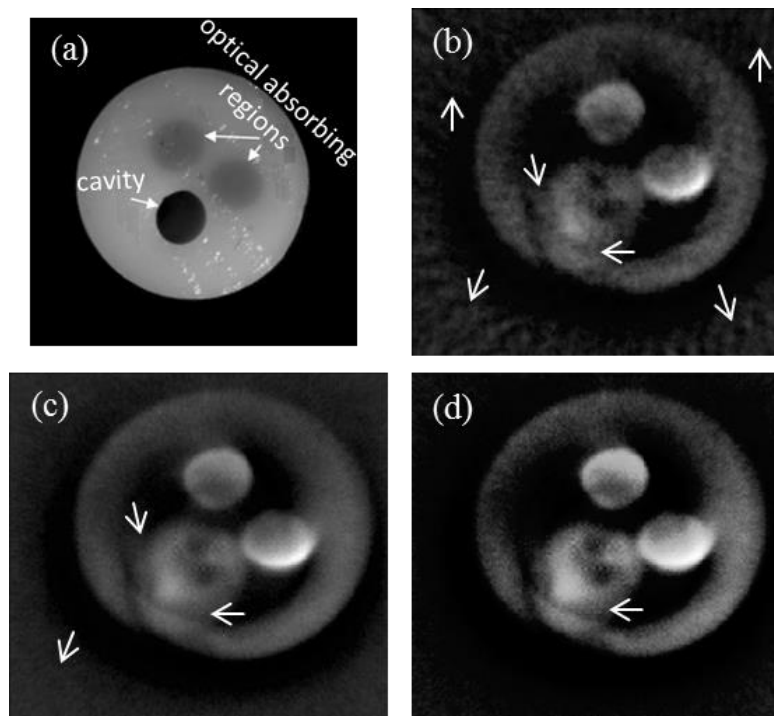


Fig. 6.4. Reconstructed images of the tissue-mimicking agar phantom, which includes hollow cavity filled with air and two high absorbing areas. (a) Reference image of the phantom. (b) Reconstructed image by L2-norm. (c) ASALSA method and (d) the proposed method. Arrows indicate artifacts caused by reflections or scattering of the acoustic waves, which are significantly reduced with the proposed method.

The results pertaining to the *ex vivo* kidney experiment reconstructed from 256 elements over 270 degrees are presented in Fig. 6.5. Fig. 6.5(a) and (b) shows images obtained with the L2-norm and ASALSA method. In analogy to the paper phantom, these two images display similar image quality. However, the CF method further improves the reconstruction performance of the SALSA scheme, as illustrated in Fig. 6.5(c) showing improved reconstruction quality. Specifically, blood vessel structures marked with the box indicated on Fig. 6.5(a) are better distinguishable and less blurry with the ASALSA-CF approach compared to other scheme (insets of Figs. 6.5(a-c)). The visual evaluation is further

corroborated by the line profile drawn over a given image segment [indicated by the dash line in Fig. 6.5(a)], which indicates that blood vessels marked by the red line are better resolved in the ASALSA-CF reconstructions.

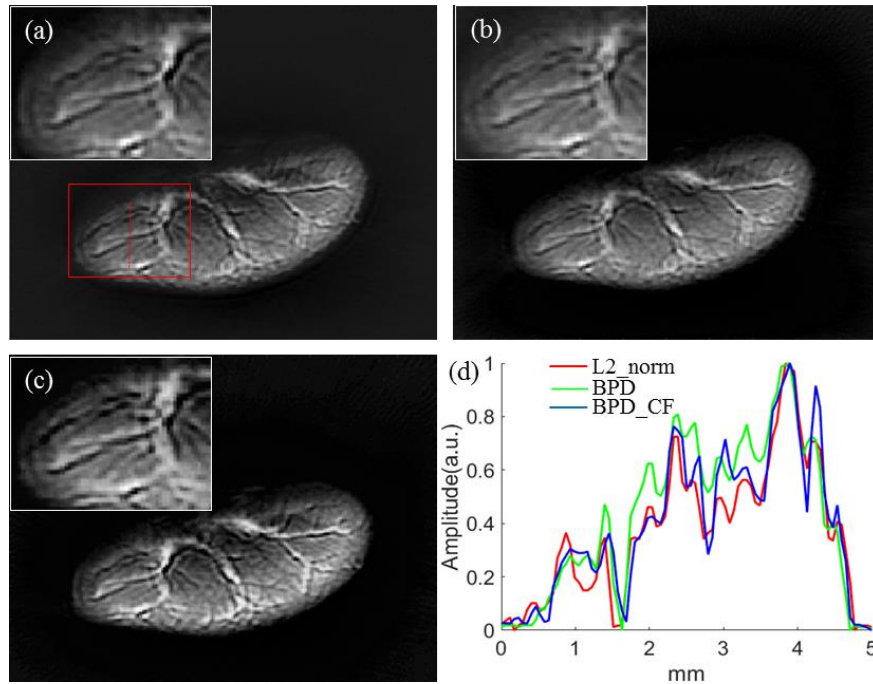


Fig. 6.5. Reconstructed images of the mouse kidney from 256 transducer positions over 270 degrees. (a) The reconstructed image by L2-norm. (b) ASALSA method and (c) the proposed method. The subjects in (a-c) are the zoom-in of region marked in red rectangle of Fig. 5(a) respectively. The line profiles marked by the red line in panel (a) are represented in (d).

The results for the *ex vivo* kidney data reconstructed from 128 elements over 135 degrees are presented in Fig. 6.6. Fig. 6.6(a) and (b) show images obtained with the L2-norm and ASALSA method respectively. It can be seen that the ASALSA method is able to reconstruction more details, while producing more artifacts than the L2-norm based scheme. The reconstruction result [Fig. 6.6(c)] obtained by the proposed method significantly reduces artifacts. Insets in Figs. 6.6(a-c) marked by the red box and the line profile clearly show that the vessel structures are better distinguishable and have higher contrast in the ASALSA-CF image than in the images obtained with other methods.

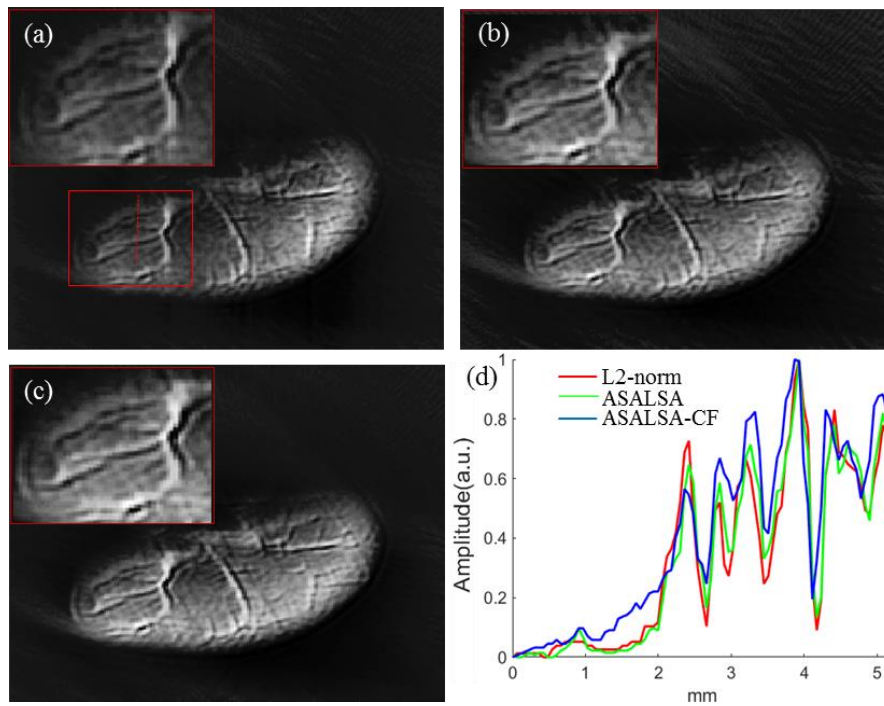


Fig. 6.6. Reconstructed images of the mouse kidney from 128 signal positions over 135 degrees. (a) The reconstructed image by L2-norm. (b) ASALSA method and (c) the proposed method. The subjects in (a-c) are the zoom-in of region marked in red rectangle of (a) respectively. The line profiles marked by the red line in panel (a) are represented in (d).

The comparison of different reconstruction schemes with respect to the computational time and memory requirements is presented in Table-III. We calculated the reconstruction time and memory usage for Fig. 6.5 and Fig. 6.6 using a normal PC (Intel Core i5-3470 @2.3GHz and 16 GB memory). It can be seen from Table-II that the proposed method takes more time and memory compared to the L2-norm approach. However, the conventional SALSA method cannot reconstruct the 256 signals because of computer memory limitation. For 128 signals, the original SALSA method is over 20 times slower and takes 7 times more memory compared to the proposed method.

TABLE III  
COMPUTATION TIME(S) AND MEMORY (GB)

Methods	FIG.7.5	FIG.7.6
L2-norm	79/2.5	35/1.3
SALSA	Out of memory	3554/14.7
ASALSA_CF	294/4.7	137/2.2

### Discussion

In this work, we proposed a fast sparse recovery method along with coherence factor weighting for optoacoustic tomographic image reconstruction. The interpolated model matrix method employs a sparse matrix; hence it is beneficial to utilize mathematical tools pertaining to sparse algebra. Therefore the original Basis Pursuit (solved using Augmented Lagrangian method) is rewritten using iterative Krylov subspace solvers (LSQR inversion), which tends to converge in fewer iterations. It has been proved that the accelerated SALSA approach can save enormous memory and significantly accelerate the computation time compared to the original SALSA approach.

Previous work utilized the SALSA algorithm in the deconvolution framework to remove the blurring caused by the regularization parameter[113]. In this work, we directly used the SALSA algorithm for performing the image reconstruction and hence avoiding the two-step procedure. Further many L1-norm based algorithms are present in the literature namely, two-step iterative shrinkage thresholding, fast iterative shrinkage thresholding algorithm (FISTA), optimization based on majorization-minimization, and greedy algorithms like orthogonal matching pursuit etc. SALSA is known as the fastest converging algorithm among all these family. Hence in this work, the SALSA algorithm has been applied and rewritten with LSQR inversion, foreseeing its utility for real-time implementation.

Table-III also shows that the proposed scheme is slower compared to the traditional L2-norm based approach by about 4 times. The reason is that the ASALSA based approach needs two iterative inversion (LSQR) operations (as shown in Table I). In terms of the order of computation, the ASALSA approach is  $O(4(M+N)N)$  while L2 based reconstruction is

$O(2(M+N)N)$ , where  $M$  is the number of measurements and  $N$  is the number of pixels to be reconstructed. This drawback can be overcome by the using of GPU to accelerate the reconstruction procedure.

We further hypothesized that the application of a weighting coherence factor will reduce the noise and artifacts arising during sparsity based reconstruction, since noise and artifacts are incoherent and optoacoustic signals are coherent. This hypothesis was motivated by the CF use in ultrasound imaging for similar reasons [108, 109]. CF weighting was integrated into the SALSA algorithm for reducing artifacts arising in limited-view cases. On the other hand, artifacts also arise due to acoustically reflecting materials like bone and air, previous works have reduced these artifacts by using coherence factor weighting [108, 109]. From Fig. 6.4, it is evident that coherence factor weighting clearly reduces artifacts arising due to acoustic mismatches. In the resolution phantom measurements, undersampled limited data and limited view scenarios were retrospectively studied, and was observed that ASALSA method outperformed the L2-norm based method in reconstructing the line features. The CF method further helps reducing artifacts and improving resolution and contrast. However, the distorted line feature (label 1) in Fig. 6.1 suggests that the CF method may underestimate the image intensity when SNR is low. This can be improved by using the SNR-based CF calculation method [108]. In analogy to the phantom measurements, reconstruction results of the mouse kidney data also proves that the proposed method can better recover vessel structure compared to conventional methods. Overall, the implication of the proposed reconstruction method could be in its utility for limited view datasets compared to conventional model-based methods and much faster reconstruction than original sparse methods.

## 6.2 Geometric pixel super-resolution approach

The spatial resolution of optoacoustic imaging is limited by the properties of the ultrasound transducer(s) used to collect the signals as well as by acoustic propagation parameters [57]. Indeed, the system configuration and the reconstruction algorithm employed are key factors to determine the final resolution recovered from an OA acquisition [57, 59]. The ideal reconstruction procedure is usually based on several assumptions: (1) wideband detection, (2) point detector measurement, (3) impulse excitation, (4) homogeneous speed of sound, (5)

full-angle detection view and (6) continuous sampling. However, most of these assumptions are not realistic in practical implementations. For example, actual ultrasound sensors have a finite sensing aperture and detection bandwidth [57], which limit the frequency content of the detected signals and hence the spatial resolution achieved [57, 59]. Phase aberrations caused by speed of sound variations and signal broadening associated to acoustic attenuation [62, 63, 114] also degrade the spatial resolution of the images rendered by assuming a uniform acoustic medium. Finally, the detection surfaces are generally finite and partially closed, so that the optoacoustic signals cannot be collected from all directions [65]. Under these circumstances, the achievable spatial resolution is usually lower than that predicted theoretically.

Hardware improvements by means of increasing the detector density have demonstrated improvements in spatial resolution and overall image fidelity [111]. Further improvements have been showcased through reconstruction methods that account for the detection properties of the measurement system and signal distortions due to the propagation medium [57, 61, 62, 67, 115-119]. Nevertheless, accurate modeling in actual biological tissues is generally very challenging and advanced algorithms are computationally expensive.

An alternative approach to improve the contrast and spatial resolution of an image is by integrating information from several low resolution (LR) images obtained at different imaging positions to generate a high resolution (HR) image [120-122]. Termed super-resolution [121], this imaging method relates to a class of ‘pixel super resolution’ algorithms that are employed in digital imaging and lens-less microscopy, to overcome resolution limitations due to pixel size. This approach does not relate to super-resolution methods aiming at breaking the diffraction limit of light and/ or ultrasound [123]. To differentiate these two classes of “super resolution” methods we refer to the method employed in digital imaging as pixel super resolution (PSR) herein. PSR methods were first introduced in digital image processing [124] and have been adapted to biomedical imaging modalities such as x-ray CT, MRI and PET [121, 124-128]. PSR methods have been successfully applied to MRI for resolution and image quality enhancement without increasing the acquisition time or changing the imaging system [127, 129, 130]. For example, Kennedy et. al. [19] demonstrated the application of iterative PSR algorithms in improving resolution of clinical

PET imaging by multiple datasets with spatial shifts between consecutive acquisitions. The PSR method suggested herein is specifically implemented the scanning protocols of a small animal multispectral optoacoustic tomography scanner, and is termed PSR-MSOT.

In this section, we consider the PSR implementation in optoacoustic imaging and aimed to investigate the possible improvements gained in image resolution and contrast [131]. In particular, we consider the complementary information contained in adjacent images in a PSR formulation. The study involved simulations and experimental measurements on phantoms and ex-vivo murine organs. Further, we discuss implementation possibilities as a compliment to scanning modifications in optoacoustic signals without requiring significant hardware upgrades.

### 6.2.1 Methods and materials

This section describes the implementation of pixel super-resolution for optoacoustic imaging, the simulations performed and details of the experimental parameters employed, including the acquisition protocol using small animal multi-spectral optoacoustic tomography scanner.

#### A. Super-resolution method

The operating principle of PSR techniques relies on composing a high resolution image from a sequence of low resolution images acquired from different imaging perspectives or views [132-134]. The PSR method is generally defined as an inverse process of imaging degradation, where the inversion is regularized due to the ill-posed nature of the problem [132, 133]. Accordingly, the HR image is calculated as follows:

$$\bar{X} = \arg \underset{X}{\text{Min}} \left\{ \sum_{k=1}^N \|Y_k, D_k H_k F_k X\| + \lambda \gamma(X) \right\} \quad (6.12)$$

where  $\{Y_k\}$  represents the k-th LR image, with resolution  $N_1 \times N_2$ , and  $X$  is the HR image estimated from  $\{Y_k\}$ , with resolution  $qN_1 \times qN_2$ , where  $q$  is the sampling scalar.  $D_k$  represents the down sampling operator from the HR to the LR image.  $H_k$  is the blur matrix corresponding to the point spread function (PSF) of the imaging system. It is taken as a delta function with a width of one pixel when the PSF is unknown.  $F_k$  is the geometric motion

operator between the estimated HR frame  $X$  and the  $k$ -th LR frame. Finally,  $\gamma(X)$  is a regularization term,  $\lambda$  being a regularization weighting parameter determined according to the trade-off between edge information and noise. The initial guess for the HR image is taken by interpolating a specific LR image.

Though the spatial transformation for different acquisitions can generally be accurately characterized, the image transformation among reconstructed LR images may not exactly correspond to the defined spatial transformation due to inevitable movement of the imaging setup and target. Thereby, in order to improve the image quality in the PSR process, the image transformation between the estimated HR frame  $X$  and the  $k$ -th LR frame  $Y$  (motion matrix  $F_k$ ) is accurately estimated with a method based on optical flow registration [135]. Then, the solution of Eq. 6.12 corresponding to the HR image  $X$  is calculated iteratively until the solution converges or a pre-defined cut-off value (maximum) of iterations is reached.

The PSR inversion process defined in Eq. 6.12 is an ill-posed process, so that a regularization term is generally required for rendering a stable solution [132]. The regularization term compensates for ill-posedness by a priori imposing additional information on the desirable HR image [124, 132], consequently suppressing artifacts and noise, and improving the rate of convergence. Herein, we employ a bilateral total variation (BTV) regularization term defined as [124, 132]:

$$\gamma(X) = \sum_{l=-P}^P \sum_{m=0}^P \alpha^{|m+l|} \|X - S_x^l S_y^m X\| \quad (6.13)$$

where  $l+m \geq 0$ ,  $S_x^l$  and  $S_y^m$  are shift matrices to present  $l$  and  $m$  pixels shift in horizontal and vertical directions, respectively.  $P(1 \leq P \leq 3)$  is the shifting range in both directions and  $\alpha(0 < \alpha < 1)$  is the weighting coefficient. The scalar weight  $\alpha$  gives a spatially-decaying effect to the regularization terms summation. The BTV regularization is based on the combination of the total variation restoration model and the bilateral filter [124, 132], where total variation anisotropic diffusion is used for image restoration and edge enhancement, and the bilateral filter focuses on noise reduction and edge sharpening [132, 136]. Subsequent application of the bilateral filter several times leads to smoothing of the signal until reaching a steady rate. Based on this, a large value of  $\alpha$  is chosen for images affected by noise, which

suppresses noise and smooth flat regions in the estimated HR image at the expense of losing edge information. More detailed information about the BTV regularization function can be found elsewhere [132, 136]. Combining Eqs. 6.12 and 6.13, the iterative PSR process is calculated with steepest descent method and the final minimization function described as [124, 132]:

$$\begin{aligned} \bar{X}_{n+1} = \bar{X}_n + & \left\{ \sum_{k=1}^N F_k^T H_k^T D_k^Y \bullet \text{sign}(Y_k - D_k H_k F_k \bar{X}_n) + \right. \\ & \left. \lambda \left( \sum_{l=-P}^P \sum_{m=0}^P \alpha^{|m|+|l|} (I - S_x^{-l} S_y^{-m}) \bullet \text{sign}(\bar{X}_n - S_x^l S_y^m \bar{X}_n) \right) \right\} \end{aligned} \quad (6.14)$$

where  $S_x^{-l}$  and  $S_y^{-m}$  represent the transposes of matrices  $S_x^l$  and  $S_y^m$  respectively and they have a shifting effect in the opposite directions as  $S_x^l$  and  $S_y^m$ .

### B. Implementation in optoacoustic tomography

In order to test the experimental performance of the PSR method in optoacoustic tomography, experiments were conducted using a small animal multispectral optoacoustic tomography scanner (MSOT256-TF, iThera Medical GmbH, Munich, Germany). The scanner utilized cross-sectional optoacoustic acquisition geometry (see Fig. 6.7) consisting of a custom-made 256-element array of cylindrically-focused piezocomposite transducers. The array covered an angle of approximately  $270^\circ$  and had a radius of curvature of 40 mm, allowing simultaneous acquisition of the signals generated with each laser pulse. The central frequency of the array elements was 5 MHz, and the -6 dB bandwidth was approximately 90%. Light excitation was provided from a wavelength-tunable optical parametric OPO laser and delivered by fiber bundles shaped to attain ring-type uniform illumination on the surface of the sample. The detected optoacoustic signals were simultaneously digitized at 40 megasamples per second. The signals were averaged 10 times for an improved SNR performance. The resolution of the system depended on the frequency response and the geometrical properties of the detector array, and was estimated as  $\sim 150 \mu\text{m}$  in the cross-sectional plane and  $\sim 800 \mu\text{m}$  in the normal direction. More detail information about the imaging setup can be found elsewhere [5, 110, 111].

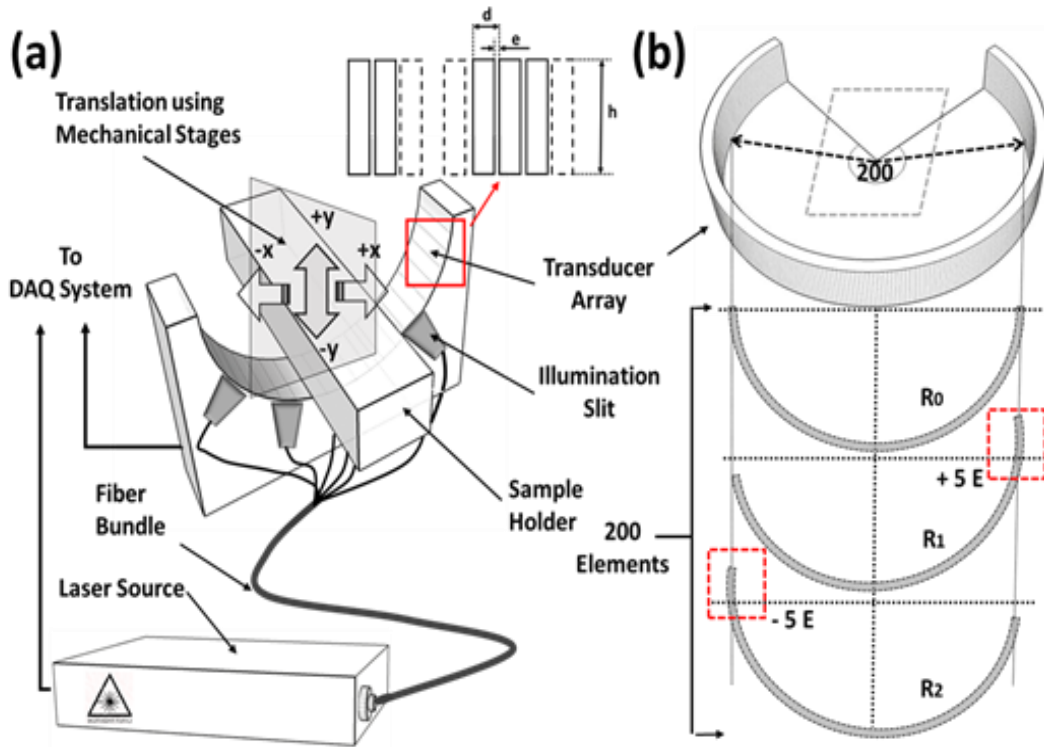


Fig. 6.7. Schematic of the MSOT256 System with the detector and laser arrangement, the sample holder is connected to mechanical stages for translation of the sample. The configuration of the detector arrays is shown in the zoom-in, the system comprises of 256 cylindrically focused individual detector elements. (a) Translational (X and Y directions in a single Z plane) and (b) transaxial scanning modes. The sample is translated four positions (in X and Y) in the translational mode and detectors are virtually rotated for three configurations ( $R_0 - R_2$ ) in the transaxial mode to acquire the data stack for super-resolution image formation.

The MSOT system integrated high-precision stages able to translate the scanning sample in steps of 0.1 mm. The PSR algorithm was first implemented in the translation mode by combining sets of four low resolution images acquired in four translation scanning positions (Fig. 6.7). Specifically, the sample was scanned to the positions  $(x+\Delta x, y)$ ,  $(x, y+\Delta y)$ ,  $(x-\Delta x, y)$ ,  $(x, y-\Delta y)$ , being  $\Delta x=\Delta y=0.3$  mm, for a given (fixed) z-plane. In addition, the PSR algorithm was also implemented in a “transaxial mode”, which combined translation and rotation. The transaxial mode acquired three LR images for each translational position using virtual rotations  $(\phi\pm\Delta\phi)$ , where  $\Delta\phi$  corresponded to the angular separation of 5 consecutive elements of the array in the transverse plane between successive acquisitions. In the translation mode, the geometric transformation at different imaging views was applied precisely and all transducer elements (256 elements) were considered for all reconstructions.

Only 200 transducer elements were used for the reconstructions in the transaxial mode, and the virtual rotation was simulated by selecting the transducer elements considered. Because the MSOT transducer array is toroidally focused, the best quality image is generally obtained with the sample located on the focus area of the detector. For a fair comparison, the best quality cross-sectional reconstruction was determined by visual inspection and was chosen as the reference image for the PSR process, where the signals of 200 channels in the central area of the detector were used for reconstruction in the transaxial mode.

### C. Simulations and experimental measurements

Numerical simulations were first performed to test the performance of the suggested method. For this, a resolution target phantom was used to define the theoretical initial optoacoustic pressure distribution [Fig. 6.8(a)]. The simulations were executed using MATLAB (The MathWorks, Inc.) k-Wave Toolbox [63, 115]. The signals at 200 points located at a distance of 25 mm from the center of the phantom and equally-spaced along an arc of  $180^\circ$  were considered. A simulated Gaussian shape impulse response with a full-width at half maximum (FWHM) of 100 ns was convolved with the simulated optoacoustic signals to mimic the effects of the frequency response of the transducer, which degraded the spatial resolution to  $150 \times 150 \mu\text{m}$ . The phantom was shifted linearly with a step-size of  $300 \mu\text{m}$  according to the translation mode described earlier, so as to obtain four optoacoustic images with different imaging views.

An equivalent experiment was subsequently performed to validate the simulation results and characterize the resolution improvement achieved with the PSR method in practical cases. For this, a printed paper (USAF resolution target, standard inkjet printer with black ink) phantom embedded in a 1.9 cm diameter diffuse agar cylinder (6% by volume Intralipid in the agar solution) was measured. The structure of the phantom is shown in Fig. 6.9(a). The image object includes several groups of elements of different size, which can be used for resolution characterization at different levels. Four optoacoustic images of the resolution target phantom were obtained in the translation mode and twelve optoacoustic images were acquired in the transaxial mode.

Further trials on an ex-vivo murine kidney were conducted to test the applicability of the method in biological tissue. The kidney was extracted post-mortem (non-perfused) according to institutional regulations regarding animal handling protocols and subsequently embedded in a diffuse agar block (6% by volume Intralipid in the agar solution) for ensuring uniform illumination of the sample. After completion of OA imaging experiments, the sample was isolated and frozen at  $-51^{\circ}\text{C}$  for 24 hours. It was thereafter embedded in a water soluble optimal cutting temperature compound and cryosectioned with sample thickness of  $20\ \mu\text{m}$  at a temperature of  $-20^{\circ}\text{C}$ . The RGB images of the cryosections were used as a reference to validate the reconstruction and PSR results by correlating the location, orientation and morphology of the blood vessels within the kidney mass.

The optoacoustic images for all scanning positions were reconstructed with a standard filtered back-projection algorithm [57]. Prior to reconstruction, the OA signals were band-pass filtered with cut-off frequencies between 0.2 and 7 MHz in order to remove low frequency off-sets and high frequency noise. A uniform speed of sound (SoS) of 1510 m/s was used for each reconstruction. Indeed, even if the SoS variations from one medium to another can cause of distortions in the OA images, using a constant SoS value generally allows obtaining a representative image [112, 114]. Thereby, the values of SoS were optimally chosen for each image by using iterative autofocus metrics. A model-based (MB) reconstruction method employing similar regularization as the PSR method was used as a reference (shown in Fig. 11) for comparison of the proposed method vis-à-vis advanced reconstruction methodologies [8].

All LR images were mathematically registered to the reference image for calculation of the image transformation. For comparison, the transformation information between the reference image and each LR images were interpolated into the reference image to obtain the so-called interleaving image. The interleaving image corresponds to a two times up-sampled LR image with the same size as the PSR image. For the translation or transaxial mode, the image obtained at the focus area was taken as the initial guess for the HR image. The transformation matrix was calculated between the guessed HR image and LR images obtained in other positions. In each iteration of the PSR inversion problem, the reference image was updated with the interleaving image, and the motion between the LR images and the updated

reference image was then calculated. The PSR procedure was iteratively updated according to Eq. 6.14 until the difference error was less than 0.02 or after 12 interactions.  $\lambda$  was taken as 0.02 for all data, while  $\alpha$  was taken as 0.01 for the simulated LR images and, was increased to 0.05 for smoothing noise of the reconstructed PSR images in the USAF and mouse tissue experiments. The initial reference images shown in the results section were reconstructed with the FBP algorithm considering the same pixel number and width as the PSR image.

In order to compare the image contrast of the resolution target phantom, the average intensity (S) of the resolution lines were calculated, as well as the standard deviation of background (B) signals in the spaces between the lines. The region of interest for calculating for resolution line was established by digitally masking the image with the known location of the target lines. The ratio of the average signal to the standard deviation of background noise provided a contrast ratio  $CNR = 20 * \log(S/B)$ .

### 6.2.2 Results

The results of the numerical simulation are depicted in Fig. 6.8. Fig. 6.8(a) shows the optical absorption distribution used for the forward simulation, which represents a resolution target phantom typically used as a characterization tool in optical imaging. Fig. 6.8(b) shows the LR OA image reconstructed by using the FBP algorithm by considering a pixel size of  $100 \mu\text{m}$  ( $200 \times 100 \text{ pixels}^2$ ) whereas Fig. 6.8(c) presents the HR image obtained by interpolation from the reference image in Fig. 6.8(b). Fig. 6.8(d) displays the HR image obtained by interleaving the LR reconstructions obtained with 4 scanned slices translated in the same plane. The HR image obtained with the PSR method from the same 4 slices is shown in Fig. 6.8(e). From the zoomed in areas shown in Fig. 6.8(f-i) and from the line profiles shown in Fig. 6.8(j-k), we see that the proposed PSR method significantly improves the image resolution.

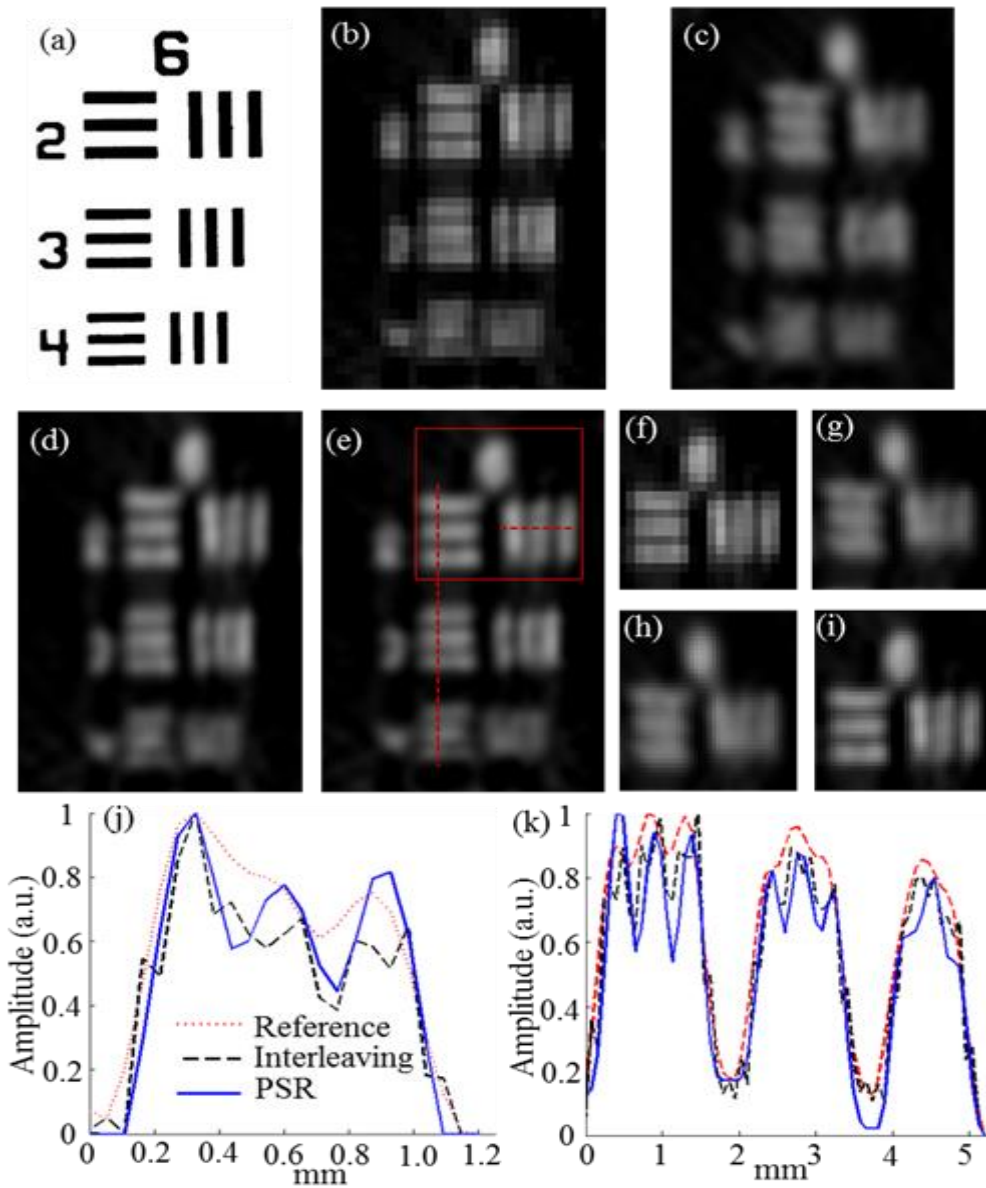


Fig. 6.8. Simulation of PSR algorithm. (a) Reference USAF phantom. (b) Low resolution (LR) reconstructed image. 4 LR images with 3pixels shifts were used to obtain a higher resolution image using (c) Interpolation, (d) interleaving and (e) PSR. The figures (f-i) are the zoom-in of the region marked in red in for panels (b-e) respectively. The line profiles in the horizontal and vertical directions marked in panel (e) are represented in (j) and (k) respectively for the interpolation (red), interleaving and PSR (blue) methods.

The experimental results corresponding to the two-dimensional USAF target paper phantom imaged in the translational mode are given in Fig. 6.9. Fig. 6.9(a) displays a photograph of the printed structure. The LR optoacoustic images are reconstructed with the FBP algorithm by considering a pixel size of  $62.5 \mu\text{m}$  ( $200 \times 200 \text{ pixels}^2$ ) and the reference image

---

(reconstructed with same pixel number and width as the PSR image) is shown in Fig. 6.9(b). The image obtained by interleaving 4 translational scans is shown in Fig. 6.9(c). The PSR image reconstructed from the same 4 positions is shown in Fig. 6.9(d). Much like in the simulations, the PSR image has higher resolution and quality as observed in the zoomed areas in Fig. 6.9(e-g) and in the line profiles in Fig. 6.9(h-i) comparing to other approaches. Specifically, line features in Fig. 6.9(e) are seriously distorted (e.g. labels 3, 4 and 8) and discontinuities (e.g. labels 1, 6 and 7) can be observed. The line features in the interleaving image [Fig. 6.9(c)] are also distorted and noisy. On the other hand, the lateral (e.g. labels 3 and 4) and axial (e.g. labels 7 and 8) resolution characterization lines are more distinguishable in the PSR image. The lateral and axial line profiles marked by the red arrows in Fig. 6.9(d) also suggest a better resolution in the PSR image. The comparison of contrast-to-noise ratio (CNR) achieved with the different methods is showcased in Table IV. The PSR image provides a CNR more than 50% higher than the reference image and 50% higher than the interleaving image (Table IV).

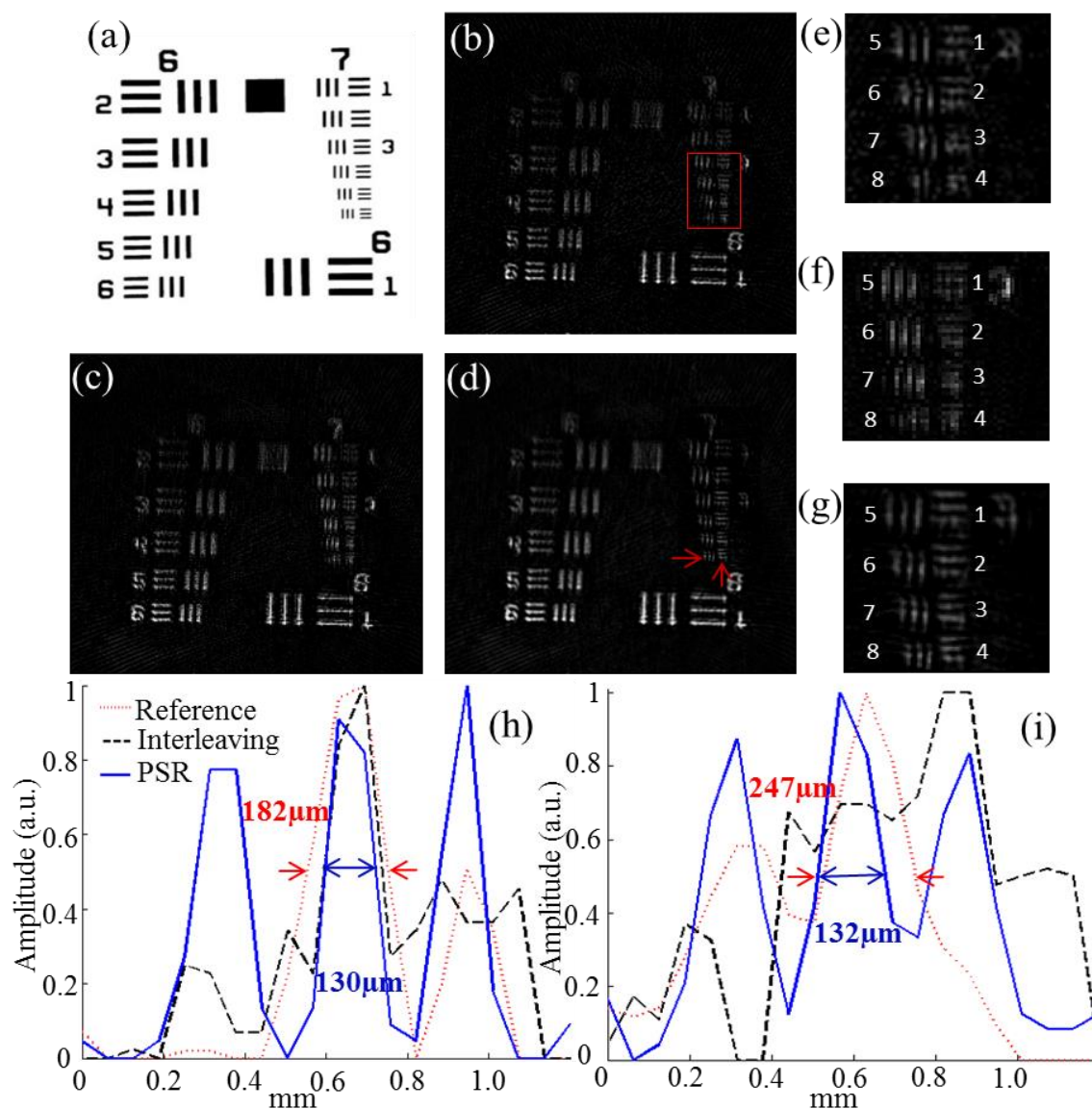


Fig. 6.9. (a) Reference USAF phantom printed on white paper with black ink, which was embedded in scattering agar. (b) Reconstructed high resolution reference image. Low resolution (LR) images were reconstructed using back projection, 4 LR images with 0.3mm shifts in linear direction were used to obtain a higher resolution image using (c) interleaving and (d) PSR. The figures (e-g) are the zoom-in of region marked in red in panel b for the panels (b-d) respectively. The line profiles in the horizontal and vertical directions marked in panel (d) are represented in (h) and (i) respectively for the high-resolution reference image (red), the interleaving image (black) and the super-resolution image (blue).

TABLE IV  
CONTRAST RATION CNR FOR OPTOACOUSTIC IMAGES IN TRANSLATION MODE

Image Type	LINE 1	LINE 2	LINE3	LINE 4
Reference Image	2.1(D <sup>a</sup> )	1.2(D)	1.9(D)	1.1(D)
Interleaving Image	1.8	0.5	1.7	0.6
PSR Image	3.2	3.8	2.8	1.9

D<sup>a</sup>: Distorted

Fig. 6.10 shows the results of the USAF phantom experiment imaged in the transaxial mode by considering different numbers of LR images. The images obtained with the interleaving and PSR methods considering 1 transaxial scanning positions (3 images) are shown in Fig. 6.10(a) and (c). The corresponding results obtained using 3 transaxial positions (9 images) are displayed in Fig. 6.10(b) and (d). The image in Fig. 6.9(b) is also considered as a reference. Targets in the PSR results are better resolved comparing to the reference and interleaving images. Comparing the horizontal (labeled 1, 2, 3, and 4) and vertical (labeled 5, 6, 7 and 8) resolution characterization lines in Fig. 6.10(c) and (d), it is observed that increasing the number of LR images also leads to a better resolution of the PSR images. Fig. 6.10(e) and (f) shows the relationship between the CNR (labels 4 and 6) and the number of LR slices used in PSR method. It is shown that increasing the number of LR images for PSR reconstruction generally leads to an increase in the CNR. However, the CNR may decrease because more noise is accumulated with the number of LR slices increasing in the PSR process; the same is clearly demonstrated in Fig. 6.10(e-f) where the CNR value is decreased when more than 9 LR images were used.

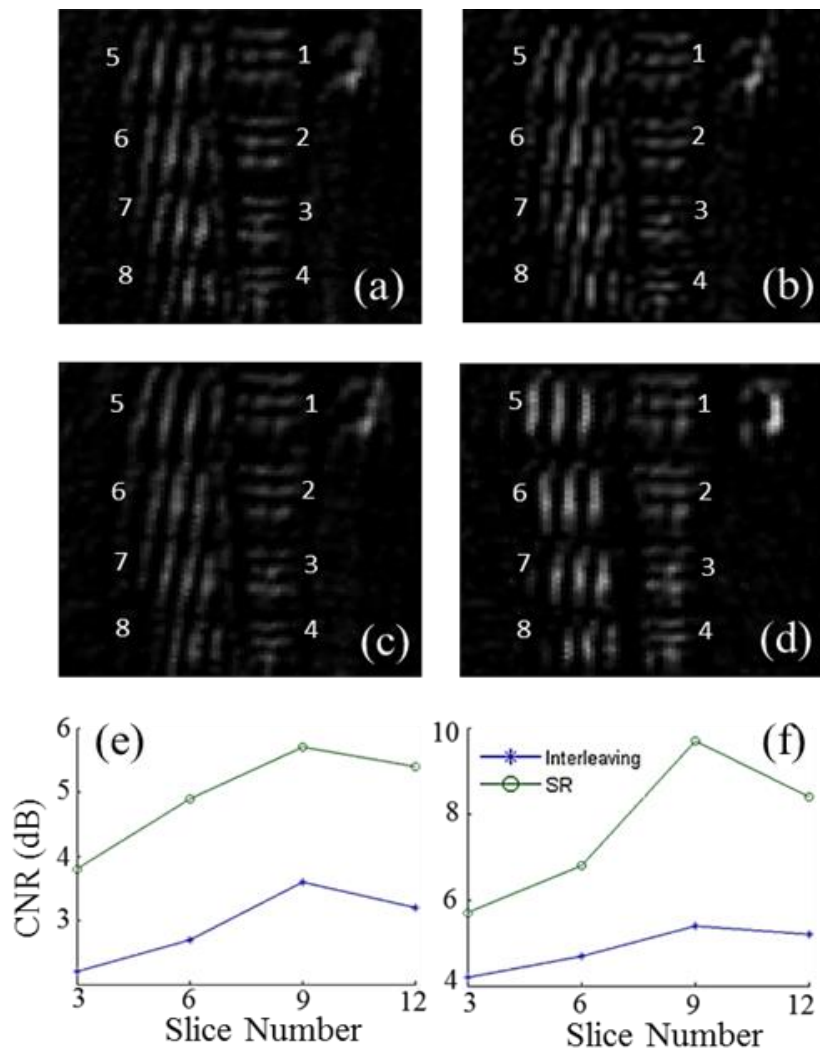


Fig. 6.10. Low resolution (LR) images were reconstructed using back projection with 0.3mm shifts in the linear direction (translational) and 5 element shifts (rotational). Higher resolution image reconstructed using (a) interleaving 3 images (1 transaxial position), (b) Interleaving with 9 images (3 transaxial positions), (c) PSR with 3 images (rotation) and (d) PSR with 9 images (rotation + translation). The plots in (e) and (f) show the relationship between the number of slices and CNR for areas 4 and 6 respectively.

The results for the *ex-vivo* kidney experiment are presented in Fig. 6.11. A photograph of a cryoslice obtained through the imaging position is shown in Fig. 6.11(a). Fig. 6.11(b) and (c) show reference images obtained with the FBP and MB algorithms by considering 400x400 pixels with pixel width 50 $\mu$ m. The interleaving result [Fig. 6.11(d)] obtained by directly registering information from different scanning views reconstructed with FBP shows similar image fidelity to the reference image. In contrast, the PSR image considering 6 slices

reconstructed with FBP in the transaxial mode displayed in Fig. 6.11(e) demonstrates improvements on image quality. Specifically, blood vessel structures marked with the box indicated on Fig. 6.11(a) are better resolved in the PSR image than in the images obtained with other methods, as shown by inserts in Figs. 6.11(b-e). The vascular structures [as indicated by arrows in the inserts in Figs. 6.11(b-e)] in the PSR image show better structural integrity and conformity when compared to the reference images and the interleaving image. The visual evaluation is further corroborated by the line profile drawn over a given image segment [indicated by the dash line in Fig. 6.11(b)], which indicates that blood vessels are better resolved in the PSR image. In addition, the PSR image has significantly less streak-type artefacts as compared to the other images, so that the background noise is reduced.

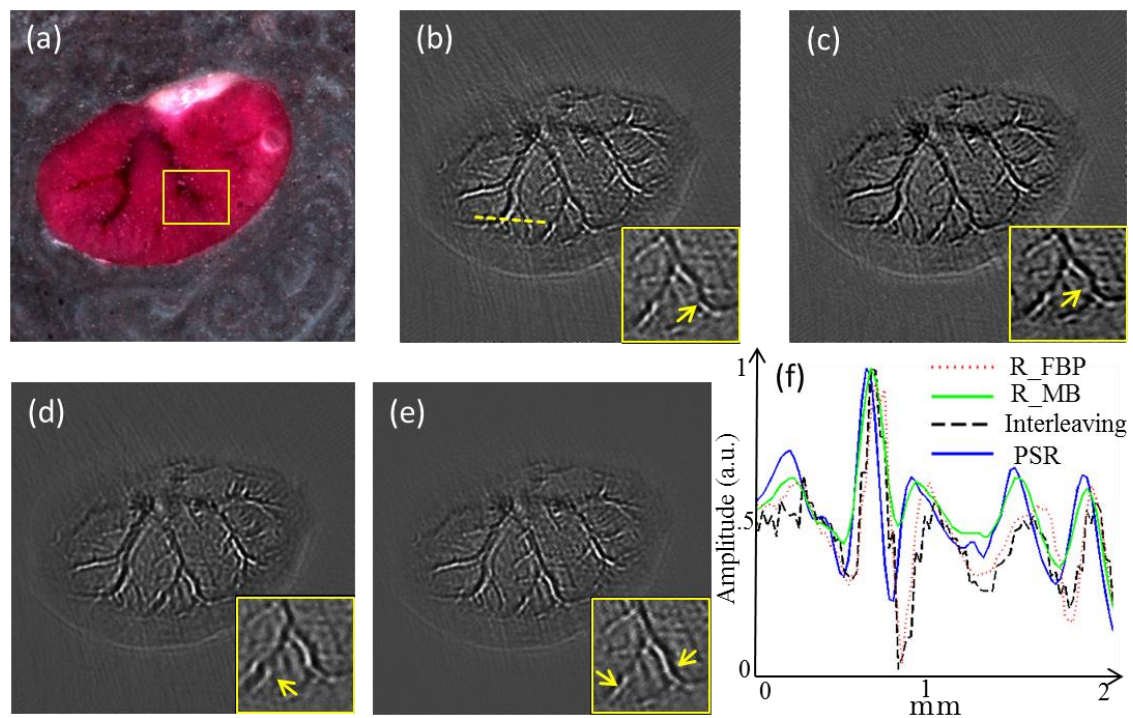


Fig. 6.11. Reconstruction results for the ex-vivo murine kidney. (a) Reference cryoslice image. (b) Reconstructed high-resolution reference image with the FBP method. (c) Reconstructed high-resolution reference image with the MB method. (d) Interleaving result with 6 images obtained in the transaxial mode. (e) PSR image. The line profile marked on (b) is shown in (f). Zoom in of the region marked in panel (a) is provided for better visualization of the microvasculature and image enhancement achieved by different methods.

**Discussion**

The section described a novel geometrical pixel super-resolution method achieved using image processing techniques, and implemented for state of the art optoacoustic tomographic imaging. The proposed PSR method made use of multiple post-reconstruction optoacoustic images with geometrical proximity to efficiently integrate the information into a high-resolution image. The performance of the suggested method for enhancing image resolution and contrast was showcased in cross-sectional optoacoustic imaging. However, the method can easily be extended to a wide range of optoacoustic imaging systems by properly defining and customizing the scanning protocol for individual systems. In this way, simple geometrical manipulation can generally lead to an enhancement in optoacoustic contrast and resolution, thus overcome limitations of the system hardware and reconstruction methods.

The simulations and experiments conducted with a USAF resolution target phantom demonstrated that the image resolution in both the lateral and axial directions improved with the PSR method suggested in this work. For instance, the resolution characterized as FWHM along the lateral direction of the line target was improved from 180  $\mu\text{m}$  in the reference image to 130  $\mu\text{m}$  in the PSR image, and the FWHM value along the axial direction was improved from 247  $\mu\text{m}$  to 132  $\mu\text{m}$  respectively. Small target resolution line features were better resolved, while they were distorted and blurred in the reference image obtained for a single imaging position and in the interleaving image retrieved by considering several positions. The image quality of larger line targets was also enhanced with the PSR method, and an improvement of CNR can be observed. Thereby, the PSR method reduced distortion of line features and enhanced image contrast at different resolution scales.

Furthermore, it was shown that increasing the number of low-resolution images obtained along different imaging views improved the image quality of the super-resolution result. It should be noted that increasing the number of low-resolution images in the super-resolution process may result in integration of reconstruction errors and noise in the resulting super-resolution image, especially when the image quality of the low-resolution images is low. For the noisy images, the regularization parameters can be optimized to smooth the noise. However, this could lead to blurring in the resulting super-resolution image. Also, the number

of scanning positions for a specific optoacoustic system may be limited. Therefore, the optimum number of low-resolution images to consider for the super-resolution method must be determined according to the achievable image quality enhancement and the practicability in different imaging setups. On the other hand, the experiments on an ex-vivo mouse kidney illustrate the potential of the super-resolution method suggested herein for improving the image quality of vascular structures in real biological tissues.

Although PSR improvements in image quality come at an incremental computation overhead, the method can potentially improve imaging accuracy by acquiring multiple low-resolution images and combining them algorithmically on a software platform, instead of having a slower high-resolution acquisition achieved through averaging the signal data over multiple cycles (typically 10 frames). The processing time grows with the number of low-resolution images used in the PSR process, both in terms of signal acquisition time as well as in image reconstruction and processing. Thereby, a trade-off between optoacoustic image quality and image formation speed generally exists. This is particularly significant during in vivo measurements where the system dynamics can vary within a very short time window. Numerically, the total time for reconstructing 4 LR images and subsequent processing with the PSR method for  $400 \times 400$  pixels<sup>2</sup> is about 4/3 of the reconstructing time of the HR reference image, which has half pixel width (total pixel resolution is doubled) of the low-resolution image. Also, the computation time of the MB reconstruction in Fig. 6.11(c) is five times slower than the total execution time of PSR process. The image reconstructions and super-resolution processing can be further accelerated by paralleled computing with GPU, which can potentially improve the applicability of the PSR method illustrated herein.

There are limitations in PSR-MSOT implementation that should be addressed towards performance optimization. We acknowledge that the suggested PSR method is sensitive to the noise level of the low-resolution images. However, suitable regularization can be employed for noise suppression to achieve a high-resolution image. The noise level also affects the registration accuracy in the super-resolution process, which diminishes the resolution. Thereby, improvements in the optoacoustic reconstruction and pre-processing methods can potentially lead to removing noise and artifacts in the final images. Furthermore, the accuracy of registration methods significantly affects the image quality of PSR-MSOT

imaging. For ex-vivo data, fast linear motion estimation method can be performed in the PSR process. However, the method can be significantly challenging in applications in vivo due to cardiac or respiratory motion. In this case, advanced registration methods, such as nonlinear subpixel registration method [135], may be applicable for estimating the motion between different images. As a part of future work, we aim to investigate on different motion correction methods for in-vivo PSR-MSOT imaging.

Overall, the successful application of super-resolution techniques in optoacoustic imaging as demonstrated in this work suggests the general applicability of this methodology to increase optoacoustic resolution and image quality. The demonstrated enhancement of resolution and contrast in experiments with tissue-mimicking phantoms and actual biological tissues showcase that super-resolution may offer as a useful tool for clinical practice and biomedical research wherein a higher imaging resolution without significant hardware upgrades can be achieved.

## Chapter 7      **Optoacoustic imaging of esophageal tissue**

Several optoacoustic endoscopy implementations and in vivo measurements of rat or rabbit esophageal tracts have been reported [52, 53]. Vessel structures inside the esophagus wall and surrounding tissue of rat or rabbit are nicely resolved [52, 53]. However, there are few studies concerning optoacoustic properties of esophageal wall from human or large animals. Investigating the imaging performance of excised samples is a very important step to prove the clinical relevance of optoacoustic imaging on gastrointestinal diseases. Therefore, esophagus samples of pigs and human are measured with high resolution optoacoustic mesoscopy system and results are further analyzed in this chapter. Section 7.1 introduces the clinical interests of esophagus imaging. Excised esophagus (pig and human) measurements conducted by mesoscopy system are described in section 7.2. Results are studied to investigate the optimal laser wavelength and detection bandwidth of ultrasound transducers for esophagus imaging. Besides, a frequency spectra analysis method is developed to analyze the relation between the frequency characteristics of optoacoustic images and the anatomical structure of esophagus wall in section 7.3. The developed endoscopy system is validated on esophageal samples and corresponding results are introduced in section 7.4.

### **7.1 Clinical interests of esophagus imaging**

Esophagus cancer is the seventh leading cause of cancer-related deaths worldwide with an increasing incidence rate over the last three decades [14]. Overall 5-year survival rate for patients with esophageal cancer is still poor [14]. Staging of esophageal cancer is a standard way for doctors to sum up how far the cancer has spread. The treatment and outlook for people with esophageal cancer depend, to a large extent, on the cancer's stage. The most common system used to stage esophageal cancer is the T stage system of the American Joint Committee on Cancer (AJCC) as illustrated in Fig. 7.1[14, 46]. The T staging classification of esophagus cancer depends mainly on the depth of the infiltration and the extent of damage

to histological layers of esophagus wall [14, 46]. From the lumen outwards, the superficial esophagus wall include several layer structures: namely epithelium (EP), lamina propria, muscularis mucosa (MM), submucosa (SM) and muscularis propria (MP) [96]. Esophageal cancers usually start in the innermost lining of the esophagus (the epithelium layer) and then grow into deeper layers over time [14, 46]. The earlier detection and staging of esophageal tumor are closely related to therapeutic strategy and the survival rate. For example, the T1 stage of esophageal cancer is subdivided into T1a and T1b [97]. In the T1a stage, the tumor only infiltrates into the mucosal lamina propria and muscularis mucosa, while the tumor of the T1b grows into the submucosa. Endoscopic treatments such as endoscopic mucosal resection (EMR) or endoscopic submucosal dissection can be performed for the T1a tumor, because the existing rate of lymph node metastases is extremely low in T1a cases [14, 97]. In contrast, lymph node metastases occur with much higher rate (21%-24%) in the T1b, and these patients are not suitable for endoscopic treatment and require surgical resection. Therefore, obtaining accurate pre-treatment staging and then subsequently providing stage-appropriate treatment is crucial in optimizing esophageal cancer outcomes [14].

Current clinical imaging techniques have limitations on stage earlier esophageal cancer. X-ray CT and PET are normally used to scan the chest and abdomen when esophageal cancer is diagnosed histologically. Besides, X-ray CT and PET are somewhat limited in defining the local extent and nodal involvement of esophageal cancer [14, 19]. Endoscopic ultrasound provides more accurate evaluation of the depth of tumor infiltration than both PET and X-ray CT, while it has low accuracy of staging early-stage cancer as T1 or T2 because of low tissue contrast [43, 137]. In order to accurately stage early esophagus cancer, an imaging modality should have the capability to clearly resolve the layer structures of esophagus wall with a penetration depth up to several millimeters [14, 97]. Herein, we apply optoacoustic imaging to measure excised esophagus samples and investigate the imaging performance of optoacoustic on esophagus wall.

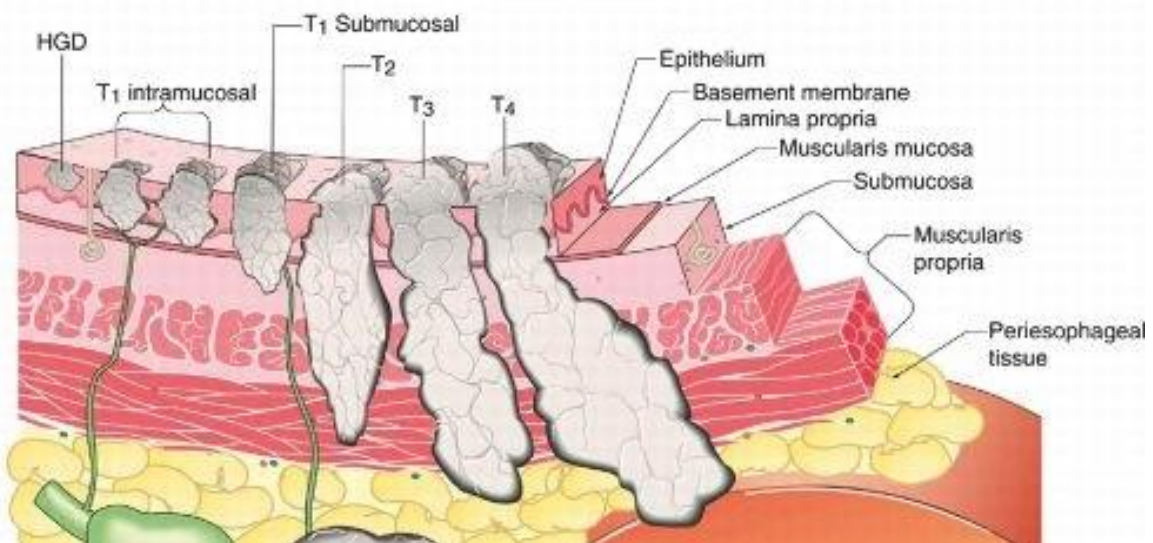


Fig. 7.1. Esophagus cancer staging according to the American Joint Committee on Cancer tumor-node-metastasis (TNM) classification, this figure is from online source (Cleveland Clinics). The anatomical layer structures of the esophagus wall are illustrated. The esophagus cancer is staged from T1 to T4 stages based on the infiltration depth and location of the lesion in the T stage system.

## 7.2 Esophagus sample measurements by Mesoscopy

In order to investigate the optoacoustic properties of esophagus wall, a high resolution optoacoustic mesoscopy system is applied to measure excised esophagus samples from human and pigs. Optoacoustic mesoscopy enables to acquire high resolution images beyond the depth of optical microscopy, up to several millimeters deep in soft tissue [138, 139]. Multi-spectra optoacoustic images are recorded and studied to understand the optoacoustic properties of esophagus samples.

### 7.2.1 Mesoscopy imaging system

A custom-made 50 MHz central frequency spherically focused transducer made of LiNbO<sub>3</sub> is employed in this system to produce wide bandwidth measurements ranging from 10 MHz to 90 MHz. The sensing areas of the transducer have a diameter of 3 mm and an f-number of 0.99. Illumination is provided by a 532 nm laser, with a pulse repetition rate of 2 kHz, energies of 1 mJ/pulse, and pulse widths of 0.9 ns (Wedge HB532, BrightSolutions SRL, Pavia, Italy). The recorded optoacoustic signals are amplified by a low noise amplifier (63

dB, AU-1291, Miteq Inc., Hauppauge, New York, USA) to a high-speed digitizer, operating at 1 GS/s (CS122G1, Gage, Lockport, Illinois, USA; 12 bit resolution; max sampling rate, 2 GS/s). To perform fast raster scan, motorized piezostages are used (M683.2U4, Physik Instrumente GmbH & Co. KG, Karlsruhe, Germany). The image reconstruction of the mesoscopy datasets are implemented by backprojection approach. The highest lateral resolution achieved with this system is 40  $\mu\text{m}$ , whereas the axial resolution reached 15  $\mu\text{m}$  [138]. More detailed information about the imaging system can be found here [138, 139].

### **7.2.2 Pig esophagus measurement**

A fresh pig esophagus sample was first imaged as the histological structure of the pig esophagus wall was similar to that of humans[140]. We took the esophagus sample from a one-year-old male pig. The sample was cut open and flattened for imaging. A histological image of the sample corresponding to the scanning position is shown in Fig. 7.2(a). As we can see, the layer morphology of the superficial esophagus wall is clearly delineated. The mucosa layer, which consists of epithelium, lamina propria and muscularis mucosa layers, is well distinguished. The main optoacoustic contrast of esophagus wall comes from hemoglobin at wavelength of 532 nm. The optoacoustic image is shown in Fig. 7.2(b). The layer structures in the optoacoustic image are identified and marked based on the depth information measured from the histological image. It can be seen that the epithelium layer is hardly resolved, because of low optoacoustic contrast. Small vessels in the lamina propria layer are recovered with high contrast, which separates the epithelium and muscularis mucosa layers. Blood vessels, lymphatic vessels, and nerves run through in the submucosa layer, resulting in high optoacoustic contrast as shown in the reconstructed image. The mucosa and submucosa layers are clearly separated by the muscularis mucosa layer, which is composed of several thin layers of smooth muscle fibers, resulting in low optoacoustic contrast comparing to its neighbor tissue.

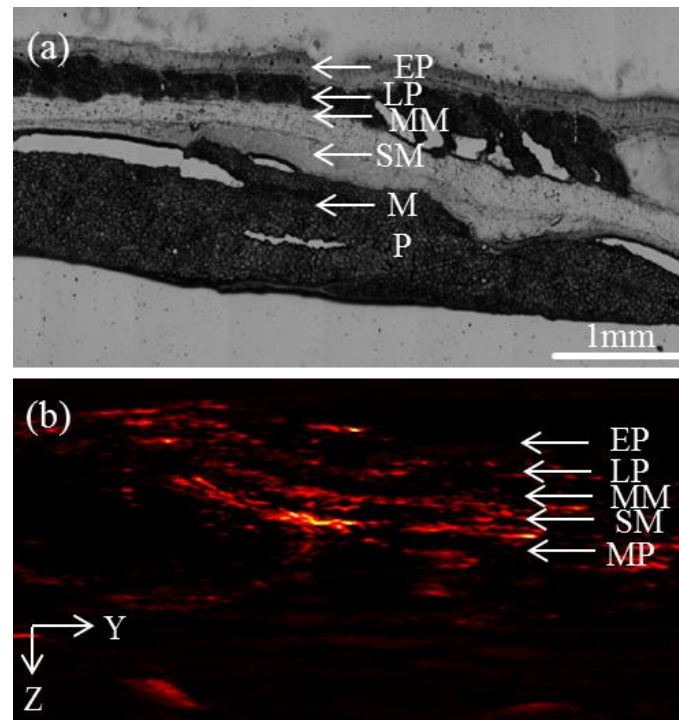


Fig. 7.2. (a) The close corresponding histology section of the esophagus sample (original magnification  $\times 4$ ). (b) The corresponding cross-sectional optoacoustic image of the esophagus sample. The white arrows in (a) and (b) indicate the layer structure of the esophagus wall. Abbreviations: EP, squamous epithelium; LP, lamina propria; MM, muscularis mucosa; SM, submucosa; MP, muscularis propria.

### 7.2.3 Human esophagus measurement

Beside pig esophagus, a 10 mm $\times$ 10 mm region of excised human esophagus sample provided by our clinical collaborator was measured in a similar way to pig esophagus sample. The sample was flattened and covered with plastic kitchen foil avoiding direct contact. The step size of the raster scan was 10  $\mu$ m along the x and y direction. The voxel size in the reconstructed 3D volume was set to 50  $\mu$ m $\times$ 50  $\mu$ m $\times$ 5  $\mu$ m. Prior to reconstruction, the acquired data was filtered using a 10–90 MHz bandpass filter. Fig. 7.3 (a) and (b) depict cross-sectional images of the esophagus wall. According to the depth and thickness of each layer measured from the histological image [Fig. 7.3(c)], the five-layered morphology of the esophagus wall is identified and marked in the optoacoustic image. In analogy to the pig esophagus sample, vessel structures in the lamina propria layer are clearly resolved, which separate the epithelium and muscularis mucosa layers. Also, the submucosa layer enriched with blood vessels and lymphatic vessels is identified with high contrast. The muscularis

mucosa layer, composed of several thin layers of smooth muscle fibers, is visualized with low contrast, which separates the mucosa and submucosa layers.

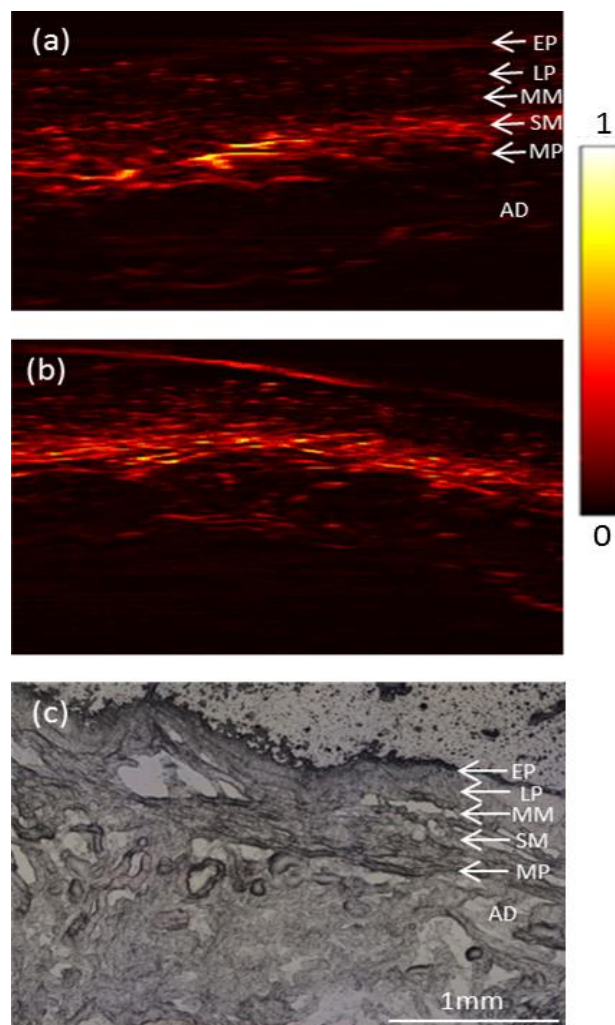


Fig. 7.3. (a) and (b) MIP results paralleled to the esophagus surface with different thickness [the thickness of (a) is 0.2mm and (b) is 0.4mm]. (c) The close corresponding histology section of the esophagus sample (original magnification  $\times 4$ ). The white arrows in (a) and (c) indicate the layer structure of the esophagus wall.

Fig. 7.4 shows the maximum-intensity projections (MIP) images parallel to the sample surface taken at different depths and several zoomed-in features are presented in the white dash rectangle regions. Representative vessel structures of each layer are indicated by white arrows. Some of the vessel structures are not well consistent as blood dried out from the excised sample. The top MIP image in Fig. 7.4(a) corresponds to the location of the mucosa layer. The bright dots are in agreement with small vessels mainly from the lamina propria

layer. The middle MIP result is related to vessel structure in the submucosa layer as shown in Fig. 7.4(b). It can be seen that middle-sized vessel structures are well distinguished. Due to the limited imaging depth at this laser wavelength, Fig. 7.4(b) corresponding to vessel structures beyond the submucosa layer is visualized with low resolution.

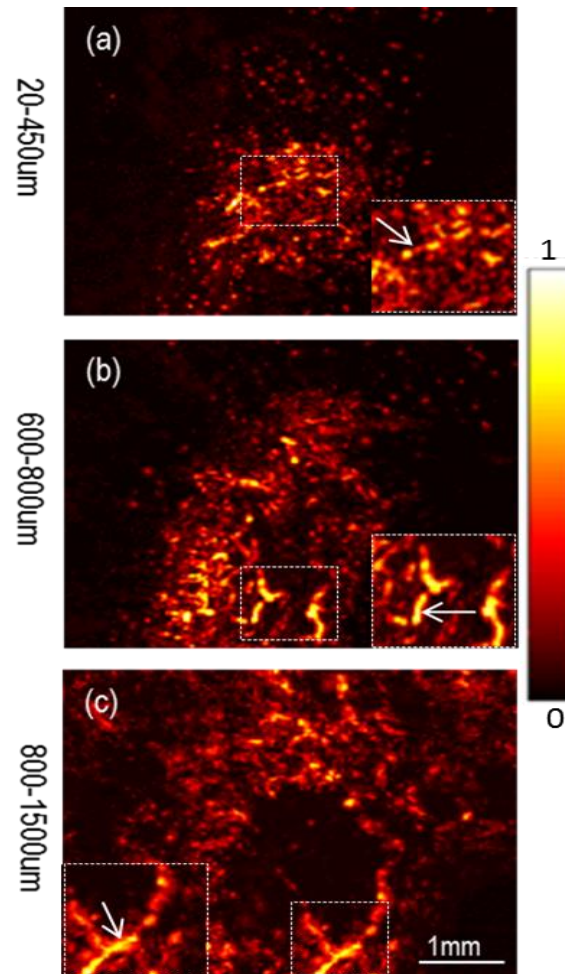


Fig. 7.4. (a)–(c) Maximum intensity projections of the reconstructed image with different thickness along the depth direction. The values on the right represent the approximate minimum depth and maximum depth used for the calculation of each projection. Zoomed-in features are marked in the white rectangle regions. Representative vessel structures are marked by white arrows.

#### 7.2.4 Multi-spectra optoacoustic imaging of esophagus sample

Multi-spectra optoacoustic images were acquired based on the same human esophagus sample. A tunable OPO laser (Innolas, Germany) with a repetition rate of 100 Hz is used as the illumination source of the mesoscopy system. The corresponding images at different

wavelengths are displayed in Fig. 7.5. All images were normalized with the laser energy for fair comparison. Optoacoustic images of the esophagus sample at six representative wavelengths exhibits strong contrast variations correlated to the deoxy-hemoglobin absorption in the mucosa and submucosa layers. For example, the superficial vessel structure at the mucosa layer reveals very strong signal intensity as hemoglobin has very high absorption at wavelength of 440 nm, while the imaging depth at this wavelength is much less than other images.

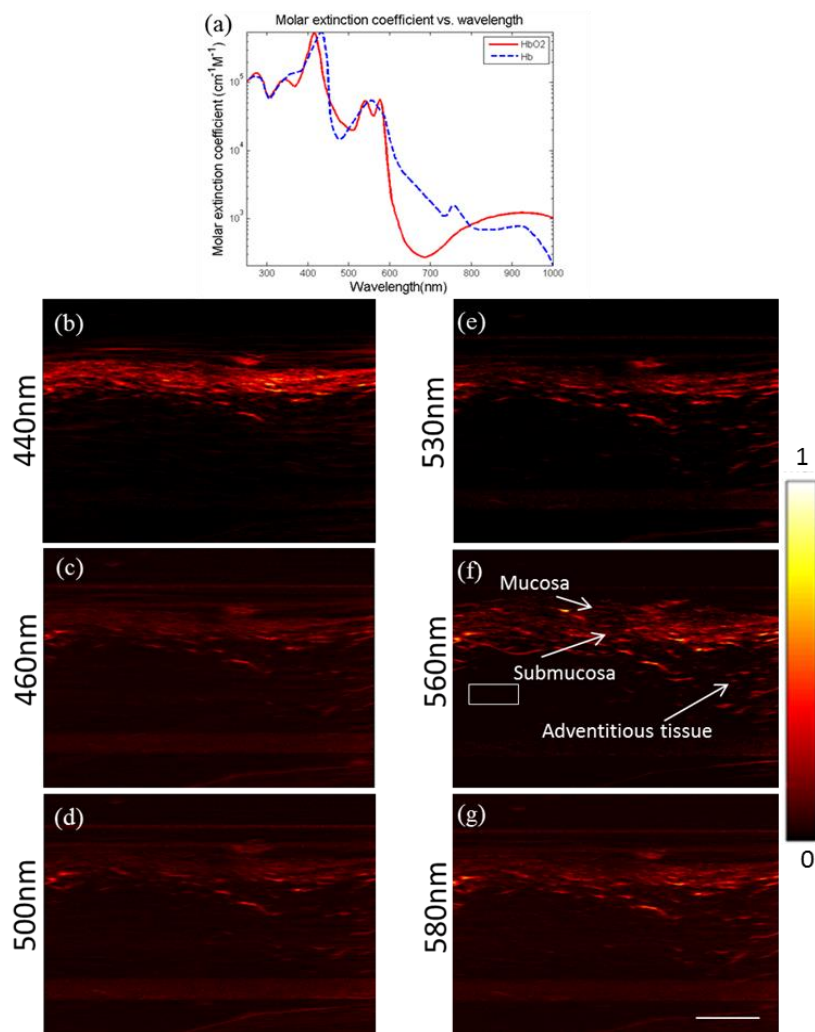


Fig. 7.5. (a) Absorption spectra of deoxy-hemoglobin. (b)-(g) Multi-spectra optoacoustic images of the esophagus samples at several wavelength, all images were normalized with the laser energy at corresponding wavelength. Scalebar 1 mm.

The relationship between the contrast to noise ratio (CNR) and wavelengths is presented in Fig. 7.6. The CNR values are calculated as the ratio between the intensity of blood vessels [marked by white arrows in Fig. 7.5(f)] and the standard deviation of the background region [white rectangle in Fig. 7.5(f)]. As we can see, the CNR values of the mucosa and submucosa areas of the superficial regions are closely correlated with the absorption spectra of hemoglobin. However, the deep region of the adventitious tissue shows less dependence on the absorption spectra as optoacoustic signal intensity in deep tissue is determined by optical absorption and attenuation together. It can be noted that, optimal CNR values at wavelength of 560 nm are achieved at the three regions of the esophagus sample. However, these results should be further validated on in vivo measurements. In this work, the optical wavelength used in this work is 532 nm, which is provided by a commercially available laser with high repetition rate of 2 kHz.

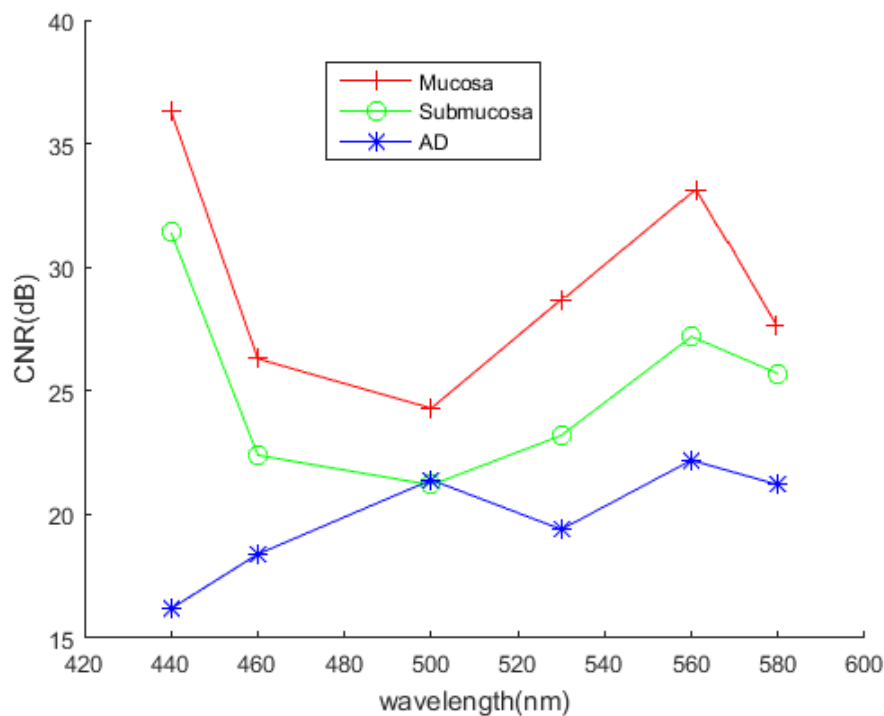


Fig. 7.6. The relationship between the CNR values and optical wavelengths calculated at three regions of the esophagus sample marked in the Fig. 3.5(f). The CNR values are calculated as the ratio between the intensity of blood vessels [marked by white arrows in Fig. 3.5(f)] and the standard deviation of the background region [white rectangle in Fig. 3.5(f)].

### 7.2.5 Frequency characteristics

As illustrated in Fig. 7.2 and Fig. 7.3, optoacoustic imaging showed good ability to distinguish the layer structures of esophagus wall by relying on the intrinsic optoacoustic contrast. Vascular structures in LP and SM layers were nicely resolved. The layer thickness of the mucosa and submucosa structure in human esophagus wall varied from few hundreds  $\mu\text{m}$  to millimeter level as shown in Fig. 7.4. Blood vessels in these layers ranged from thin capillaries with a diameter of several  $\mu\text{m}$  located in the lamina propria layer to larger vessels with a diameter of up to a hundred  $\mu\text{m}$  in the submucosa layer [96]. Thus, the frequency contents of optoacoustic signals generated from the esophagus wall were intrinsically broadband. In order to analyze the frequency characteristics, the relation between the detection bandwidth and the morphological structures of esophagus wall was studied based on the pig esophagus data shown in Fig. 7.2. Optoacoustic signals within the detection bandwidth of the mesoscopy system were separated in different frequency bands using bandpass filter. Fig. 7.7(a)-(c) depicts the raw signals at frequency bands of 10-25 MHz, 25-60MHz, and 60-90MHz respectively. Fig. 7.7(d)-(f) illustrate the corresponding reconstruction results of the three frequency bands using backprojection reconstruction approach. As we can see, low frequency contents of 10-25 MHz correspond to larger structures in the SM and MP layers, reaching approximately 2 mm penetration depth. Signals at the range of 25-60 MHz contain detailed features of the upper LP and SM layers with imaging depth about 1 mm. Vessels in the SM layers are well resolved in this frequency range while the MP layer disappears. The high frequency contents in the range of 60-90 MHz can be detected from regions of less than 1 mm depth as shown in Fig. 7.7(c), which carries information from the superficial LP layer, such as capillary vessels. The capillary dots are identified and boundaries of absorbers in the SM layer are recovered shown in Fig. 7.7(f). In order to resolve all layer structures, transducers with ultra-wide bandwidth ranging from few megahertz to a hundred MHz should be used to record optoacoustic signals.

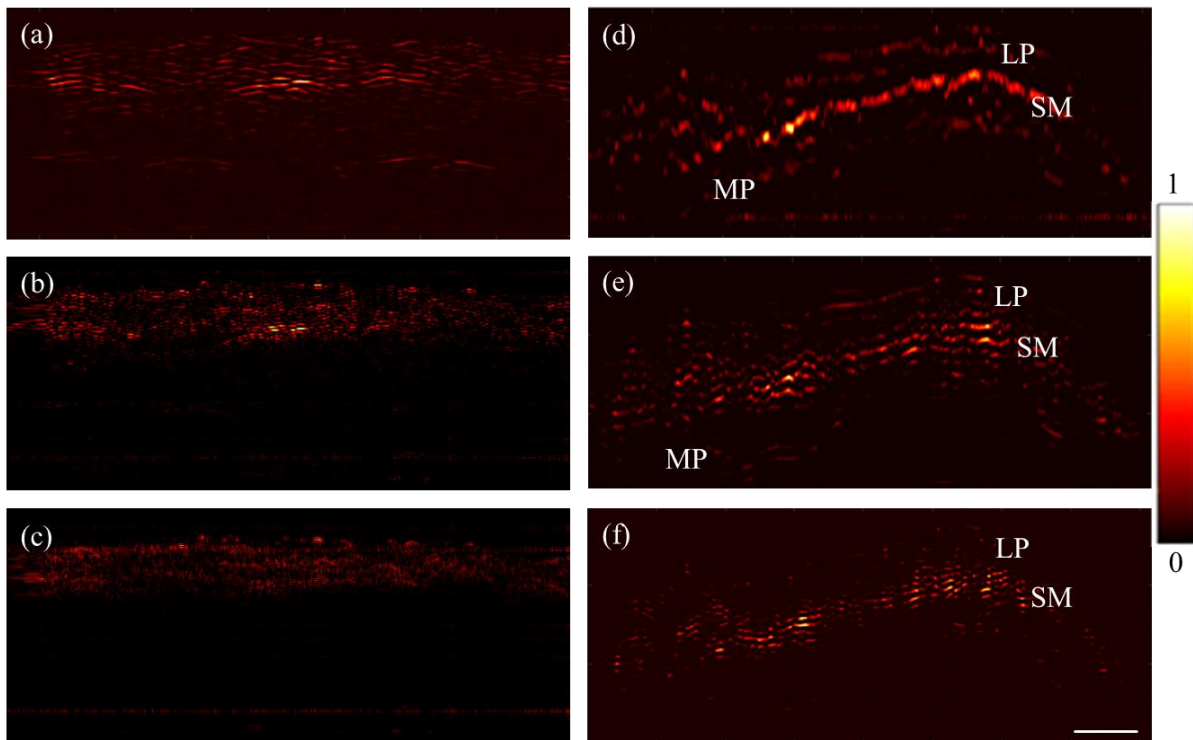


Fig. 7.7. Frequency response of the esophagus wall structure by reconstructing images at different frequency bands. (a)–(c) Raw optoacoustic signals at frequency range of 10–25 MHz, 25–60 MHz and 60–90 MHz respectively; (d)–(f) Corresponding reconstruction images of the three frequency bands. The layer structures are marked based on the depth location of each layer measured from the histological image. Scalebar 500  $\mu\text{m}$ .

### 7.3 Optoacoustic endoscopy imaging of esophageal sample

The results of mesoscopy measurements have demonstrated that optoacoustic imaging have superior capability of resolving esophagus structures. In order to validate the performance of the developed endoscopy systems, fresh pig esophagus samples are measured.

#### 7.3.1 Esophagus measurement by IVUS-based endoscopy system

To test the practicability of the IVUS-based endoscopy system, fresh pig esophagus wall was imaged as the histological structure of the pig esophagus wall was similar to that of humans. We took a fresh esophagus sample with 20 cm long from a one year old male pig. Since the excised esophagus tissue was tightly shrinking, we cut the sample open and rolled it into a 180 degree cylindrical structure as shown in Fig. 7.8(a). A histological image of the sample

along the extending direction is Fig. 7.8(b), and the corresponding B-scan optoacoustic image is depicted in Fig. 7.8(c). One cross-sectional image is shown in Fig. 7.8(d) and the volumetric image is presented in Fig. 7.8(e). As we can see from the histological image, layer structures are distinguished. According to the depth and thickness of each layer structure measured from the histological image, mucosa and submucosa layers are identified and marked in the optoacoustic images. However, thin layer structures, like the EP and LP layers were not visualized because of the limited resolution of the endoscopy probe.

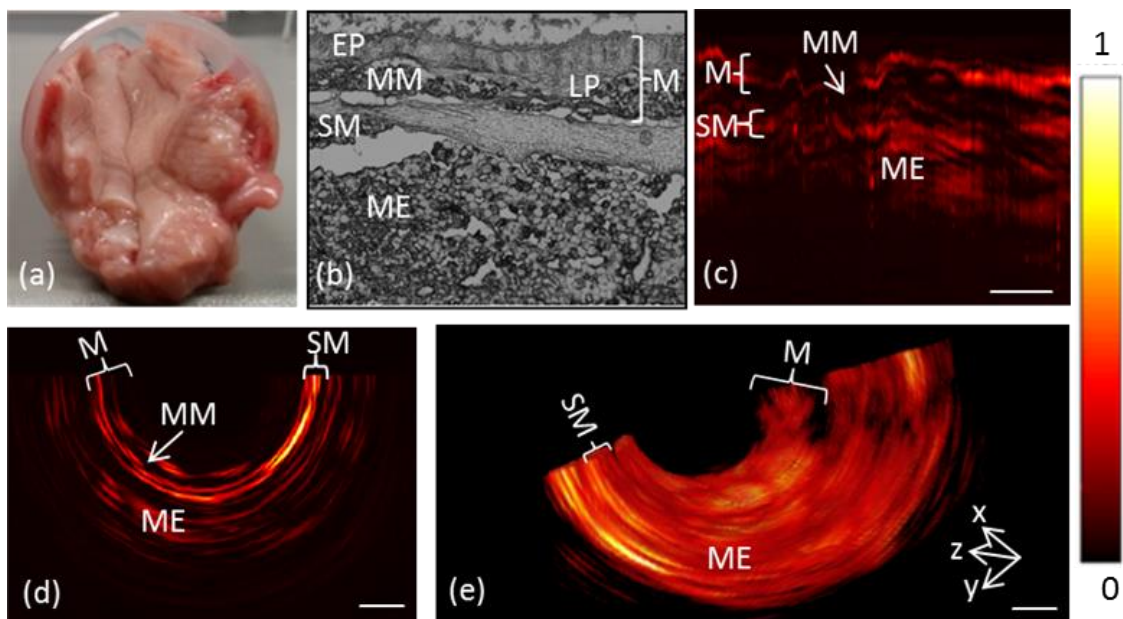


Fig. 7.8. (a) Photo of the rolled pig esophagus sample. (b) The close corresponding histology section of the esophagus sample (original magnification  $\times 4$ ). (c) and (d) typical B-scan images in two different directions. (e) Volumetric image. Layer structures in optoacoustic images are labeled according to the depth and thickness of each layer measured from the histological image. Abbreviations: EP, squamous epithelium; LP, Lamina propria; MM, Muscularis mucosa; SM, Submucosa; M, Mucosa; MP, Muscularis propria; ME, Adventitious tissue. Scalebar 500  $\mu\text{m}$ .

### 7.3.2 Challenges of in vivo measurements

For in vivo esophagus measurements of large animals, the imaging procedures are more complicated comparing to small animal experiments. Several issues of the imaging procedures should be considered, such as motion and acoustic coupling medium. In order to explore the practicability of in vivo esophagus imaging, we measured pig colon in vivo for

---

the first time using the IVUS based endoscopy probe. The whole endoscopy procedure was operated by a medical doctor. The optoacoustic endoscopic probe was combined with a video endoscopy system, which could help to position the optoacoustic probe and record the whole imaging procedure. A normal pig was anesthetized first and pure water was pumped inside the colon. Fig. 7.9 shows pictures at different stages of the measurement recorded by the video endoscopy system. As we can see in Fig. 7.9(a), the colon has an irregular lumen shape with a diameter of over 2 centimeters. The IVUS probe has limited working distance, thus only partial of the colon wall could be scanned. Therefore, the IVUS probe was positioned close to one side of the colon with the help of the video endoscopy. Clean water was continuously pumped inside the colon for cleaning and acoustic coupling. The flushing water introduced serious motions as shown in Fig. 7.9(b) and (c). A cross-sectional image was depicted in Fig. 7.9(d) where obvious artifacts were produced. Due to significant motions, volumetric images could not be reconstructed. For future *in vivo* measurements, several things can be improved. For example, acoustic gel can be used for sound coupling, which can reduce motions caused by the flushing water. For the IVUS based endoscopy probe, a protective balloon with a diameter similar to the luminal organ can be used to encapsulate the IVUS based endoscopy probe instead of the metal head housing. In such implementation, the whole endoscopy probe can be passed through the working channel. When the probe reaches the region of interest inside the luminal organ, the balloon will be dilated and the luminal organ can constrict around the balloon, forming a stable environment. With these improvements, optoacoustic endoscopy probes introduced in this section will be applied for *in vivo* esophagus imaging in the future.

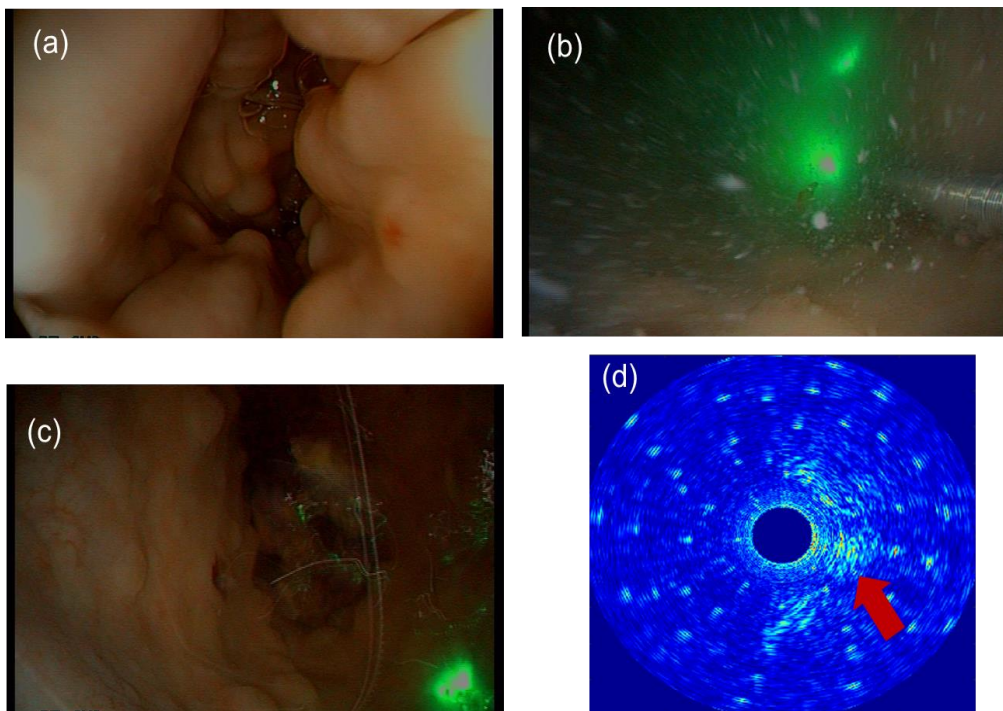


Fig. 7.9 Pictures of in vivo pig colon measurements. (a) Pig colon before water flushing; (b) and (c) Pig colon with flushing water. The illuminated areas indicate the position of the IVUS based endoscopy probe. (d) One cross-sectional image of the pig colon. The red arrow points out the optoacoustic image of the colon wall.

### 7.3.3 Esophagus measurement by focused detector based endoscopy system

The focused detector based endoscopy probe was also tested on an excised esophagus sample from a one year old male pig. Instead of radial scanning, we imaged the sample in a linear scanning configuration. The crysliced image is shown in Fig. 7.10(a). The corresponding optoacoustic image is depicted in Fig. 7.10(b), where blood vessels in mucosa and submucosa layers are resolved relying on the focus of the transducer. The sample surface is positioned inside the focus of the transducer, resulting good lateral resolution. However, structures gradually get elongated as they are out of the focus region of the transducer.

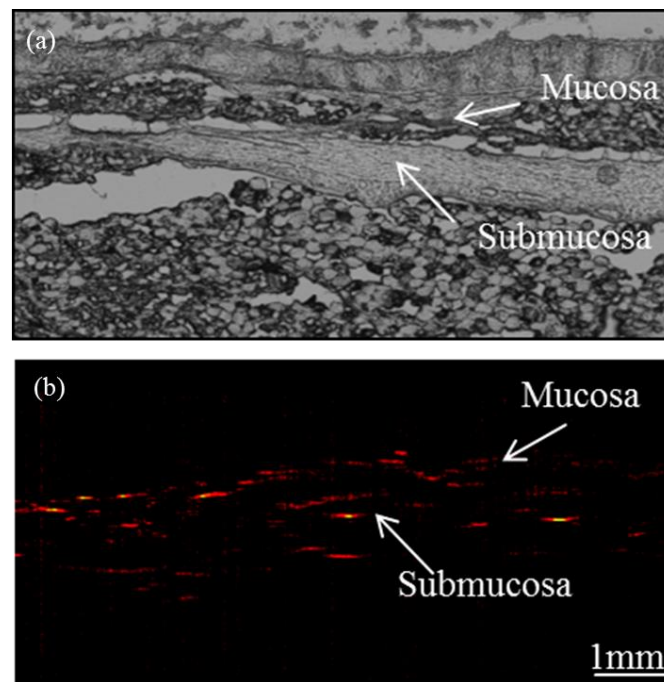


Fig. 7.10. Optoacoustic imaging of pig esophagus sample. (a) The histological image corresponding to the scanning position. (b) Optoacoustic cross-sectional image.

In order to test the practicability of the endoscopy probe, inner surface of fingers from a human volunteer were scanned. The volunteer rolled fingers around a plastic cylinder. Half circle of the cylinder was cut open and covered with plastic membrane, forming a detection window for sound and light. A representative sectional optoacoustic image is depicted in Fig. 7.11(a). Two zoomed areas marked in the red ellipses are displayed in Fig. 7.11(b) and (c). It can be seen that vessel structures are resolved relying on the focus of the ultrasound transducer. Besides, three black lines acted as indicators were marked in the opposite side of the detection window. The corresponding features are visualized in the region indicated by the red arrow in Fig. 7.11(a). The MIP image in the polar coordinate is given in Fig. 7.11(d), where we can see the layer structure of the skin marked by the white arrows. Besides, the MIP image along the depth direction is shown in Fig. 7.11(e), where dense vessels are visualized. The three line objects are resolved with low resolution as indicated by the yellow arrow shown in Fig. 7.11(e). Furthermore, we can see the layer structure of the skin in the MIP image along the scanning direction as illustrated in Fig. 7.13(f), where white arrows points to the surface structures.

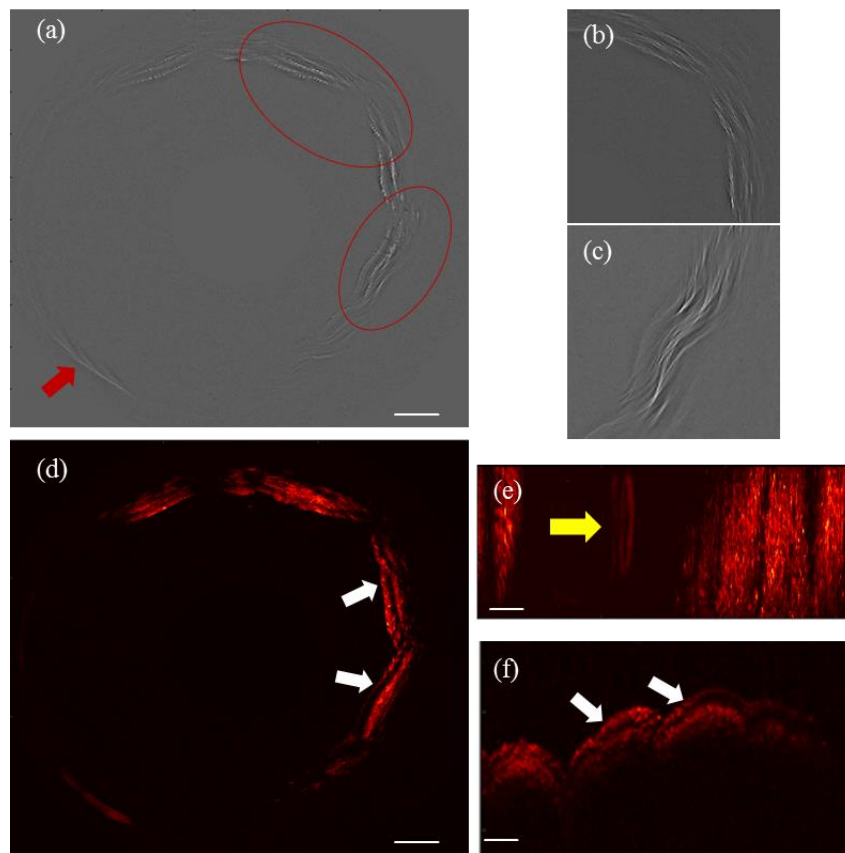


Fig. 7.11. (a) Sectional image of finger skin. (b) and (c) are zoomed-in images of the red ellipses shown in (a). (d) MIP image in the polar coordinate. (e) and (f) MIP images along the depth and scanning directions respectively. White arrows in both images point to the surface structures of human skin. Scalebar 1 mm.

### 7.3.4 Further development

The focused detector based endoscopy probe has relative large diameter (over 6 mm in diameter), impossible to pass through the working channel of commercial video endoscopy system. Therefore, an endoscopy probe should be developed, which allows it to scan independently. Fig. 7.12 shows the capsule based optoacoustic endoscopy system designed for human esophagus imaging. Fig. 7.12(a) presents the working principle and Fig. 7.12(b) depicts the schematic of the capsule probe. The capsule is a plastic lumen with a diameter of approximately 1.8 cm and length of 2.5 cm. The spherical focused ultrasound detector with illumination fiber is centered in the capsule. Flexible torque coils are used to transmit rotation force smoothly from the scanning unit to the detector. A position measuring unit is applied to record the pulling distance of the capsule during volumetric imaging. For in vivo

measurements, the capsule probe will be swallowed and gradually be pushed down along the gastrointestinal tract under the natural propulsion force of peristalsis. After the probe reaches the distal-most region of interest, the esophagus wall constricts around the capsule, which makes the capsule center and stable inside the esophagus lumen. In such arrangement, the endoscopy probe is stabilized inside the capsule, which reduces the motion artifacts during in vivo volumetric scanning. Optoacoustic waves and laser light can pass through the detection window of the capsule. Volumetric images with the same length of the detection window can be obtained without moving the capsule. By changing the capsule position, more regions of the esophagus wall can be imaged.

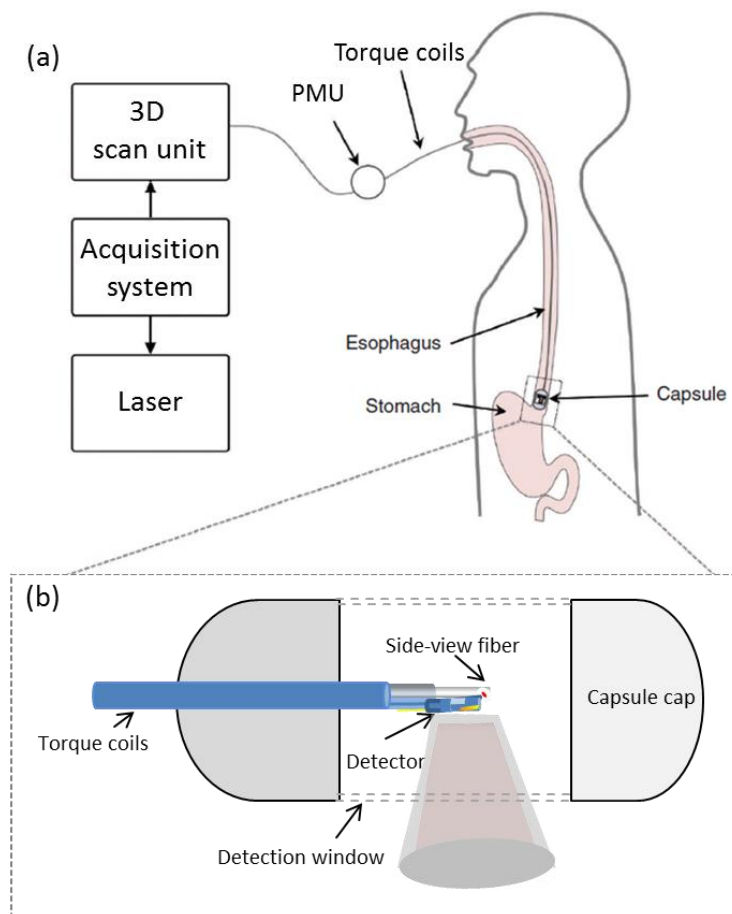


Fig. 7.12. Principle of capsule based optoacoustic endoscopy system. (a) Schematic of capsule endoscopy system and working principle. (b) Schematic of the capsule endoscopy probe. PMU: position measuring unit.

## 7.4 Summary and discussion

In this chapter, cross-sectional optoacoustic images acquired by the mesoscopy system nicely identified the layer structures of the esophagus wall. The mucosa and submucosa layers were clearly distinguished based on optoacoustic contrast. The MIP results revealed vessel structure patterns of different layers. The relation between the CNR values and laser wavelength were analyzed based on the multi-spectra optoacoustic images obtained by the mesoscopy system, which suggested the optimal optical wavelength for esophagus imaging. The frequency response of the esophagus wall was studied to understand the necessary frequency bandwidth of recovering optoacoustic absorbers in each layer of the esophagus wall. Results of several esophagus measurements proved optoacoustic imaging can significantly distinguish the layer structures of esophagus wall with high tissue contrast. Even though images were not obtained in endoscopic mode, this study demonstrated the clinical potential of optoacoustic on esophagus imaging. Results of mesoscopy measurements can be regarded as reference images to validate the imaging performance of optoacoustic endoscopy and help to optimize the development of endoscopy systems.

The performance of the developed endoscopy systems were validated on esophagus tissue. Structures of esophagus were nicely resolved using the developed endoscopy systems, which showed great potential for esophagus imaging. However, several improvements should be addressed. For example, the first experience of *in vivo* pig measurement presented the challenges of *in vivo* endoscopy experiments. The acoustic coupling medium and motion issues should be considered for *in vivo* measurements. With these necessary improvements, the endoscopy probes developed in this section will be tested on animals *in vivo* in the future. To improve the practicability, the capsule probe was introduced to encapsulate the whole endoscopy probe inside a capsule, which enabled the focused detector based probe scanning independently.

Overall, optoacoustic imaging has demonstrated the superior capability of resolving the layer structures of esophagus wall, showing great clinical impacts for endoscopy applications.

## **Chapter 8 Conclusion and outlook**

### **8.1 Conclusion**

Optoacoustic endoscopy is a novel imaging technique that embodies optoacoustic techniques in a small probe to image internal organs through intracavitary introduction. High potential of optoacoustic endoscopy is highlighted by various implementations and animal measurements. However, there are few study investigating the imaging performance of optoacoustic on esophagus samples from human or large animals (like pigs), as their anatomical structures are very different to small animals. Besides, current endoscopy implementations are designed for small animal imaging, which are not optimized for human esophagus imaging.

To enhance the performance of optoacoustic endoscopy, several endoscopy probes were built based on different scanning geometries, ultrasound transducers and illumination configurations. For example, a curved scanning endoscopy probe was implemented using the IVUS detector. The curved scanning geometry offered larger effective acceptance angle, along the direction of image formation, which can improve image quality compared to rotational systems. The resolution characterized by the microsphere phantom was 27% more accurate in the curved mode than the linear scanning mode against the known dimensions of the phantoms imaged. Besides, a hybrid optical resolution and acoustic resolution optoacoustic endoscopy with a single sensor was implemented. Experiments of phantoms and ex vivo samples proved that the proposed endoscopy probe could gain optical resolution imaging of the surface and tomography imaging for the deeper features. Beside single element based endoscopy probe, we investigated the merits and imaging performance achieved with a miniaturized linear transducer, which could allow the endoscopic deployment of MSOT. In contrast to single transducer implementations, transducer arrays can be employed in rotation or translation mode and offer real-time 2D image formation based on parallelized tomographic detection. Overall, these implementations showed possible

improvements of optoacoustic endoscopy probes, enabling to optimize the development of optoacoustic endoscopy system.

In order to apply optoacoustic for esophagus imaging, two optoacoustic endoscopy systems were built. The first one was an IVUS based endoscopy probe, which was fully encapsulated in a custom-designed plastic tube with a diameter of 3.6 mm, compatible with the working channel. To accurately transmit the rotating force, the probe was encapsulated using flexible torque coils. This design had more simplified distal structure with less mechanical components inside the probe. Phantoms and pig esophagus measurements *ex vivo* were conducted to test its imaging performance. However, limited sensitivity of the IVUS probe and poor transverse resolution restricted the performance of acquiring high quality images. In order to improve the image quality, an endoscopy probe based on a spherical focused detector was implemented. Phantoms and esophagus samples were measured, and high quality images were recovered inside the focus of the transducer. Furthermore, the implementation of capsule endoscopy system was introduced and validated, which showed potential of scanning the esophagus wall independently.

The relation between the detection bandwidth and the imaging capability of esophagus samples was studied based on simulations and tissue experiments. The frequency response of the simulated esophagus wall theoretically indicated the necessary frequency bandwidth of recovering absorbers in each layer of the esophagus wall. To evaluate the simulation results, fresh pig esophagus samples were imaged using transducers with center frequencies at 15 and 50 MHz respectively. Comparing the results of both detectors, it can be clearly noted that 50 MHz detector showed superior imaging ability on resolving the thin layers of esophagus wall, while the 15 MHz detector achieved larger imaging depth. Therefore, ultra-wide bandwidth detectors ranging from few megahertz to a hundred MHz should be used to record optoacoustic signals.

Beside instrumentation, we improved the model-based reconstruction approach by developing a fast sparse recovery method along with coherence factor weighting. This approach can be applied to reconstruct optoacoustic signals acquired in the linear or curved scanning endoscopy or tomography systems. It has been proved that the proposed approach can save enormous memory and significantly accelerate the computation time compared to the original sparse based approach. Besides, an image quality enhancement approach was

introduced, which integrated information from multiple optoacoustic images acquired at sub-diffraction steps into one high resolution image by means of an iterative registration algorithm. Experimental validations performed in phantoms and ex-vivo tissue samples confirmed that the suggested approach rendered significant improvements in terms of optoacoustic image resolution and quality without introducing significant alterations into the signal acquisition hardware or inversion algorithms.

In order to validate the clinical relevance of optoacoustic imaging on excised esophagus samples, high resolution optoacoustic mesoscopy system with detection bandwidth ranging from 10 to 90 MHz was applied to measure esophagus samples. The layer morphology of the superficial esophagus wall was clearly delineated in optoacoustic images. The MIP results revealed vessel structure patterns of different layers. The relation between the CNR values and the wavelength were analyzed based on the multi-spectra optoacoustic images obtained by the mesoscopy system, which suggested the optimal optical wavelength for esophagus imaging. Overall, results reported from the esophagus measurements demonstrated the superior capability of optoacoustic imaging on resolving the layer structures of esophagus wall, which proved its great clinical potential for esophagus imaging. Furthermore, phantoms and esophagus tissues were measured to test the performance of the developed endoscopy systems. Mucosa and submucosa layers of pig esophagus wall have been clearly resolved by the IVUS based endoscopy. For the focused detector based endoscopy system, esophagus samples and human skin were measured, and high resolution images were recovered relying on the focus of the transducer.

In conclusion, this work presented the system development of optoacoustic endoscopy and corresponding characterization experiments. Results of biological measurements from optoacoustic mesoscopy and the developed endoscopy systems together demonstrated the great capability of optoacoustic imaging on resolving the structures of esophagus from pigs and human, showing great clinical impacts of the technology for esophagus imaging.

## **8.2 Outlook**

Performance of the proposed endoscopy probes can be further improved. As for the curved endoscopy, the image quality can be further enhanced using a detector with a larger sensing

angle. To enable passing the curved endoscope through the working channel of an optical endoscope one could employ a pre-shaped guidewire with a good shape memory or a guidewire with an actively deflectable tip. For the hybrid endoscopy probe, it should be noted that, due to the short working distance of the OR fiber, the probe in the current implementation has to be positioned close to the sample surface, thus only a limited luminal segment can be imaged at a time. To improve the applicability of the presented endoscope for obtaining circumferential images of the big lumen, a GRIN fiber with longer focal distance should be applied. Besides, beam-splitting or preferably two time-interleaved laser sources could be employed for concurrent imaging, which can further improve imaging efficiency.

Several aspects can be addressed to further improve the developed endoscopy systems. For the IVUS based endoscope system, the ability of resolving esophagus structures is limited by the acoustic properties of the employed IVUS transducer. Advanced transducers with higher sensitivity and wider detection bandwidth should be used, for example, optical interferometry based ultrasound sensors. In order to increase the imaging depth, laser light in the near infrared can be applied. Furthermore, multi-spectra optoacoustic endoscopy imaging can be implemented in the future for visualizing functional information, such as the oxygenation saturation of hemoglobin, or molecular information, such as the distribution of various contrast agents or molecular probes. The capsule endoscopy probe based on spherical focused detector has been validated on phantoms and excised esophagus samples, which obtained high quality images relying on the focus of the transducer. However, further improvements of the capsule endoscopy probe should be made for esophagus imaging. As the image resolution is determined by the ultrasound focusing ability of the transducer, transducers with longer focal zone and high sensitivity can be applied. In order to apply the endoscopy probe for human esophagus measurements, several challenges should be considered. For example, the catheter and capsule used for encapsulating the endoscopy probes should be clinically acceptable and transparent to sound and light. Besides, the rotation and translation force should be transmitted smoothly to scan the endoscopy probe with a high rotation speed, which enables fast imaging and helps to reduce motion artifacts for volumetric imaging inside human body. A micro-camera system can be added in the capsule endoscopy, which can monitor the position of the capsule probe and provides complimentary video information.

As for the image reconstruction part, there is no effective image reconstruction technique available to enhance the image quality of the radial scanning endoscopy configuration. In the future, advanced reconstruction approaches should be adapted to improve the image quality of radial scanning endoscopy. For example, model-based techniques can be used to model the radial scanning geometry and integrate the detector properties in the reconstruction process.

Through analyzing optoacoustic images of pig and human esophagus samples, results have demonstrated the superior capability of optoacoustic on resolving the layer structures of esophagus wall. In order to fully investigate the potential of optoacoustic imaging, more excised esophagus tissues including diseased and healthy samples, should be measured using optoacoustic techniques. With these measurements, several challenges can be investigated. For example, how well optoacoustic techniques differentiate the diseased and health tissues; whether optoacoustic techniques can diagnose or stage esophagus cancer accurately; what the benefits of multi-spectra optoacoustic for esophagus imaging. Furthermore, the developed optoacoustic endoscopy systems can be evaluated on the exercised esophageal samples.

## Acknowledgements

I would like to thank Prof. Vasilis Ntziachristos and Dr. Andreas Buehler for giving me the opportunity of studying my Ph.D. in the interesting field of optoacoustic imaging. Their advices and support were very helpful for my work, and their creativity and working attitude were inspirational for my future career. Special thanks for helping writing my publications and allowing me to present my research at international conference.

I would like to thank Prof. Kleeff Jorg, Prof. Dieter Sauer, Dr. Alexander Novotny, and Dr. Krzysztof Flisikowski for their help for providing tissue samples and advices for the development of optoacoustic endoscopy system. Thanks to Georg Wissmeyer for the thoughtful discussions and cooperation, which lead to the publication “Hybrid optical and acoustic resolution optoacoustic endoscopy”. Besides, I want to thank Dr. Jaya Prakash Naidu and Subhamoy Mandal, for helping me to improve my reconstruction method and the successful cooperation on the publication “Optoacoustic tomography using accelerated sparse recovery and coherence factor weighting” and “Improving Optoacoustic Image Quality via Geometric Pixel Super-resolution Approach”. Also thanks to Dr. Xosé-Luis Déan-Ben for giving comments for these two publications.

Thanks to my office colleagues, Mathias Schwarz, Dominic Soliman, Ludwig Prada, Andrei Berezhnoi, Antonios Stylogiannis, and other colleagues, like Dmitry Bozhko, Xiaopeng Ma, Dr. Jiao Li, Yiyong Han, Yuanhui Huan, Juan Aguirre, Roman Schnaiderman, Panagiotis Symvoulidis, Alexander Dima, Yuanyuan Jiang for their kind help for my work and life in Germany. Their fruitful discussions and creative ideas helped me a lot during my Ph.D. work. To the rest of my IBMI coworkers, I would like to say thanks for the beautiful memory we spent together.

Many thanks to Dr. Christian Zakian, Dr. Saak V. Ovsepian and Dr. Barbara Schroeder for helping my scientific writing and proof-reading of parts of this thesis. Furthermore, many thanks to the administrative personal Silvia Weinzierl, Susanne Stern, Dr. Julia Thomas, Dr. Doris Bengel, Zsuzsanna Öszi, Dr. Andreas Brandstaetter, Martina Riedl for their help in

administrative matters and to the technical personal Sarah Glasl, Florian Jürgelait, Uwe Klemm for precious support in animal handling and cryoslicing.

Finally, I'd like to thank my grandparents and parents, my brother, family members and friends for their love and support during my Ph.D. study.

## Publication lists

### Publications in peer-reviewed journals

1. **Hailong He**, Andreas Buehler, and Vasilis Ntziachristos, “Super resolution technique for optoacoustic imaging”, *IEEE Trans. Medical Imaging*, Vol.35, No 3, March 2016.
2. **Hailong He**, Andreas Buehler, Dmitry Bozhko and Vasilis Ntziachristos, “Importance of ultrawide bandwidth for optoacoustic esophagus imaging”, *IEEE Trans. Medical Imaging*, November 2017.
3. **Hailong He**, Georg Wissmeyer, Saak V. Ovsepian, Andreas Buehler, and Vasilis Ntziachristos, “Hybrid optical and acoustic resolution optoacoustic endoscopy”, *Optics Letters*, Vol 41, No. 12, June 2016.
4. **Hailong He**, Andreas Buehler, and Vasilis Ntziachristos, “Optoacoustic endoscopy in curved scanning mode”, *Optics Letters*, Vol. 40, No. 20, 2015.
5. **Hailong He\***, Jaya Prakash\*, Andreas Buehler, and Vasilis Ntziachristos, “Optoacoustic tomography using accelerated sparse recovery and coherence factor weighting”. *Tomography*, Vol. 2, No 2, 2016. \*Equal contributions.

### International conference contributions and proceedings

1. **Hailong He**, Georg Wissmeyer, Saak V. Ovsepian, Andreas Buehler, and Vasilis Ntziachristos, “Optoacoustic endoscopy with optical and acoustic resolution”, In Proceedings of the SPIE BIOS, Photonics West, San Francisco, California, United States, 2017. Oral presentation.
2. **Hailong He\***, Jaya Prakash\*, Andreas Buehler, and Vasilis Ntziachristos, “Optoacoustic tomography using accelerated sparse recovery and coherence factor weighting”, In Proceedings of the SPIE BIOS, Photonics West, San Francisco, California, United States, 2017. Oral presentation.
3. **Hailong He**, Andreas Buehler, and Vasilis Ntziachristos, “Optoacoustic endoscopy in curved scanning mode”. In Proceedings of the SPIE BIOS, Photonics West, San Francisco, California, United States, 2016. Oral presentation

4. **Hailong He**, Subhamoy Mandal, Andreas Buehler, X. Luís Deán-Ben, Daniel Razansky, and Vasilis Ntziachristos. “Optoacoustic Imaging Quality Enhancement Based on Geometrical Super-Resolution Method.” In Proceedings of the SPIE BIOS, Photonics West, San Francisco, California, United States, 2016. Oral presentation
5. Andreas Buehler, **Hailong He**, and Vasilis Ntziachristos, “Real-time optoacoustic endoscopy on a miniaturized linear transducer”, European Conferences on Biomedical Optics 2015.
6. **Hailong He**, Andreas Buehler, and Vasilis Ntziachristos, “Geometrical super-resolution image processing in optoacoustic tomography”, European Conferences on Biomedical Optics 2015, poster.

## Bibliography

- [1] S. Kudo, S. Tamura, T. Nakajima, H. Yamano, H. Kusaka, and H. Watanabe, "Diagnosis of colorectal tumor lesions by magnifying endoscopy," *Gastrointest Endosc*, vol. 44, pp. 8-14, Jul 1996.
- [2] J. Mannath and K. Ragnath, "Role of endoscopy in early oesophageal cancer," *Nat Rev Gastroenterol Hepatol*, Nov 03 2016.
- [3] R. Weissleder, "Scaling down imaging: molecular mapping of cancer in mice," *Nat Rev Cancer*, vol. 2, pp. 11-8, Jan 2002.
- [4] V. Ntziachristos, J. Ripoll, L. V. Wang, and R. Weissleder, "Looking and listening to light: the evolution of whole-body photonic imaging," *Nat Biotechnol*, vol. 23, pp. 313-20, Mar 2005.
- [5] D. Razansky, A. Buehler, and V. Ntziachristos, "Volumetric real-time multispectral optoacoustic tomography of biomarkers," *Nat Protoc*, vol. 6, pp. 1121-9, Aug 2011.
- [6] D. Razansky, M. Distel, C. Vinegoni, R. Ma, N. Perrimon, R. W. Köster, *et al.*, "Multispectral optoacoustic tomography of deep-seated fluorescent proteins in vivo," *Nature Photonics*, vol. 3, pp. 412-417, 2009.
- [7] A. Taruttis and V. Ntziachristos, "Advances in real-time multispectral optoacoustic imaging and its applications," *Nature Photonics*, vol. 9, pp. 219-227, 2015.
- [8] A. Taruttis, G. M. van Dam, and V. Ntziachristos, "Mesoscopic and Macroscopic Optoacoustic Imaging of Cancer," *Cancer Res*, vol. 75, pp. 1548-1559, Apr 15 2015.
- [9] V. Ntziachristos, "Going deeper than microscopy: the optical imaging frontier in biology," *Nat Methods*, vol. 7, pp. 603-14, Aug 2010.
- [10] G. Lee, H. I, S. J. Kim, Y. J. Jeong, I. J. Kim, K. Pak, *et al.*, "Clinical Implication of PET/MR Imaging in Preoperative Esophageal Cancer Staging: Comparison with PET/CT, Endoscopic Ultrasonography, and CT," *J Nucl Med*, vol. 55, pp. 1242-1247, May 27 2014.
- [11] S. B. Perlman, B. S. Hall, and M. Reichelderfer, "PET/CT imaging of inflammatory bowel disease," *Semin Nucl Med*, vol. 43, pp. 420-6, Nov 2013.
- [12] J. M. Artigas, M. Marti, J. A. Soto, H. Esteban, I. Pinilla, and E. Guillen, "Multidetector CT angiography for acute gastrointestinal bleeding: technique and findings," *Radiographics*, vol. 33, pp. 1453-70, Sep-Oct 2013.
- [13] R. Matthews and M. Choi, "Clinical Utility of Positron Emission Tomography Magnetic Resonance Imaging (PET-MRI) in Gastrointestinal Cancers," *Diagnostics (Basel)*, vol. 6, Sep 09 2016.
- [14] M. F. Berry, "Esophageal cancer: staging system and guidelines for staging and treatment," *J Thorac Dis*, vol. 6 Suppl 3, pp. S289-97, May 2014.
- [15] V. Conteduca, D. Sansonno, G. Ingravallo, S. Marangi, S. Russi, G. Lauletta, *et al.*, "Barrett's esophagus and esophageal cancer: An overview," *International Journal of Oncology*, vol. 41, pp. 414-424, Aug 2012.
- [16] G. N. Tytgat, H. Bartelink, R. Bernards, G. Giaccone, J. J. van Lanschot, G. J. Offerhaus, *et al.*, "Cancer of the esophagus and gastric cardia: recent advances," *Dis Esophagus*, vol. 17, pp. 10-26, 2004.
- [17] K. M. Horton and E. K. Fishman, "Current role of CT in imaging of the stomach," *Radiographics*, vol. 23, pp. 75-87, Jan-Feb 2003.
- [18] A. B. Bühler, "Multi-Spectral Optoacoustic Tomography: Methods and Applications," 2013.

- [19] J. Zhang, D. Tian, R. Lin, G. Zhou, G. Peng, and M. Su, "Phase-contrast X-ray CT imaging of esophagus and esophageal carcinoma," *Sci Rep*, vol. 4, p. 5332, 2014.
- [20] B. Liu, M. Ramalho, M. AlObaidy, K. K. Busireddy, E. Altun, J. Kalubowila, *et al.*, "Gastrointestinal imaging-practical magnetic resonance imaging approach," *World J Radiol*, vol. 6, pp. 544-66, Aug 28 2014.
- [21] G. H. Glover, "Overview of functional magnetic resonance imaging," *Neurosurg Clin N Am*, vol. 22, pp. 133-9, vii, Apr 2011.
- [22] N. J. Hangiandreou, "AAPM/RSNA physics tutorial for residents. Topics in US: B-mode US: basic concepts and new technology," *Radiographics*, vol. 23, pp. 1019-33, Jul-Aug 2003.
- [23] M. Esaki, T. Matsumoto, T. Moriyama, K. Hizawa, Y. Ohji, S. Nakamura, *et al.*, "Probe EUS for the diagnosis of invasion depth in superficial esophageal cancer: a comparison between a jelly-filled method and a water-filled balloon method," *Gastrointest Endosc*, vol. 63, pp. 389-95, Mar 2006.
- [24] E. Vazquez-Sequeiros and M. J. Wiersema, "High-frequency US catheter-based staging of early esophageal tumors," *Gastrointest Endosc*, vol. 55, pp. 95-9, Jan 2002.
- [25] P. N. Wells and H. D. Liang, "Medical ultrasound: imaging of soft tissue strain and elasticity," *J R Soc Interface*, vol. 8, pp. 1521-49, Nov 07 2011.
- [26] C. Technology Assessment, J. Liu, S. Carpenter, R. Chuttani, J. Croffie, J. Disario, *et al.*, "Endoscopic ultrasound probes," *Gastrointest Endosc*, vol. 63, pp. 751-4, May 2006.
- [27] S. Yoshinaga, I. Oda, S. Nonaka, R. Kushima, and Y. Saito, "Endoscopic ultrasound using ultrasound probes for the diagnosis of early esophageal and gastric cancers," *World J Gastrointest Endosc*, vol. 4, pp. 218-26, Jun 16 2012.
- [28] M. Goetz, N. P. Malek, and R. Kiesslich, "Microscopic imaging in endoscopy: endomicroscopy and endocytoscopy," *Nat Rev Gastroenterol Hepatol*, vol. 11, pp. 11-8, Jan 2014.
- [29] R. Singh, H. Karageorgiou, V. Owen, K. Garsed, P. J. Fortun, E. Fogden, *et al.*, "Comparison of high-resolution magnification narrow-band imaging and white-light endoscopy in the prediction of histology in Barrett's oesophagus," *Scand J Gastroenterol*, vol. 44, pp. 85-92, 2009.
- [30] M. C. Godoy, J. F. Bruzzi, C. Viswanathan, M. T. Truong, M. D. Guimaraes, W. L. Hofstetter, *et al.*, "Multimodality imaging evaluation of esophageal cancer: staging, therapy assessment, and complications," *Abdom Imaging*, vol. 38, pp. 974-93, Oct 2013.
- [31] A. Hoffman, M. Goetz, M. Vieth, P. R. Galle, M. F. Neurath, and R. Kiesslich, "Confocal laser endomicroscopy: technical status and current indications," *Endoscopy*, vol. 38, pp. 1275-83, Dec 2006.
- [32] J. Liu, M. Li, Z. Li, X. L. Zuo, C. Q. Li, Y. Y. Dong, *et al.*, "Learning curve and interobserver agreement of confocal laser endomicroscopy for detecting precancerous or early-stage esophageal squamous cancer," *PLoS One*, vol. 9, p. e99089, 2014.
- [33] M. A. Lediju Bell, N. Kuo, D. Y. Song, and E. M. Boctor, "Short-lag spatial coherence beamforming of photoacoustic images for enhanced visualization of prostate brachytherapy seeds," *Biomed Opt Express*, vol. 4, pp. 1964-77, 2013.
- [34] B. J. Vakoc, D. Fukumura, R. K. Jain, and B. E. Bouma, "Cancer imaging by optical coherence tomography: preclinical progress and clinical potential," *Nat Rev Cancer*, vol. 12, pp. 363-8, May 2012.
- [35] G. D. De Palma, "Confocal laser endomicroscopy in the "in vivo" histological diagnosis of the gastrointestinal tract," *World Journal of Gastroenterology*, vol. 15, p. 5770, 2009.
- [36] P. Amornphimoltham, A. Masedunskas, and R. Weigert, "Intravital microscopy as a tool to study drug delivery in preclinical studies," *Adv Drug Deliv Rev*, vol. 63, pp. 119-28, Jan-Feb 2011.
- [37] V. Becker, F. J. van den Broek, A. M. Buchner, E. Dekker, M. B. Wallace, S. von Delius, *et al.*, "Optimal fluorescein dose for intravenous application in miniprobe-based confocal laser scanning microscopy in pigs," *J Biophotonics*, vol. 4, pp. 108-13, Jan 2011.
- [38] M. Goetz and T. D. Wang, "Molecular imaging in gastrointestinal endoscopy," *Gastroenterology*, vol. 138, pp. 828-33 e1, Mar 2010.

- [39] T.-H. Tsai, J. Fujimoto, and H. Mashimo, "Endoscopic Optical Coherence Tomography for Clinical Gastroenterology," *Diagnostics*, vol. 4, pp. 57-93, 2014.
- [40] S. H. Yun, G. J. Tearney, B. J. Vakoc, M. Shishkov, W. Y. Oh, A. E. Desjardins, *et al.*, "Comprehensive volumetric optical microscopy in vivo," *Nat Med*, vol. 12, pp. 1429-33, Dec 2006.
- [41] M. J. Gora, J. S. Sauk, R. W. Carruth, K. A. Gallagher, M. J. Suter, N. S. Nishioka, *et al.*, "Tethered capsule endomicroscopy enables less invasive imaging of gastrointestinal tract microstructure," *Nat Med*, vol. 19, pp. 238-40, Feb 2013.
- [42] L. Liu, J. A. Gardecki, S. K. Nadkarni, J. D. Toussaint, Y. Yagi, B. E. Bouma, *et al.*, "Imaging the subcellular structure of human coronary atherosclerosis using micro-optical coherence tomography," *Nat Med*, vol. 17, pp. 1010-4, Aug 2011.
- [43] T. Attila and D. O. Faigel, "Role of endoscopic ultrasound in superficial esophageal cancer," *Dis Esophagus*, vol. 22, pp. 104-12, 2009.
- [44] A. T. Committee, V. Kaul, D. G. Adler, J. D. Conway, F. A. Farraye, S. V. Kantsevov, *et al.*, "Interventional EUS," *Gastrointest Endosc*, vol. 72, pp. 1-4, Jul 2010.
- [45] P. S. Steeg, "Tumor metastasis: mechanistic insights and clinical challenges," *Nat Med*, vol. 12, pp. 895-904, Aug 2006.
- [46] L. J. He, H. B. Shan, G. Y. Luo, Y. Li, R. Zhang, X. Y. Gao, *et al.*, "Endoscopic ultrasonography for staging of T1a and T1b esophageal squamous cell carcinoma," *World J Gastroenterol*, vol. 20, pp. 1340-7, Feb 7 2014.
- [47] L. V. Wang and J. Yao, "A practical guide to photoacoustic tomography in the life sciences," *Nat Methods*, vol. 13, pp. 627-38, Jul 28 2016.
- [48] V. Ntziachristos and D. Razansky, "Molecular imaging by means of multispectral optoacoustic tomography (MSOT)," *Chem Rev*, vol. 110, pp. 2783-94, May 12 2010.
- [49] C. Li, J. M. Yang, R. Chen, C. H. Yeh, L. Zhu, K. Maslov, *et al.*, "Urogenital photoacoustic endoscope," *Opt Lett*, vol. 39, pp. 1473-6, Mar 15 2014.
- [50] S. Sethuraman, S. R. Aglyamov, J. H. Amirian, R. W. Smalling, and S. Y. Emelianov, "Intravascular photoacoustic imaging using an IVUS imaging catheter," *Ieee Transactions on Ultrasonics Ferroelectrics and Frequency Control*, vol. 54, pp. 978-986, May 2007.
- [51] P. Beard, "Biomedical photoacoustic imaging," *Interface Focus*, vol. 1, pp. 602-31, Aug 6 2011.
- [52] J. M. Yang, C. Favazza, R. Chen, J. Yao, X. Cai, K. Maslov, *et al.*, "Simultaneous functional photoacoustic and ultrasonic endoscopy of internal organs in vivo," *Nat Med*, vol. 18, pp. 1297-1302, Aug 2012.
- [53] J. M. Yang, K. Maslov, H. C. Yang, Q. Zhou, K. K. Shung, and L. V. Wang, "Photoacoustic endoscopy," *Opt Lett*, vol. 34, pp. 1591-3, May 15 2009.
- [54] H. He, A. Buehler, and V. Ntziachristos, "Optoacoustic endoscopy with curved scanning," *Opt Lett*, vol. 40, pp. 4667-70, Oct 15 2015.
- [55] J. M. Yang, R. Chen, C. Favazza, J. Yao, C. Li, Z. Hu, *et al.*, "A 2.5-mm diameter probe for photoacoustic and ultrasonic endoscopy," *Opt Express*, vol. 20, pp. 23944-53, Oct 8 2012.
- [56] R. A. Kruger, P. Liu, Y. R. Fang, and C. R. Appledorn, "Photoacoustic ultrasound (PAUS)--reconstruction tomography," *Med Phys*, vol. 22, pp. 1605-9, Oct 1995.
- [57] M. H. Xu and L. H. V. Wang, "Photoacoustic imaging in biomedicine," *Review of Scientific Instruments*, vol. 77, p. 041101, Apr 2006.
- [58] L. W. a. H.-I. Wu, "Biomedical Optics principles and imaging," *Wiley-Interscience*, 2007.
- [59] M. H. Xu, Y. Xu, and L. H. V. Wang, "Time-domain reconstruction-algorithms and numerical simulations for thermoacoustic tomography in various geometries," *Ieee Transactions on Biomedical Engineering*, vol. 50, pp. 1086-1099, Sep 2003.
- [60] M. Xu and L. Wang, "Analytic explanation of spatial resolution related to bandwidth and detector aperture size in thermoacoustic or photoacoustic reconstruction," *Physical Review E*, vol. 67, 2003.

- [61] X. L. Dean-Ben, R. Ma, D. Razansky, and V. Ntziachristos, "Statistical approach for optoacoustic image reconstruction in the presence of strong acoustic heterogeneities," *IEEE Trans Med Imaging*, vol. 30, pp. 401-8, Feb 2011.
- [62] X. L. Dean-Ben, D. Razansky, and V. Ntziachristos, "The effects of acoustic attenuation in optoacoustic signals," *Phys Med Biol*, vol. 56, pp. 6129-48, Sep 21 2011.
- [63] B. E. Treeby, "Acoustic attenuation compensation in photoacoustic tomography using time-variant filtering," *J Biomed Opt*, vol. 18, p. 036008, Mar 2013.
- [64] A. Rosenthal, D. Razansky, and V. Ntziachristos, "Quantitative optoacoustic signal extraction using sparse signal representation," *IEEE Trans Med Imaging*, vol. 28, pp. 1997-2006, Dec 2009.
- [65] A. Buehler, A. Rosenthal, T. Jetzfellner, A. Dima, D. Razansky, and V. Ntziachristos, "Model-based optoacoustic inversions with incomplete projection data," *Medical Physics*, vol. 38, p. 1694, 2011.
- [66] C. Lutzweiler and D. Razansky, "Optoacoustic imaging and tomography: reconstruction approaches and outstanding challenges in image performance and quantification," *Sensors (Basel)*, vol. 13, pp. 7345-84, 2013.
- [67] C. Huang, K. Wang, L. Nie, L. V. Wang, and M. A. Anastasio, "Full-wave iterative image reconstruction in photoacoustic tomography with acoustically inhomogeneous media," *IEEE Trans Med Imaging*, vol. 32, pp. 1097-110, Jun 2013.
- [68] D. Calvetti, S. Morigi, L. Reichel, and F. Sgallari, "Tikhonov regularization and the L-curve for large discrete ill-posed problems," *Journal of Computational and Applied Mathematics*, vol. 123, pp. 423-446, Nov 1 2000.
- [69] C. C. P. a. M. A. Saunders, "LSQR: An algorithm for sparse linear- equations and sparse least-squares," *Journal ACM Transactions on Mathematical Software*, vol. 8, pp. 43-71, 1982.
- [70] J. Prakash and P. K. Yalavarthy, "A LSQR-type method provides a computationally efficient automated optimal choice of regularization parameter in diffuse optical tomography," *Med Phys*, vol. 40, p. 033101, Mar 2013.
- [71] X. L. Dean-Ben, V. Ntziachristos, and D. Razansky, "Acceleration of optoacoustic model-based reconstruction using angular image discretization," *IEEE Trans Med Imaging*, vol. 31, pp. 1154-62, May 2012.
- [72] K. Wang, J. Xia, C. Li, L. V. Wang, and M. A. Anastasio, "Fast spatiotemporal image reconstruction based on low-rank matrix estimation for dynamic photoacoustic computed tomography," *J Biomed Opt*, vol. 19, p. 056007, May 2014.
- [73] L. Ding, X. L. Dean-Ben, and D. Razansky, "Real-time Model-based Inversion in Cross-sectional Optoacoustic Tomography," *IEEE Trans Med Imaging*, Mar 2 2016.
- [74] X. L. Dean-Ben, A. Ozbek, and D. Razansky, "Volumetric real-time tracking of peripheral human vasculature with GPU-accelerated three-dimensional optoacoustic tomography," *IEEE Trans Med Imaging*, vol. 32, pp. 2050-5, Nov 2013.
- [75] N. Beziere and V. Ntziachristos, "Optoacoustic imaging: an emerging modality for the gastrointestinal tract," *Gastroenterology*, vol. 141, pp. 1979-85, Dec 2011.
- [76] G. P. J. A. Viator, S. L. Jacques, and S. A. Prahl,, "Design and testing of an endoscopic photoacoustic probe for determination of treatment depth after photodynamic therapy," *Proc. SPIE 4256, Biomedical Optoacoustics II*, 2001.
- [77] B. Wang and S. Emelianov, "Thermal intravascular photoacoustic imaging," *Biomed Opt Express*, vol. 2, pp. 3072-8, Nov 1 2011.
- [78] X. Li, W. Wei, Q. Zhou, K. K. Shung, and Z. Chen, "Intravascular photoacoustic imaging at 35 and 80 MHz," *J Biomed Opt*, vol. 17, p. 106005, Oct 2012.
- [79] H. He, G. Wissmeyer, S. V. Ovsepian, A. Buehler, and V. Ntziachristos, "Hybrid optical and acoustic resolution optoacoustic endoscopy," *Opt Lett*, vol. 41, pp. 2708-10, Jun 15 2016.
- [80] K. Jansen, G. van Soest, and A. F. van der Steen, "Intravascular photoacoustic imaging: a new tool for vulnerable plaque identification," *Ultrasound Med Biol*, vol. 40, pp. 1037-48, Jun 2014.

- [81] J. M. Yang, C. Li, R. Chen, Q. Zhou, K. K. Shung, and L. V. Wang, "Catheter-based photoacoustic endoscope," *J Biomed Opt*, vol. 19, p. 066001, Jun 2014.
- [82] B. Dong, S. Chen, Z. Zhang, C. Sun, and H. F. Zhang, "Photoacoustic probe using a microring resonator ultrasonic sensor for endoscopic applications," *Opt Lett*, vol. 39, pp. 4372-5, Aug 1 2014.
- [83] D. Soliman, G. J. Tservelakis, M. Omar, and V. Ntziachristos, "Combining microscopy with mesoscopy using optical and photoacoustic label-free modes," *Sci Rep*, vol. 5, p. 12902, 2015.
- [84] E. M. Strohm, M. J. Moore, and M. C. Kolios, "High resolution ultrasound and photoacoustic imaging of single cells," *Photoacoustics*, 2016.
- [85] P. Hajireza, W. Shi, and R. Zemp, "Label-free in vivo GRIN-lens optical resolution photoacoustic micro-endoscopy," *Laser Physics Letters*, vol. 10, p. 055603, 2013.
- [86] J. M. Yang, C. Li, R. Chen, B. Rao, J. Yao, C. H. Yeh, *et al.*, "Optical-resolution photoacoustic endomicroscopy in vivo," *Biomed Opt Express*, vol. 6, pp. 918-32, Mar 1 2015.
- [87] K. Jansen, A. F. van der Steen, H. M. van Beusekom, J. W. Oosterhuis, and G. van Soest, "Intravascular photoacoustic imaging of human coronary atherosclerosis," *Opt Lett*, vol. 36, pp. 597-9, Mar 1 2011.
- [88] W. Wei, X. Li, Q. Zhou, K. K. Shung, and Z. Chen, "Integrated ultrasound and photoacoustic probe for co-registered intravascular imaging," *J Biomed Opt*, vol. 16, p. 106001, Oct 2011.
- [89] Y. Yang, X. Li, T. Wang, P. D. Kumavor, A. Aguirre, K. K. Shung, *et al.*, "Integrated optical coherence tomography, ultrasound and photoacoustic imaging for ovarian tissue characterization," *Biomed Opt Express*, vol. 2, pp. 2551-61, Sep 1 2011.
- [90] Y. L. Sheu, C. Y. Chou, B. Y. Hsieh, and P. C. Li, "Image reconstruction in intravascular photoacoustic imaging," *IEEE Trans Ultrason Ferroelectr Freq Control*, vol. 58, pp. 2067-77, Oct 2011.
- [91] M. Xu and L. Wang, "Universal back-projection algorithm for photoacoustic computed tomography," *Physical Review E*, vol. 71, 2005.
- [92] T. Jetzfellner, A. Rosenthal, A. Buehler, A. Dima, K. H. Englmeier, V. Ntziachristos, *et al.*, "Optoacoustic tomography with varying illumination and non-uniform detection patterns," *J Opt Soc Am A Opt Image Sci Vis*, vol. 27, pp. 2488-95, Nov 1 2010.
- [93] A. Rosenthal, S. Kellnberger, D. Bozhko, A. Chekkoury, M. Omar, D. Razansky, *et al.*, "Sensitive interferometric detection of ultrasound for minimally invasive clinical imaging applications," *Laser & Photonics Reviews*, vol. 8, pp. 450-457, 2014.
- [94] A. Buehler, M. Kacprowicz, A. Taruttis, and V. Ntziachristos, "Real-time handheld multispectral photoacoustic imaging," *Optics Letters*, vol. 38, pp. 1404-6, 2013 May 2013.
- [95] J. M. Yang, C. Favazza, J. Yao, R. Chen, Q. Zhou, K. K. Shung, *et al.*, "Three-dimensional photoacoustic endoscopic imaging of the rabbit esophagus," *PLoS One*, vol. 10, p. e0120269, 2015.
- [96] A. L. K. a. L. L. Tres, *Histology and Cell Biology: An Introduction to Pathology*, 3 ed.: Elsevier / Mosby, 2011.
- [97] G. Sgourakis, I. Gockel, and H. Lang, "Endoscopic and surgical resection of T1a/T1b esophageal neoplasms: a systematic review," *World J Gastroenterol*, vol. 19, pp. 1424-37, Mar 7 2013.
- [98] S.-R. Puli, "Staging accuracy of esophageal cancer by endoscopic ultrasound: A meta-analysis and systematic review," *World Journal of Gastroenterology*, vol. 14, p. 1479, 2008.
- [99] M. A. A. Caballero, A. Rosenthal, A. Buehler, D. Razansky, and V. Ntziachristos, "Optoacoustic determination of spatio-temporal responses of ultrasound sensors," *IEEE Transactions on Ultrasonics, Ferroelectrics and Frequency Control*, vol. 60, pp. 1234-1244, 2013.
- [100] A. Rosenthal, V. Ntziachristos, and D. Razansky, "Optoacoustic methods for frequency calibration of ultrasonic sensors," *IEEE Trans Ultrason Ferroelectr Freq Control*, vol. 58, pp. 316-26, Feb 2011.
- [101] Y. Han, S. Tzoumas, A. Nunes, V. Ntziachristos, and A. Rosenthal, "Sparsity-based acoustic inversion in cross-sectional multiscale photoacoustic imaging," *Med Phys*, vol. 42, pp. 5444-52, Sep 2015.

- [102] J. Provost and F. Lesage, "The application of compressed sensing for photo-acoustic tomography," *IEEE Trans Med Imaging*, vol. 28, pp. 585-94, Apr 2009.
- [103] K. Lee, Y. Bresler, and M. Junge, "Subspace Methods for Joint Sparse Recovery," *IEEE Transactions on Information Theory*, vol. 58, pp. 3613-3641, 2012.
- [104] J. P. Hailong He, Andreas Buehler and Vasilis Ntziachristos, "Optoacoustic Tomography Using Accelerated Sparse Recovery and Coherence Factor Weighting," *Tomography*, vol. 2, pp. 138-145, 2016.
- [105] M. Lustig, D. Donoho, and J. M. Pauly, "Sparse MRI: The application of compressed sensing for rapid MR imaging," *Magn Reson Med*, vol. 58, pp. 1182-95, Dec 2007.
- [106] J. Prakash, C. B. Shaw, R. Manjappa, R. Kanhirodan, and P. K. Yalavarthy, "Sparse Recovery Methods Hold Promise for Diffuse Optical Tomographic Image Reconstruction," *IEEE Journal of Selected Topics in Quantum Electronics*, vol. 20, pp. 74-82, 2014.
- [107] M. V. Afonso, J. M. Bioucas-Dias, and M. A. T. Figueiredo, "Fast Image Recovery Using Variable Splitting and Constrained Optimization," *Ieee Transactions on Image Processing*, vol. 19, pp. 2345-2356, Sep 2010.
- [108] Y. H. Wang and P. C. Li, "SNR-dependent coherence-based adaptive imaging for high-frame-rate ultrasonic and photoacoustic imaging," *IEEE Trans Ultrason Ferroelectr Freq Control*, vol. 61, pp. 1419-32, Aug 2014.
- [109] P. C. Li and M. L. Li, "Adaptive imaging using the generalized coherence factor," *Ieee Transactions on Ultrasonics Ferroelectrics and Frequency Control*, vol. 50, pp. 128-141, Feb 2003.
- [110] A. Buehler, E. Herzog, D. Razansky, and V. Ntziachristos, "Video rate optoacoustic tomography of mouse kidney perfusion," *Opt Lett*, vol. 35, pp. 2475-7, Jul 15 2010.
- [111] A. Dima, N. C. Burton, and V. Ntziachristos, "Multispectral optoacoustic tomography at 64, 128, and 256 channels," *J Biomed Opt*, vol. 19, p. 36021, Mar 2014.
- [112] S. Mandal, E. Nasonova, X. L. Dean-Ben, and D. Razansky, "Optimal self-calibration of tomographic reconstruction parameters in whole-body small animal optoacoustic imaging," *Photoacoustics*, vol. 2, pp. 128-136, Sep 2014.
- [113] J. Prakash, A. S. Raju, C. B. Shaw, M. Pramanik, and P. K. Yalavarthy, "Basis pursuit deconvolution for improving model-based reconstructed images in photoacoustic tomography," *Biomed Opt Express*, vol. 5, pp. 1363-77, May 1 2014.
- [114] X. L. Dean-Ben, V. Ntziachristos, and D. Razansky, "Effects of small variations of speed of sound in optoacoustic tomographic imaging," *Med Phys*, vol. 41, p. 073301, Jul 2014.
- [115] B. E. Treeby, E. Z. Zhang, and B. T. Cox, "Photoacoustic tomography in absorbing acoustic media using time reversal," *Inverse Problems*, vol. 26, p. 115003, 2010.
- [116] X. L. Dean-Ben, R. Ma, A. Rosenthal, V. Ntziachristos, and D. Razansky, "Weighted model-based optoacoustic reconstruction in acoustic scattering media," *Phys Med Biol*, vol. 58, pp. 5555-66, Aug 21 2013.
- [117] X. L. Dean-Ben, V. Ntziachristos, and D. Razansky, "Artefact reduction in optoacoustic tomographic imaging by estimating the distribution of acoustic scatterers," *J Biomed Opt*, vol. 17, p. 110504, Nov 2012.
- [118] A. Buehler, X. L. Dean-Ben, D. Razansky, and V. Ntziachristos, "Volumetric optoacoustic imaging with multi-bandwidth deconvolution," *IEEE Trans Med Imaging*, vol. 33, pp. 814-21, Apr 2014.
- [119] K. Mitsuhashi, K. Wang, and M. A. Anastasio, "Investigation of the far-field approximation for modeling a transducer's spatial impulse response in photoacoustic computed tomography," *Photoacoustics*, vol. 2, pp. 21-32, Mar 1 2014.
- [120] M. A. O'Reilly and K. Hynynen, "A super-resolution ultrasound method for brain vascular mapping," *Med Phys*, vol. 40, p. 110701, Nov 2013.
- [121] J. A. Kennedy, O. Israel, A. Frenkel, R. Bar-Shalom, and H. Azhari, "Super-resolution in PET imaging," *IEEE Trans Med Imaging*, vol. 25, pp. 137-47, Feb 2006.

- [122] E. Van Reeth, I. W. K. Tham, C. H. Tan, and C. L. Poh, "Super-resolution in magnetic resonance imaging: A review," *Concepts in Magnetic Resonance Part A*, vol. 40A, pp. 306-325, Nov 2012.
- [123] A. Greenbaum, W. Luo, T. W. Su, Z. Gorocs, L. Xue, S. O. Isikman, *et al.*, "Imaging without lenses: achievements and remaining challenges of wide-field on-chip microscopy," *Nat Methods*, vol. 9, pp. 889-95, Sep 2012.
- [124] S. C. Park, M. K. Park, and M. G. Kang, "Super-resolution image reconstruction: A technical overview," *Ieee Signal Processing Magazine*, vol. 20, pp. 21-36, May 2003.
- [125] A. Gholipour, J. A. Estroff, and S. K. Warfield, "Robust super-resolution volume reconstruction from slice acquisitions: application to fetal brain MRI," *IEEE Trans Med Imaging*, vol. 29, pp. 1739-58, Oct 2010.
- [126] M. Fogtman, S. Seshamani, C. Kroenke, C. Xi, T. Chapman, J. Wilm, *et al.*, "A unified approach to diffusion direction sensitive slice registration and 3-D DTI reconstruction from moving fetal brain anatomy," *IEEE Trans Med Imaging*, vol. 33, pp. 272-89, Feb 2014.
- [127] R. Z. Shilling, T. Q. Robbie, T. Bailloeu, K. Mewes, R. M. Mersereau, and M. E. Brummer, "A Super-Resolution Framework for 3-D High-Resolution and High-Contrast Imaging Using 2-D Multislice MRI," *Ieee Transactions on Medical Imaging*, vol. 28, pp. 633-644, May 2009.
- [128] G. Wang, M. W. Vannier, M. W. Skinner, M. G. Cavalcanti, and G. W. Harding, "Spiral CT image deblurring for cochlear implantation," *IEEE Trans Med Imaging*, vol. 17, pp. 251-62, Apr 1998.
- [129] E. Plenge, D. H. Poot, M. Bernsen, G. Kotek, G. Houston, P. Wielopolski, *et al.*, "Super-resolution methods in MRI: can they improve the trade-off between resolution, signal-to-noise ratio, and acquisition time?," *Magn Reson Med*, vol. 68, pp. 1983-93, Dec 2012.
- [130] A. Rueda, N. Malpica, and E. Romero, "Single-image super-resolution of brain MR images using overcomplete dictionaries," *Med Image Anal*, vol. 17, pp. 113-32, Jan 2013.
- [131] H. He, S. Mandal, A. Buehler, X. Dean-Ben, D. Razansky, and V. Ntziachristos, "Improving Optoacoustic Image Quality via Geometric Pixel Super-Resolution Approach," *IEEE Trans Med Imaging*, vol. 35, pp. 812-8, Mar 2016.
- [132] S. Farsiu, M. D. Robinson, M. Elad, and P. Milanfar, "Fast and robust multiframe super resolution," *IEEE Trans Image Process*, vol. 13, pp. 1327-44, Oct 2004.
- [133] D. Robinson and P. Milanfar, "Statistical performance analysis of super-resolution," *IEEE Trans Image Process*, vol. 15, pp. 1413-28, Jun 2006.
- [134] G. E. Marai, D. H. Laidlaw, and J. J. Crisco, "Super-resolution registration using tissue-classified distance fields," *Ieee Transactions on Medical Imaging*, vol. 25, pp. 177-187, Feb 2006.
- [135] F. Zhou, W. M. Yang, and Q. M. Liao, "A Coarse-to-Fine Subpixel Registration Method to Recover Local Perspective Deformation in the Application of Image Super-Resolution," *Ieee Transactions on Image Processing*, vol. 21, pp. 53-66, Jan 2012.
- [136] H. L. He, K. He, and G. Zou, "A Lorentzian Stochastic Estimation for Video Super Resolution with Lorentzian Gradient Constraint," *Ieee Transactions on Consumer Electronics*, vol. 58, pp. 1294-1300, Nov 2012.
- [137] S. Kelly, K. M. Harris, E. Berry, J. Hutton, P. Roderick, J. Cullingworth, *et al.*, "A systematic review of the staging performance of endoscopic ultrasound in gastro-oesophageal carcinoma," *Gut*, vol. 49, pp. 534-9, Oct 2001.
- [138] M. Omar, J. Gateau, and V. Ntziachristos, "Raster-scan optoacoustic mesoscopy in the 25-125 MHz range," *Opt Lett*, vol. 38, pp. 2472-4, Jul 15 2013.
- [139] M. Omar, D. Soliman, J. Gateau, and V. Ntziachristos, "Ultrawideband reflection-mode optoacoustic mesoscopy," *Opt Lett*, vol. 39, pp. 3911-4, Jul 1 2014.
- [140] S. Yokosawa, "Identification of the layered morphology of the esophageal wall by optical coherence tomography," *World Journal of Gastroenterology*, vol. 15, p. 4402, 2009.

